Title
Visualizing dynamic states of human molecular chaperone complexes by high-resolution cryo-EM

Author
Braxton, Julian Raymond

Publication Date
2023

Visualizing dynamic states of human molecular chaperone complexes by high-resolution cryo-EM

by
Julian Raymond Braxton

DISSERTATION
Submitted in partial satisfaction of the requirements for degree of
DOCTOR OF PHILOSOPHY

in

Chemistry and Chemical Biology

in the

GRADUATE DIVISION
of the
UNIVERSITY OF CALIFORNIA, SAN FRANCISCO

Approved:

DocuSigned by:
Daniel Southworth
031AA0767EFF409...
Daniel Southworth
Chair

DocuSigned by:
Jason E. Gestwicki
Jason E. Gestwicki

DocuSigned by:
David A. Agard
David A. Agard

DocuSigned by:
Adam Frost
2BFC3B4CEA6C478...
Adam Frost

Committee Members

Acknowledgments

The process of earning a doctorate is not without its highs and lows, at least in my experience. I therefore have many people (and animals!) to thank for ensuring that I was productive, happy, and sane during these past five years, and for getting me to where I am today.

I will first thank the members of the UCSF scientific community that have shaped my experience in graduate school. I first thank my Ph.D. advisors, Daniel Southworth and Jason Gestwicki, for their unwavering support and confidence in me and my research. What started out as an unorthodox joint rotation in their labs blossomed into an exciting and interesting collaboration that exposed me to many biological systems, techniques, and, most importantly, people. I thank everyone who has cycled through their labs in my time at UCSF, but especially Hao Shao, who helped me start my first project of graduate school, Eric Tse, who taught and continues to teach me about cryo-EM, and Taylor Arhar, Kelly Monét Montgomery, Emma Carroll, Alexandrea Rizo, and Gregory Merz, who have provided much-needed advice, support, friendship, and distraction. I also thank the collaborators and friends without whom much of my work would not have been possible, including Michelle Arkin, Chad Altobelli, Elissa Fink, Kwadwo Opoku-Nsiah, Maxwell Tucker, Sarah Williams, and Aye Thwin. Finally, I would like to thank the members of my qualifying examination and dissertation committees, David Agard and Adam Frost (both), and Michelle Arkin and Danica Galonić Fujimori (qualifying), for their time, advice, and encouragement during some particularly stressful periods of graduate school.

Next, I would like to thank the teachers and mentors that helped me discover and pursue an interest in science. At the Massachusetts General Hospital and the Broad Institute, I thank Deborah Hung and Christoph Ernst for their mentorship of my undergraduate research experience. At Harvard University, I thank Martin Samuels, Dominic Mao, and Lisa Fountain for their excellent undergraduate advising and support. At the Cincinnati Country Day School, I thank my science teachers Timothy Dunn, Brock Miller, and especially Paula Butler, whose enthusiasm

and support inspired me to pursue science as a career. Finally, I thank Leah Kottyan and Charles Vorhees of the Cincinnati Children's Hospital Medical Center and Daniel Buchholz of the University of Cincinnati, who gave me my first taste of professional research by allowing me to work in their labs during summers in high school and college.

Finally, I would like to thank my friends and family, as without their support I surely would not be here today. I thank my friend and roommate Holly Vickery, and of course Ernest Demetrius Poozer Vickery III, for being a constant source of support and joy. I also thank Jill and Larry Vickery, who provided many opportunities to temporarily escape from graduate school and experience the exceptional beauty of our country. I next thank my siblings, Chandler and Blair Braxton, for providing support and strength in what we will agree was not an easy childhood. Lastly, and most importantly, I thank my mother, Patricia Braxton, who has always enabled and encouraged me to pursue my dreams and whose efforts in raising me and my siblings were nothing short of herculean.

This dissertation is dedicated to the memories of my father, Keylon Augustus Braxton, and my grandfather, Raymond David Gleason, both of whom I hope would be proud of what I have accomplished and the person I have become.

Visualizing dynamic states of human molecular chaperone complexes by high-resolution cryo-EM

Julian Raymond Braxton

Abstract

The maintenance of protein homeostasis (proteostasis) is essential in all living organisms and requires a robust network of pro-folding and pro-degradation factors. Among others, proteostasis machinery includes molecular chaperones, which promote the folding of newly-synthesized and transiently misfolded proteins, and the proteasome, which degrades misfolded or otherwise aberrant proteins. These machines frequently exhibit pronounced conformational variability and are often coupled to co-chaperones and adapter proteins, likely to accommodate the processing of diverse substrates and enable specific cellular functions. While decades of biochemistry and cell biology have established the importance of these systems, direct observation of these macromolecular complexes in functionally relevant states has only recently been enabled by seminal hardware and software advancements in high-resolution single-particle cryo-electron microscopy (cryo-EM). In addition to making routine the structure determination of almost any macromolecule of interest, this technique allows for the classification of particles based on compositional and conformational variability, and is thus uniquely suited to uncover the complicated structural dynamics characteristic of most proteostasis machinery. My doctoral work has focused on using cryo-EM to visualize challenging targets in the proteostasis network, with an emphasis on uncovering rare or dynamic states central to the understanding of these machines.

The first chapter of this dissertation reviews how the structure and function of the human AAA+ segregase p97/VCP is regulated by a large and structurally and mechanistically diverse set of adapter proteins critical for its function. Mirroring the themes of my doctoral work, we establish

that single particle cryo-EM has begun to reveal the molecular basis for many p97-adapter interactions, and suggest that this technique, coupled with advances in computational structure prediction and *in situ* structural biology, will continue to play an important role in advancing understanding of this essential and multifunctional protein complex.

The second chapter reports high-resolution cryo-EM structures of p97 in complex with UBXD1, a particularly enigmatic adapter implicated in the autophagic clearance of damaged organelles and other functions. We show that UBXD1 binding potently inhibits p97 ATPase activity and structurally remodels p97 using an extensive and unprecedented set of interactions. These interactions split the stable p97 hexamer into an open ring conformation that potentially enables unique modes of substrate processing.

The third chapter describes the reaction cycle of human mitochondrial heat shock protein 60 (mtHsp60), a conserved molecular chaperone that promotes the folding of proteins in the mitochondrial matrix. Using cryo-EM image processing techniques including symmetry expansion and focused classification, we uncover novel conformations of this dynamic machine that provide a structural rationale for the simultaneous substrate- and co-chaperone-binding activity observed in some mtHsp60 intermediates. These results likely apply to all mtHsp60 homologs.

The fourth chapter describes how the human 20S proteasome is remodeled by a sub-optimal peptide activator derived from the consensus hydrophobic, Tyr, any amino acid (HbYX) sequence. We show that this peptide binds in multiple conformations in the 20S alpha pockets, inducing a radial expansion of alpha subunit N-terminal regions that are on-pathway to complete activation. While some disordering of the 20S gate is observed, indicating partial activation, it appears that a consensus HbYX sequence is necessary to completely open the gate and allow substrates to access the interior proteolytic active sites.

Contributions

Chapter 1 is a manuscript in preparation:

Braxton, J. R. and Southworth, D. R. (2023) Regulation of p97/VCP structure and function by adapter proteins.

Chapter 2 is a manuscript in review:

Braxton, J. R., Altobelli, C. R., Tucker, M. R., Tse, E., Thwin, A. C., Arkin, M. R., and Southworth, D. R. (2023) The p97/VCP adapter UBXD1 drives AAA+ remodeling and ring opening through multi-domain tethered interactions.

Chapter 3 is a manuscript in review:

Braxton, J. R., Shao, H., Tse, E., Gestwicki, J. E., and Southworth, D. R. (2023) Asymmetric apical domain states of mitochondrial Hsp60 coordinate substrate engagement and chaperonin assembly.

Table of Contents

List of Figures

List of Tables

Chapter 1

Regulation of p97/VCP structure and function by adapter proteins

Contributing Authors:

Julian R. Braxton[1,2] and Daniel R. Southworth[2]

[1]Graduate Program in Chemistry and Chemical Biology; University of California, San Francisco; San Francisco, CA 94158, USA

[2]Department of Biochemistry and Biophysics and Institute for Neurodegenerative Diseases; University of California, San Francisco; San Francisco, CA 94158, USA

Abstract

p97/VCP is an essential eukaryotic AAA+ ATPase with diverse functions including protein homeostasis, membrane remodeling, and chromatin regulation. p97 functions in these diverse processes by extracting proteins from macromolecular assemblies by translocation through its central pore. This activity is coordinated by a set of more than 30 'adapter' proteins, which, among other functions, dictate substrate specificity and impart accessory enzymatic activity. Most adapters directly facilitate p97 substrate processing, typically through substrate recruitment or modification, pre- or post-translocation. In so doing, these adapters enable critical p97-dependent functions such as extraction of misfolded proteins from the endoplasmic reticulum or mitochondria. Adapters without substrate-binding domains are also connected to specific p97-dependent pathways, and likely serve to regulate p97 structure or control its cellular localization. Little is known about the molecular mechanisms by which most adapters regulate p97 structure and function, and it is therefore largely unclear how these interactions enable associated cellular processes. Here, we review the known functions of adapter proteins and highlight recent structural and biochemical advances that have begun to reveal the diverse molecular bases for adapter-mediated regulation of p97 function. These studies suggest that the range of mechanisms by which p97 activity is controlled is vastly underexplored, with significant advances possible for understanding p97 regulation by most known adapters.

Main Text

p97 (also called valosin-containing protein, VCP, and Cdc48 in yeast) is an abundant and essential AAA+ (ATPases associated with diverse cellular activities) translocase present in all eukaryotic organisms. Since its discovery as a hexameric ATPase in 1990 (1), p97 has been associated with a wide and ever-expanding array of cellular functions, including many in protein and organellar homeostasis, membrane remodeling, protein trafficking, and chromatin-associated processes, and has thus been dubbed a "cellular multitool" (2). p97 functions in these diverse

processes by using the energy from ATP binding and hydrolysis to extract proteins from macromolecular complexes and membranes, and is therefore considered a AAA+ ‘segregase’.

Central to p97 function are so-called ‘adapter proteins’ that directly enable segregase activity and remodel p97 for various purposes. We define adapter proteins (also called adaptors or cofactors; these names are considered interchangeable in this review) as those that enable a specific p97 function through direct interaction. Notably, while p97 can hydrolyze ATP in the absence of adapters, these proteins are required to initiate substrate processing, and are therefore essential in all known p97 functions. There are over 30 known adapter proteins; in addition to those that recruit substrate, these also include adapters that modify substrates, control p97 subcellular localization, ATPase activity, or oligomeric state. Cellular studies have long established that specific adapters or sets thereof are important in certain processes, but the molecular interactions of most with p97 are uncharacterized, and thus little is known about what role(s) p97 plays in these processes. Given the lack of structural or biochemical data on most adapters, it is thus largely unknown how these adapters alter p97 function, and for what purpose.

Dysregulation of p97 function is linked to disease, underscoring its broad importance in cellular physiology. p97 has been investigated as a cancer target, as many cancers appear to particularly depend on p97 and other proteostasis factors in a phenomenon termed ‘non-oncogene addiction’ (3, 4). To this end, many small molecule inhibitors of p97 have been developed, some of which have been evaluated in clinical trials (5, 6). Regardless of clinical utility, some of these molecules are valuable p97 chemical probes, enabling acute and specific inhibition of p97 in cells and other experimental models. Furthermore, point mutations in p97 cause neurodegenerative diseases including inclusion body myopathy associated with Paget disease of bone and frontotemporal dementia (IBMPFD, also called multisystem proteinopathy), amyotrophic lateral sclerosis, and vacuolar tauopathy (7–9). Common to these disorders is the presence of abnormal protein deposits, implicating a defect in p97-dependent protein quality

control as the cause of disease. Curiously, many disease-causing mutations appear to alter p97-adapter interactions, suggesting that perturbation of this network may contribute to disease (10–14) and underscoring the importance of adapters in p97 biology.

In this review, we discuss the knowledge gap between the known or predicted molecular architectures of adapter proteins and how they facilitate their associated p97-dependent cellular processes. We highlight recent technological advances, including high-resolution cryo-electron microscopy (cryo-EM) structure determination and accurate artificial intelligence-based structure prediction, that are enabling advances in understanding the molecular basis for adapter regulation of p97 function. These studies have revealed that a diverse ensemble of structural elements in adapters regulate p97 function, in much the same way as cochaperones of Hsp90 have been discovered to regulate its chaperone activity through a similarly large number of mechanisms. Structures of full-length adapters bound to p97 reveal that adapters frequently possess both conserved and novel p97-interaction domains which together coordinate p97 activity. We suggest that future investigations will reveal additional motifs that bind and regulate p97 in novel modes, likely with distinct effects on p97 structure and function.

p97-dependent cellular functions

p97-facilicated segregation of substrates from macromolecular structures is a component of many cellular processes (**Figure 1.1**). p97 substrates are typically, though not exclusively, targeted for translocation by the attachment of ubiquitin chains. p97 activity can be classified into two groups: facilitating proteasomal degradation of substrates, and regulating cellular processes. Regarding degradation, many proteins destined for the 26S proteasome need to be extracted from large assemblies or cellular compartments in order to gain access to proteolytic machinery; ubiquitylation targets these substrates to both p97 and the proteasome. Well-known examples of this are in endoplasmic reticulum-associated degradation (ERAD) (15, 16), where misfolded proteins need to be dislodged from the ER membrane, and in ribosome-associated quality control

(RQC) (17, 18), in which substrates need to be extracted from stalled ribosomes. p97 is therefore a central component of protein quality control and cellular stress response.

The regulatory processes facilitated by p97 substrate threading are less understood, but are nonetheless critical aspects of p97 function. For example, p97 facilitates disassembly of many multiprotein complexes from chromatin, including the replicative helicase (19, 20) and the double-strand break sensor Ku70/80 (21), enabling the completion of DNA replication and double-strand break repair, respectively. Remodeling of surface proteomes by p97 extraction also appears to be important for organellar homeostasis: p97 activity enables clearance of damaged mitochondria and lysosomes through macroautophagy (22–25), and enables endolysosomal trafficking of some proteins (12). Additionally, p97 facilitates Golgi and ER reassembly by promoting membrane fusion (26, 27), potentially through a similar regulatory mechanism. As in preparation of substrates for proteasomal degradation, substrates involved in regulatory processes are typically targeted to p97 by the presence of ubiquitin. However, this is not exclusively the case, as it has recently been demonstrated that p97 facilitates PP1 holoenzyme formation by extracting an inhibitory subunit from a precursor complex without ubiquitin conjugation (28–31). Furthermore, there are likely more ubiquitin-independent processes yet to be discovered. Finally, the adapters facilitating some p97-related processes, such as clearance of tau fibrils, are unknown (8, 32).

Mechanism of p97 substrate processing

p97 contains two AAA+ domains (D1 and D2) that bind and hydrolyze ATP (**Figure 1.2A,B**). As in all AAA+ proteins, nucleotide binding in both AAA+ domains occurs in a cleft at the interface of constituent large and small subdomains, and hydrolysis is catalyzed by trans-acting arginine fingers from an adjacent protomer (33). p97 additionally features an N-terminal domain (NTD) and a flexible C-terminal (CT) extension, which are the primary sites of adapter interaction. p97 protomers assemble to form homohexamers, which enclose a central channel. Initial structures of p97 revealed that this channel was more narrow than in other AAA+ proteins, potentially too

narrow to accommodate a protein substrate (33, 34). This led to the hypothesis that p97 does not act as a protein translocase. It was also noted that the position of the NTDs with respect to the AAA+ core was dependent on p97 nucleotide occupancy (35). Later structures clarified that the nucleotide occupancy of the D1 domain dictates NTD conformation; in this mechanism, ADP binding induces the formation of a 'down' conformation of the NTD, coplanar with the D1 ring, while ATP binding causes the NTDs to rotate above the D1 ring in a more flexible 'up' state (**Figure 1.2C**) (36). While these studies revealed p97 oligomer architecture and domain motions, they did not reveal the basis for p97 activity.

A significant advance in understanding p97 function came from experiments done by Rapoport and colleagues, using Cdc48 and other purified components of ERAD in yeast (15). This study demonstrated that luminal ERAD substrates are ubiquitylated by a membrane-bound E3 ligase, which results in the recruitment of Cdc48. Cdc48 ATPase activity dislodges substrate from the E3, allowing for proteasomal degradation. Thus, Cdc48 acts as a protein 'segregase' in ERAD and likely other pathways, though the molecular mechanism for this activity was not elucidated. An additional landmark study by the Rapoport group, also using purified components from yeast, showed that Cdc48 unfolds ubiquitylated substrates and fully translocates them through its central channel in an ATPase-dependent manner (37). This work established that p97 and its homologs indeed process substrates as do other AAA+ proteins. Structures of substrate-bound complexes then provided direct observation of Cdc48-mediated substrate processing (38, 39). These structures revealed that p97 forms right-handed spirals that enable the interaction of pore loop residues in D1 and D2 along an unfolded substrate (**Figure 1.2D**,**E**). The NTDs in these structures are in the 'up' conformation, indicating that this is the conformation active for substrate processing. Indeed, IBMPFD mutations that increase the frequency of the 'up' conformation enhance substrate processing (13). Substrate translocation appears to occur in a processive, hand-over-hand mechanism in which ATP hydrolysis and subsequent binding of ATP to the lowest

protomer causes its movement to the top of the hexamer, advancing substrate contact by ~two amino acids. This mechanism is thought to be conserved among all AAA+ translocases.

Adapters are defined by conserved p97-interacting domains

Adapters of p97 exhibit striking structural and functional diversity (**Figure 1.3** and **Table 1.1**). These proteins are typically identified by the presence of one or more domains that interact with p97. Given the conservation of many of these domains, the number of known or predicted adapters has been expanded through bioinformatic analysis of eukaryotic genomes (40, 41). Most adapters are modular assemblies of domains connected by unstructured linkers of unknown function, suggesting that conformational flexibility is an important aspect of many p97-adapter interactions. Domains mediating interaction with p97 typically bind to the NTD or CT tail, though other interaction sites exist (**Figure 1.3A**). The NTD is the primary site of adapter interaction, and binds three conserved classes of p97-interacting domains. The first of these are the ubiquitin regulatory X (UBX) and UBX-like (UBXL) domains, which are ~80 residue globular domains structurally similar to ubiquitin that bind the NTD in the cleft formed between its Nn and Nc lobes. UBX domains interact with the NTD using an arginine in the β1 strand and a tripeptide motif located in a loop (S3/S4) between β3 and β4 with consensus sequence Phe-Pro-Arg (42–45). UBXL domains bind in a similar orientation, though the residues mediating the interactions are distinct (46). The next class of NTD-interacting domains are the linear VCP-interacting (VIM) and VCP-binding (VBM) motifs, which bind by projecting charged residues into the same Nn-Nc cleft as do UBX(L) domains (40, 47, 48). Finally, the SHP box, also called binding site 1 (BS1), is a short peptide of ~8 residues that adopts a β-strand conformation with the β-sheet of the Nn lobe (49). In contrast to the large number of NTD-interacting domains, only two domains have been identified to bind the p97 CT tail, the peptide:*N*-glycanase and UBA or UBX-containing proteins (PUB) and PLAP, Ufd3p, and Lub1p (PUL) domains (50–52). Both interact with the last residues of this tail (804-Leu-Tyr-Gly-806), and thus localize adapters containing these domains to the D2

face of p97. Notably, phosphorylation of Tyr805 is a major mechanism by which PUB/PUL interactions are regulated, as this posttranslational modification abolishes interaction with the CT tail (50, 53).

In addition to highly-conserved p97-interacting domains, some adapters harbor unique p97-interacting elements that enable distinct mechanisms of modulating p97 structure and function. These include the helical lariat of ASPL, which is a four-helix insertion in its UBX domain that encircles the NTD entirely (54), and the four extensions in NPL4 that anchor this adapter directly above the p97 central channel using D1 interactions (55). Additional p97-interacting domains have yet to be structurally characterized, including the H1/H2 region of UBXD1, which interacts with the NTD-D1 interface (14, 56).

Most p97 adapters play a role in substrate processing through direct interactions with substrate proteins, and contain additional domains that enable this activity. In addition to those that simply bind substrates (as with ubiquitin-binding UBA domains found in many adapters), many of these domains modify ubiquitin chains on substrates, and include deubiquitinases (as in YOD1, Ataxin-3, and VCIP135) and ubiquitin ligases (as in HRD1, HOIP, and UBE4B). Other posttranslational modifications are enabled by deglycosylases (PNGase), kinases (DNA-PKcs), and proteases (SPRTN). However, some adapters lack these additional domains, and their role in modulating p97 activity is therefore less understood. Moreover, some adapters have multiple domains that interact with p97, though why more than one such domain is required in these adapters is not known. Indeed, at the extreme, the adapters UBXD1 and ASPL have many p97-interacting domains that account for ~50% of their sequences (**Figure 1.3B**). This implies that the function of these adapters is the controlled modulation of p97 structure, rather than simply acting as a bridge between p97 and its substrates.

Specific adapters or combinations thereof are linked to specific p97-dependent functions. For example, many p97 substrates are recognized through attachment of polyubiquitin chains,

and the ubiquitin-binding adapter UFD1/NPL4 is therefore linked to numerous p97 processes including ERAD, RQC, chromatin-associated degradation, and others (15, 17, 57, 58). In contrast, some adapters appear to facilitate more specialized processes. For example, the SPRTN metalloprotease mediates recruitment of p97 to sites of DNA damage, which facilitates the extraction of specific DNA damage response proteins and may limit the number of mutations introduced (59–61). Of note, combinations of substrate-binding and non-substrate-binding adapters appear to cooperate in certain p97 processes, including YOD1 and PLAA (binding) and UBXD1 (non-binding) in lysophagy (22), suggesting the functions of the two classes are not mutually exclusive.

The complexity of the p97 adapter network, already significant in lower eukaryotes, is even more apparent in humans. For example, SEP (Shp1, eyes closed, and p47)-domain proteins are among the most studied p97 adapters due to their abundance and affinity for p97 (27). Only one SEP-domain protein exists in yeast, Shp1, whereas humans have four, all of which appear to have distinct functions. Moreover, some adapters such as UBXD1 are only present in higher eukaryotes, implying a more sophisticated range of p97 regulation and function. Of note, it is possible that there are p97 adapters yet to be discovered due to the lack of known p97-interacting domains. Finally, the logic of adapter interactions in certain p97 processes is intriguing. For example, many effectors of ERAD directly interact with p97, including channel-forming Derlins (62), the ER membrane-resident E3 ubiquitin ligase gp78 (63), and the ER membrane-resident adapter VIMP (64, 65). Clearly, localization of p97 to the ER membrane is a critical function, but why all of these adapters need p97-interacting domains is unclear.

Technological advances enabling structural studies of adapters

Structural interrogation of adapter proteins has until recently been limited to structures of isolated p97-interacting domains (with or without p97 or truncations thereof) and low-resolution cryo-EM reconstructions. These studies have provided foundational insight into p97-adapter interactions,

revealing diverse interaction modes of p97-interacting domains with the NTD and C-terminus, and identifying the NTD-D1 face of the p97 hexamer as a major site of adapter interaction. However, while these results have generated preliminary models of adapter-mediated regulation of p97, a major limitation has been the lack of full-length p97-adapter structures. These structures are desired for several reasons: they would enable the identification of unknown p97-interaction domains, reveal unique arrangements of adapters not predicted by sequence alone, and identify adapter-mediated structural rearrangements of p97 critical to its function. Such structures therefore have the potential to bridge the gap between annotated cellular functions of p97 and the underlying molecular interactions that facilitate them.

Analysis of full-length p97-adapter complexes has been facilitated by two major and ongoing developments: advances in cryo-EM hardware and software, and artificial intelligence (AI)-enabled structure prediction. Regarding cryo-EM, it is widely appreciated that improved microscope design, direct electron detectors, and maximum-likelihood-based classification algorithms have enabled the so-called ‘resolution revolution’ in single-particle cryo-EM, making it the current method of choice for structural biology (66). These advances have facilitated the determination of structures recalcitrant to crystallization, whether due to conformational or compositional sample heterogeneity, enabling high-resolution characterization of many large, dynamic multiprotein complexes. This is well-illustrated by the processing workflow employed in a recent study of p47-mediated substrate processing, in which the authors were able to separate particles without substrate from those with it (**Figure 1.4A**); the coexistence of these two populations would likely preclude crystallization (67). Beyond these generally applicable developments, there are challenges specific to p97-adapter structure determination that make advances in cryo-EM software particularly enabling. First, p97 complexes are often characterized by a relatively rigid core composed of the AAA+ domains, while the smaller peripheral regions, namely NTDs and adapter proteins, exhibit pronounced flexibility with respect to this core. In

consensus reconstructions, these peripheral regions, often those of particular interest, are averaged out at the expense of the stronger AAA+ density. Thus, the mechanisms of adapter interaction are frequently obscured. To overcome these challenges, many algorithms have been developed to improve visualization of peripheral or flexible regions (68). Most prominent among these are focused classification and refinement, which allow the user to focus on a region of interest using a mask around the desired density (68). These strategies have been employed successfully in several studies of p97 homologs (38, 39).

Accurate, high-throughput protein structure prediction is also beginning to transform the study of adapters. In particular, with the development of AlphaFold2, RoseTTAFold, and other algorithms, it is now possible to predict the structure of nearly any protein in the human proteome, with many being precomputed and publicly available (69–72). These predictions have revealed a striking structural diversity of adapters, raising many questions about their interactions with p97. Indeed, the (predicted) structures of many adapters suggest novel functions. For example, the predicted structure of FAF2 features substrate-binding UBA and membrane-anchoring domains clustered on one end of the protein, and a p97-binding UBX domain at the other (**Figure 1.4B**). These sides appear connected by an extremely long alpha helix, and perhaps imply that precise spatial positioning of UBA and UBX domains is important for FAF2-enabled functions; however, this has yet to be tested experimentally. These predictions can also facilitate the identification of unknown density in experimental structures, an especially important application given the large unannotated regions present in many adapters. Further advances in the accurate prediction of multimeric complexes will likely continue to facilitate prediction-guided hypotheses about p97-adapter interactions.

High-resolution structures of intact p97-adapter complexes reveal novel regulatory mechanisms and interaction modes

In the past few years, much progress has been made in identifying the mechanisms by which adapter proteins bind to and regulate p97. Many of these discoveries have relied on cryo-EM image processing algorithms, and it is likely that this approach, coupled with machine learning-generated models, will continue to enable similar breakthroughs. Notable developments are discussed below.

Substrate processing by UFD1/NPL4 and SEP-domain adapters

How adapters enable processing of p97 substrates has been an area of active study. Direct observation of this activity has only recently been achieved using single-particle cryo-EM. This is due to the significant conformational heterogeneity of substrate-bound structures, which, in a manner similar to that of all other substrate-bound AAA+ complexes, precludes formation of an ordered lattice needed for structure determination by X-ray crystallography. Seminal cryo-EM studies of substrate translocation enabled by UFD1/NPL4 and Shp1 in yeast Cdc48 were published in 2019 (38, 39), and reveal many insights into how adapters enable this activity (**Figure 1.5A,B**).

While the mechanism of substrate translocation appears conserved among all AAA+ proteins, the roles of adapter proteins in enabling this activity are distinct. The heterodimeric UFD1/NPL4 adapter is among the best structurally characterized due to its stable tower-like structure on the D1 face of p97. NPL4 binds K48-linked ubiquitin molecules in folded and unfolded states using its MPN and CTD domains; unfolded ubiquitin is bound in a conserved groove positioned directly above the entrance to the p97 central channel. Interactions by the UT3 domain of UFD1 also contribute to ubiquitin binding. In agreement with a previous substrate-free Cdc48/UFD1/NPL4 structure (55), interactions with the p97 hexamer are extensive, and involve conserved and unique interactions that could not be completely anticipated based on homology

to other proteins or domains thereof. NPL4 uses two zinc fingers and an N-terminal bundle to anchor onto the D1 ring, as well as a UBXL domain that binds the p97 NTD. The UT6 domain of UFD1 harbors two SHP boxes that also bind NTDs, though they, and the UBXL, are not well resolved due to the flexibility of the NTDs in the up state. Together these structures reveal an intimate and highly coordinated arrangement of p97- and substrate-interacting domains that enable unfolding of ubiquitylated substrates. Critically, these observations were enabled by resolution improvements facilitated by modern image processing practices, including for example subtraction of D2 signal to better classify D1/NPL4, and local refinement of the D1/NPL4 and D2 regions separately.

In contrast to the multifaceted interactions of UFD1/NPL4 with p97 and substrate, SEP-domain adapters (including yeast Shp1 and human homologs p37 and p47) are considerably simplified. Shp1 has a UBA domain that interacts with ubiquitin, as well as a UBX and SHP box that bind p97 NTDs. Immunoprecipitation and cryo-EM imaging of Shp1 from yeast in the presence of ADP-BeFx yielded substrate-bound p97 complexes, in which the only non-p97 density was the unfolded substrate in the central channel and the UBX of Shp1 (**Figure 1.5C**) (39). This suggests that Shp1 flexibly associates with p97 and substrate, rather than adopting a stable structure as with UFD1/NPL4. Indeed, substrate-bound (29, 67) and -unbound (73) structures of p97 complexes with human Shp1 homologs further confirm the flexible association of these adapters with p97. Further advances in image processing may enable visualization of poorly-resolved regions of these adapters.

Hexamer dissociation by ASPL

The importance of studying regions of adapter proteins outside highly conserved domains is exemplified by the characterization of the non-canonical adapter ASPL (**Figure 1.5D**). ASPL has a UBX, UBXL, and SHP box, and was identified to dissociate p97 hexamers into smaller oligomers and monomers (54). Truncation analysis revealed that the region responsible for this activity was

the UBX domain and an uncharacterized region inserted therein termed the helical lariat. X-ray crystallography of p97 and an ASPL construct containing these elements revealed that the UBX domain interacts with the p97 NTD in a manner conserved among all known UBX proteins, but the helical lariat structure completely encircles this NTD and contacts the associated D1 through unprecedented interactions, displacing a neighboring p97 protomer (54). Though a definitive cellular role of ASPL-mediated p97 disassembly is lacking, a recent study reported that this disassembly enables methylation of an otherwise inaccessible lysine residue by METTL21D (also known as VCPKMT), which could potentially alter p97 activity (74). This work reveals that p97 adapters can have functions unrelated to directly enabling substrate processing, and that p97 structure is regulated through diverse mechanisms.

Conclusions and perspectives

Though much progress has been made in understanding the mechanisms by which p97 is regulated by adapter proteins, there remains much to be discovered. It is increasingly apparent that adapter studies *in vitro* are most informative when performed with full-length proteins, given the likelihood of unannotated elements being important for their activity. This is well-illustrated by studies of UFD1/NPL4 and ASPL, both of which feature unanticipated elements that contribute to p97 binding. However, nearly all other adapters have not been structurally or functionally characterized using full-length protein, leaving much unknown. A related issue is the disconnect between the molecular basis of adapter interactions with p97 and their associated cellular functions; this is especially true for non-substrate-binding adapters. Given the complexities of p97-adapter interactions in cells, we anticipate that technologies that bridge the gap between biochemistry and cell biology will enable significant advances in our understanding of these processes. Indeed, purification and analysis of native complexes has already proven to be successful in the study of SEP-domain adapters (39, 67), and this approach can likely be applied to others. High-resolution cellular cryo-electron tomography might also facilitate these efforts,

enabling direct observation of p97 complexes in their native environment. This might reveal unknown interacting partners, as well as provide spatial context that appears relevant in many p97-dependent processes.

Figures

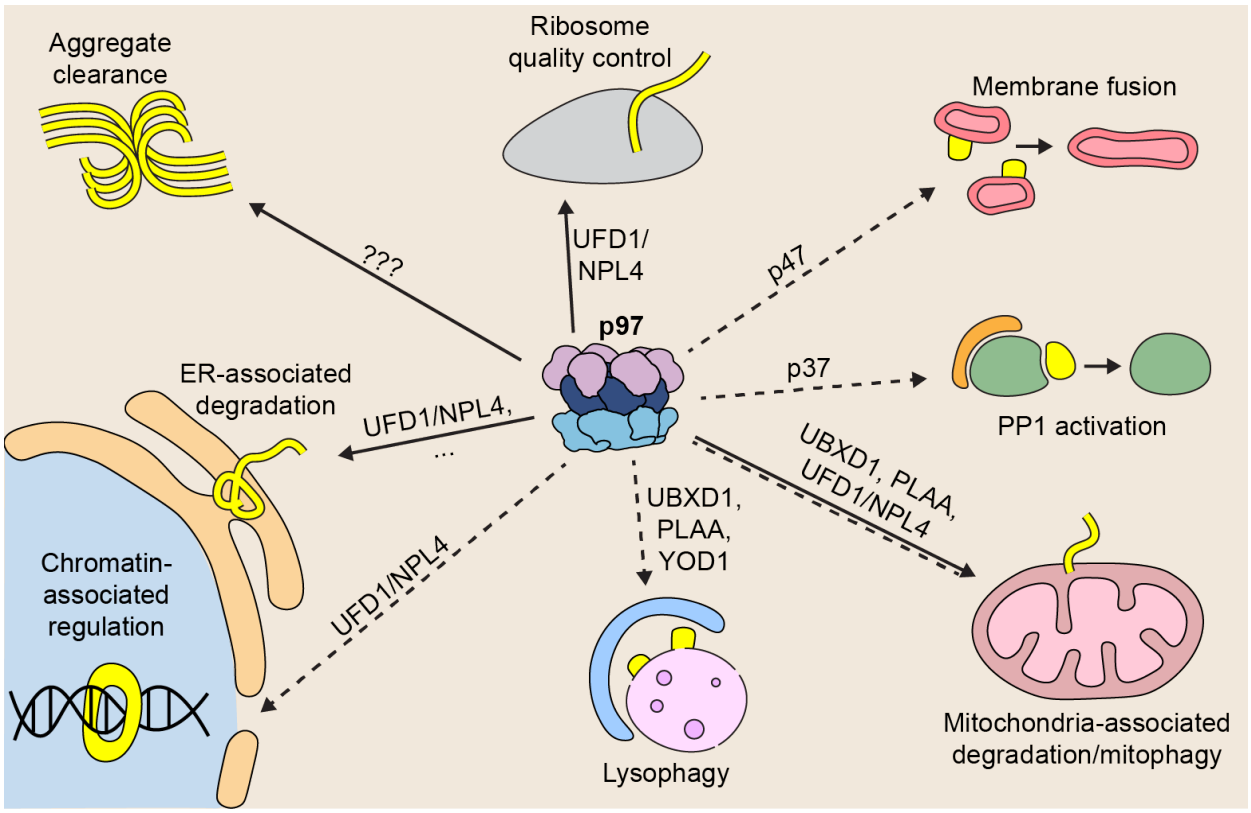

Figure 1.1 Cellular functions of p97
Representative p97-dependent functions, with associated adapters listed. Functions that result in clearance of misfolded/aggregated proteins by proteasomal degradation are indicated by solid lines; those that enable regulatory segregation are indicated by dashed lines.

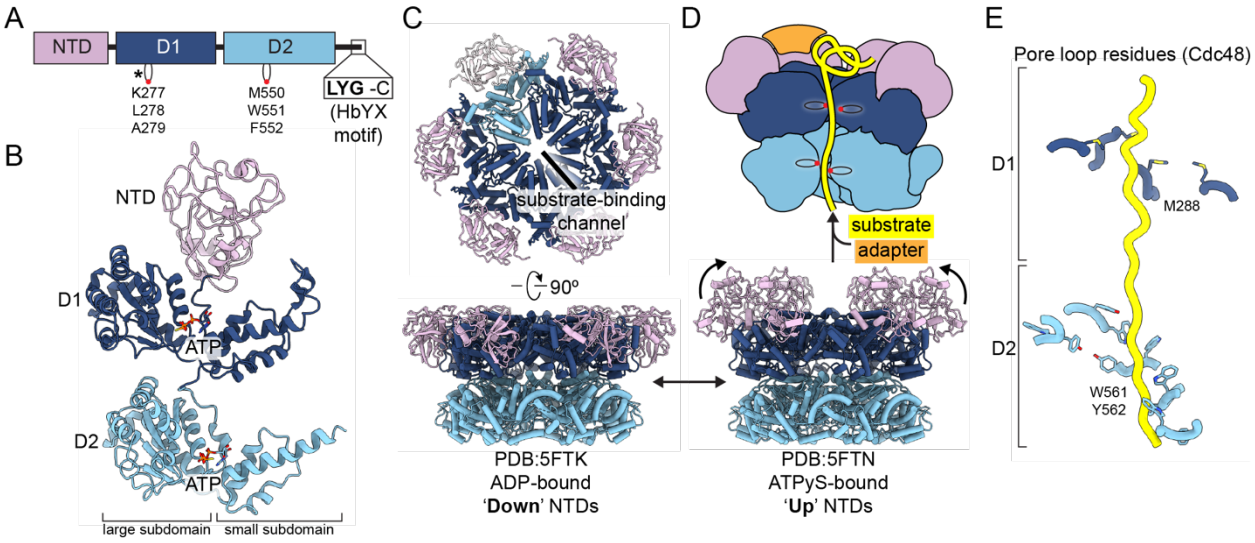

Figure 1.2 Domain structure and hexamer architecture of human p97
(**A**) Domain schematic of human p97. Pore loop residues identified to contact substrate are shown. Degenerate residues in D1 are indicated (*), as well as the HbYX motif at the C-terminus. (**B**) View of ATPyS-bound p97 protomer (PDB 5FTN), colored as in (A). (**C**) Views of ADP-bound (left, PDB 5FTK) and ATPyS-bound (right, PDB 5FTN) p97 hexamers. One protomer in the top view of 5FTK is colored in lighter shades to delineate protomer boundaries. (**D**) Illustration of substrate threading through the p97 central pore. (**E**) View of substrate in the Cdc48 channel (PDB 6OA9), showing spiral arrangement of pore loops in D1 and D2.

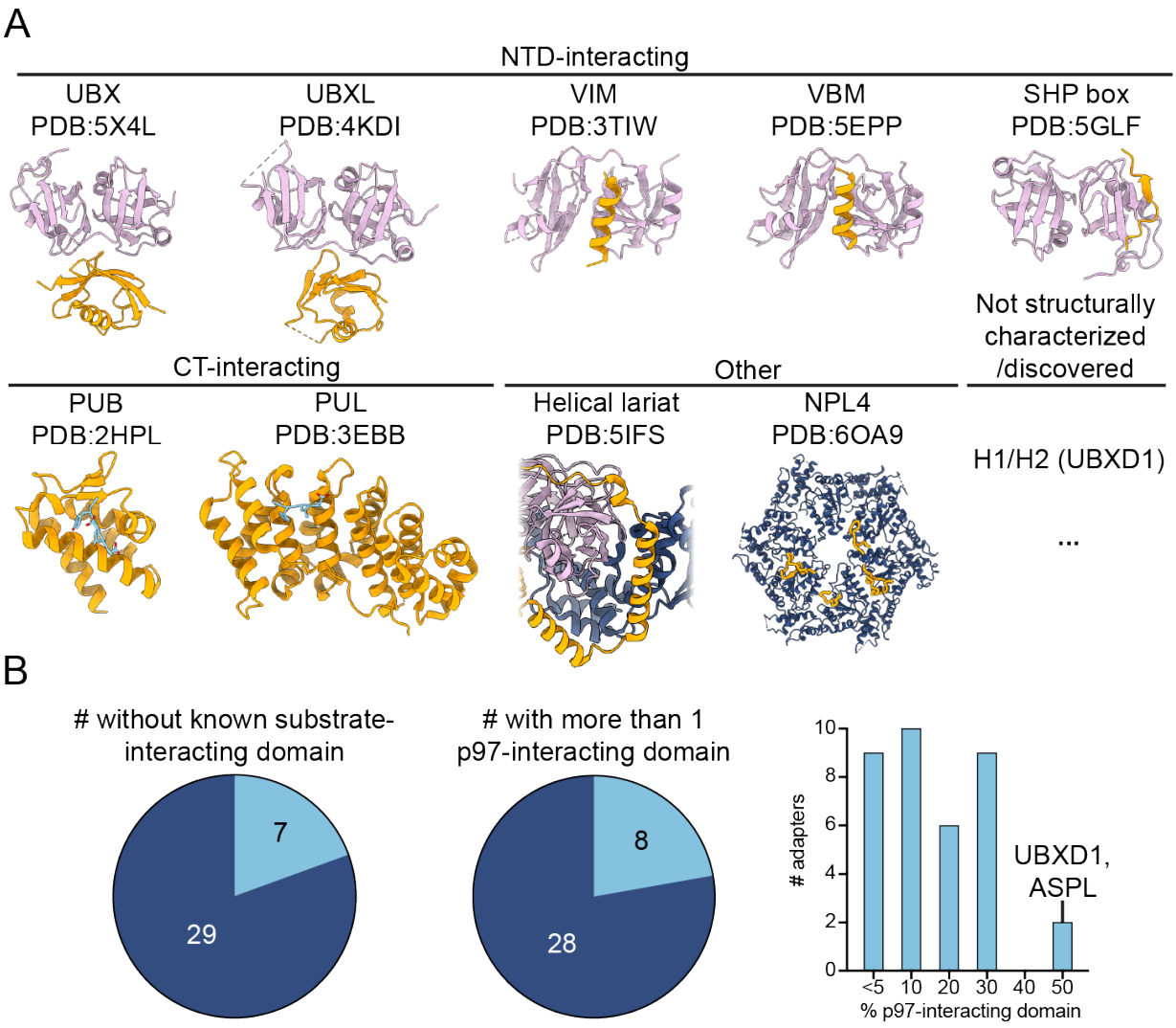

Figure 1.3 Architecture of p97 adapters
(**A**) Structures of p97-interacting domains of adapters bound to p97 or truncations thereof. (**B**) Summary statistics of known adapter proteins.

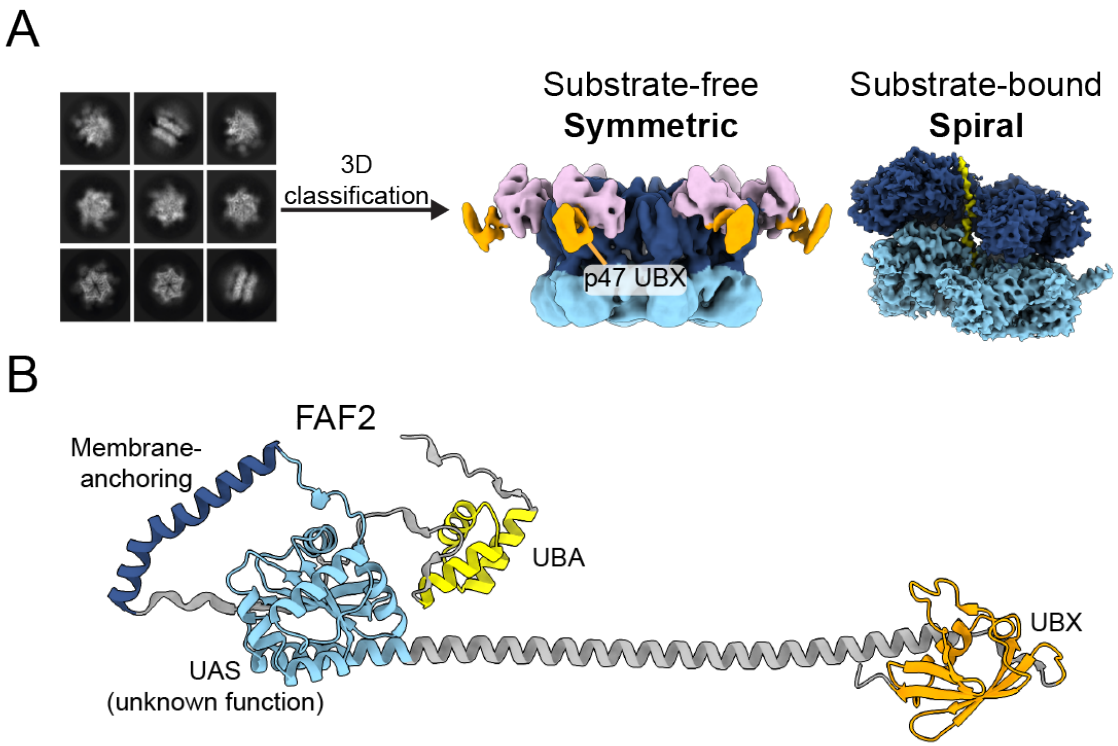

Figure 1.4 Technological advances enabling study of p97-adapter interactions
(**A**) Schematic of cryo-EM processing workflow for p97-p47 complexes from (67). 3D classification enabled the separation of planar, C6-symmetric substrate-free complexes from spiral, substrate-bound complexes. (**B**) AlphaFold2 model of FAF2, showing an unanticipated arrangement of domains, in which the UBX domain (orange) is connected by a long alpha helix to other components. The substrate-interacting domain is shown in yellow, and other annotated domains in blues.

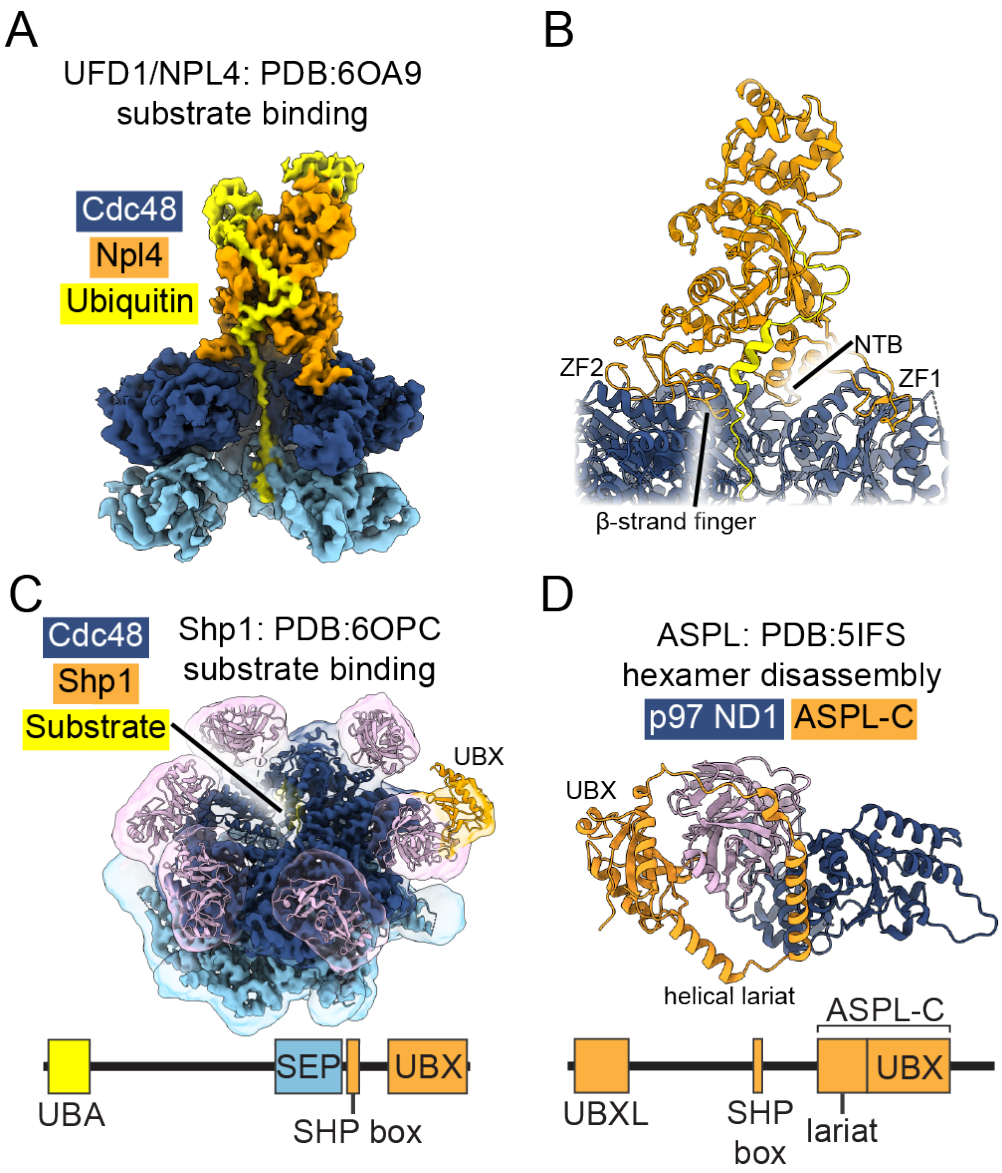

Figure 1.5 Structures of intact p97-adapter complexes
(**A**) Structure of yeast Cdc48 bound to the UFD1/NPL4 adapter, unfolding a ubiquitylated substrate and threading it through the Cdc48 central channel. (**B**) Enlarged view of contacts made between NPL4 and Cdc48. ZF = zinc finger, NTB = N-terminal bundle. (**C**) Structure of substrate-bound Cdc48 bound to the Shp1 adapter. A filtered transparent map is shown over the sharpened map and model, showing density for the NTDs and UBX domain. The domain schematic of Shp1 is shown below. (**D**) Structure of an ASPL truncation construct containing the UBX and helical lariat domains (ASPL-C) bound to a human p97 construct (N and D1 domains only). The domain schematic of ASPL is shown below.

Tables

(next page)

Table 1.1 List of human p97 adapters

Common name	Protein	Gene	UniProt ID	UBX	UBXL	VIM	VBM	SHP	PUB	PUL	H1/H2	Lariat	NPL4	Enzymatic activity	Substrate binding?	% p97 interacting
AIRAPL	AN1-type zinc finger protein 2B	ZFAND2B	Q8WV99			•								N/A	Yes	5
ANKZF1	Ankyrin repeat and zinc finger domain-containing protein 1	ANKZF1	Q9H8Y5			•								Peptidyl-tRNA hydrolase	Yes	2
ASPL (UBXD9)	Tether containing UBX domain for GLUT4	ASPSCR1 (UBXN9)	Q9BZE9	•	•			•				•		N/A	No	47
Ataxin-3	Ataxin-3	ATXN3	P54252				•							Deubiquitinase	Yes	7
CHIP	E3 ubiquitin-protein ligase CHIP	STUB1	Q9UNE7				•							E3 ubiquitin ligase	Yes	2
Derlin-1	Derlin-1	DERL1 (DER1)	Q9BUN8					•						N/A	Yes	5
Derlin-2	Derlin-2	DERL2 (DER2)	Q9GZP9					•						N/A	Yes	5
DNA-PKcs	DNA-dependent protein kinase catalytic subunit	PRKDC	P78527			•								Kinase	Yes	<1
FAF1 (UBXD12)	FAS-associated factor 1	FAF1 (UBXN3A)	Q9UNN5	•										N/A	Yes	12
FAF2 (UBXD8)	FAS-associated factor 2	FAF2 (UBXN3B)	Q96CS3	•										N/A	Yes	18
gp78	E3 ubiquitin-protein ligase AMFR	AMFR	Q9UKV5			•								E3 ubiquitin ligase	Yes	3
HOIP	E3 ubiquitin-protein ligase RNF31	RNF31	Q96EP0						•					E3 ubiquitin ligase	Yes	7
HRD1	E3 ubiquitin-protein ligase synoviolin	SYVN1	Q86TM6				•							E3 ubiquitin ligase	Yes	2
NPL4	Nuclear protein localization protein 4 homolog	NPLOC4	Q8TAT6		•								•	N/A	Yes	27
NUB1	NEDD8 ultimate buster 1	NUB1	Q9Y5A7				•							N/A	Yes	6
OTU1	Ubiquitin thioesterase OTU1	YOD1	Q5VVQ6		•									Deubiquitinase	Yes	22

(continued)

Common name	Protein	Gene	UniProt ID	UBX	UBXL	VIM	VBM	SHP	PUB	PUL	H1/H2	Lariat	NPL4	Enzymatic activity	Substrate binding?	% p97 interacting
p37	UBX domain-containing protein 2B	UBXN2B	Q14CS0	•				•						N/A	Yes	27
p47	NSFL1 cofactor p47	NSFL1C (UBXN2C)	Q9UNZ2	•				•						N/A	Yes	24
PLAA (PLA2P, PLAP, UFD3)	Phospholipase A-2-activating protein	PLAA	Q9Y263							•				N/A	Yes	31
PNGase	Peptide-N(4)-(N-acetyl-beta-glucosaminyl)asparagine amidase	NGLY1	Q96IV0						•					Deglycosylase	Yes	10
RHBDL4	Rhomboid-related protein 4	RHBDD1	Q8TEB9				•							Protease	Yes	5
SAKS1	UBX domain-containing protein 1	UBXN1 (SAKS1)	Q04323	•										N/A	Yes	29
SPRTN (DVC1)	DNA-dependent metalloprotease SPRTN	SPRTN	Q9H040					•						Protease	Yes	2
SVIP	Small VCP/p97-interacting protein	SVIP	Q8NHG7			•								N/A	No	27
TEX264	Testis-expressed protein 264	TEX264	Q9Y6I9					•						N/A	Yes	4
UBE4B (UFD2)	Ubiquitin conjugation factor E4 B	UBE4B	O95155				•							E3 ubiquitin ligase	Yes	1
UBXD1	UBX domain-containing protein 6	UBXN6	Q9BZV1	•		•			•		•			N/A	No	51
UBXD2 (Erasin)	UBX domain-containing protein 4	UBXN4	Q92575	•										N/A	No	15
UBXD3	UBX domain-containing protein 10	UBXN10	Q96LJ8	•										N/A	No	27
UBXD4	UBX domain-containing protein 2A	UBXN2A	P68543	•				•						N/A	Yes	33
UBXD5 (Socius)	UBX domain-containing protein 11	UBXN11 (SOC)	Q5T124	•				•						N/A	Yes	17

(continued)

Common name	Protein	Gene	UniProt ID	UBX	UBXL	VIM	VBM	SHP	PUB	PUL	H1/H2	Lariat	NPL4	Enzymatic activity	Substrate binding?	% p97 interacting
UBXD6	UBX domain-containing protein 8	UBXN8	O00124	•										N/A	No	28
UBXD7	UBX domain-containing protein 7	UBXN7	O94888	•										N/A	Yes	16
UFD1	Ubiquitin recognition factor in ER-associated degradation protein 1	UFD1 (UFD1L)	Q92890					••						N/A	Yes	8
VCIP135	Deubiquitinating protein VCPIP1	VCPIP1	Q96JH7		•									Deubiquitinase	Yes	6
VIMP	Selenoprotein S	SELENOS	Q9BQE4			•								N/A	No	27

Acknowledgments

This work was supported by National Institutes of Health grants F31GM142279 (to J.R.B.) and R01GM138690 (to D.R.S.).

Author Contributions

J.R.B., D.R.S. conceptualization; J.R.B. writing–original draft; J.R.B., D.R.S. writing–review & editing.

References

1. Peters, J. M., Walsh, M. J., and Franke, W. W. (1990) An abundant and ubiquitous homo-oligomeric ring-shaped ATPase particle related to the putative vesicle fusion proteins Sec18p and NSF. *Embo J*. 9, 1757–1767
2. Stach, L., and Freemont, P. S. (2017) The AAA+ ATPase p97, a cellular multitool. *Biochem J*. 474, 2953–2976
3. Fessart, D., Marza, E., Taouji, S., Delom, F., and Chevet, E. (2013) P97/CDC-48: Proteostasis control in tumor cell biology. *Cancer Lett*. 337, 26–34
4. Vekaria, P. H., Home, T., Weir, S., Schoenen, F. J., and Rao, R. (2016) Targeting p97 to Disrupt Protein Homeostasis in Cancer. *Frontiers Oncol*. 6, 181
5. Benajiba, L., Carraway, H. E., Hamad, N., Stein, E. M., Yannakou, C. K., Burroughs, A., Harris, S., Lane, H., Nguyen, D. D., Stuart, M., Vargas, J., Puissant, A., Stegmaier, K., and DiNardo, C. D. (2020) Trials in Progress: A Phase I Study to Evaluate the Safety and Pharmacokinetic Profiles of CB-5339 in Participants with Relapsed/Refractory Acute Myeloid Leukemia or Relapsed/Refractory Intermediate or High-Risk Myelodysplastic Syndrome. *Blood*. 136, 21–21
6. Kilgas, S., and Ramadan, K. (2023) Inhibitors of the ATPase p97/VCP: From basic research to clinical applications. *Cell Chem Biol*. 10.1016/j.chembiol.2022.12.007
7. Watts, G. D. J., Wymer, J., Kovach, M. J., Mehta, S. G., Mumm, S., Darvish, D., Pestronk, A., Whyte, M. P., and Kimonis, V. E. (2004) Inclusion body myopathy associated with Paget disease of bone and frontotemporal dementia is caused by mutant valosin-containing protein. *Nat Genet*. 36, 377–381
8. Darwich, N. F., Phan, J. M., Kim, B., Suh, E., Papatriantafyllou, J. D., Changolkar, L., Nguyen, A. T., O'Rourke, C. M., He, Z., Porta, S., Gibbons, G. S., Luk, K. C., Papageorgiou, S. G., Grossman, M., Massimo, L., Irwin, D. J., McMillan, C. T., Nasrallah, I. M., Toro, C., Aguirre,

G. K., Deerlin, V. M. V., and Lee, E. B. (2020) Autosomal dominant VCP hypomorph mutation impairs disaggregation of PHF-tau. *Science*. 10.1126/science.aay8826

9. Johnson, J. O., Mandrioli, J., Benatar, M., Abramzon, Y., Deerlin, V. M. V., Trojanowski, J. Q., Gibbs, J. R., Brunetti, M., Gronka, S., Wuu, J., Ding, J., McCluskey, L., Martinez-Lage, M., Falcone, D., Hernandez, D. G., Arepalli, S., Chong, S., Schymick, J. C., Rothstein, J., Landi, F., Wang, Y.-D., Calvo, A., Mora, G., Sabatelli, M., Monsurrò, M. R., Battistini, S., Salvi, F., Spataro, R., Sola, P., Borghero, G., Consortium, T. I., Galassi, G., Scholz, S. W., Taylor, J. P., Restagno, G., Chiò, A., and Traynor, B. J. (2010) Exome Sequencing Reveals VCP Mutations as a Cause of Familial ALS. *Neuron*. 68, 857–864
10. Bulfer, S. L., Chou, T.-F., and Arkin, M. R. (2016) p97 Disease Mutations Modulate Nucleotide-Induced Conformation to Alter Protein–Protein Interactions. *Acs Chem Biol*. 11, 2112–2116
11. Zhang, X., Gui, L., Zhang, X., Bulfer, S. L., Sanghez, V., Wong, D. E., Lee, Y., Lehmann, L., Lee, J. S., Shih, P.-Y., Lin, H. J., Iacovino, M., Weihl, C. C., Arkin, M. R., Wang, Y., and Chou, T.-F. (2015) Altered cofactor regulation with disease-associated p97/VCP mutations. *Proc National Acad Sci*. 112, E1705–E1714
12. Ritz, D., Vuk, M., Kirchner, P., Bug, M., Schütz, S., Hayer, A., Bremer, S., Lusk, C., Baloh, R. H., Lee, H., Glatter, T., Gstaiger, M., Aebersold, R., Weihl, C. C., and Meyer, H. (2011) Endolysosomal sorting of ubiquitylated caveolin-1 is regulated by VCP and UBXD1 and impaired by VCP disease mutations. *Nat Cell Biol*. 13, 1116–1123
13. Blythe, E. E., Gates, S. N., Deshaies, R. J., and Martin, A. (2019) Multisystem Proteinopathy Mutations in VCP/p97 Increase NPLOC4·UFD1L Binding and Substrate Processing. *Structure*. 27, 1820-1829.e4
14. Schuetz, A. K., and Kay, L. E. (2016) A Dynamic molecular basis for malfunction in disease mutants of p97/VCP. *Elife*. 5, e20143

15. Stein, A., Ruggiano, A., Carvalho, P., and Rapoport, T. A. (2014) Key Steps in ERAD of Luminal ER Proteins Reconstituted with Purified Components. *Cell*. 158, 1375–1388
16. Brodsky, J. L. (2012) Cleaning Up: ER-Associated Degradation to the Rescue. *Cell*. 151, 1163–1167
17. Brandman, O., Stewart-Ornstein, J., Wong, D., Larson, A., Williams, C. C., Li, G.-W., Zhou, S., King, D., Shen, P. S., Weibezahn, J., Dunn, J. G., Rouskin, S., Inada, T., Frost, A., and Weissman, J. S. (2012) A Ribosome-Bound Quality Control Complex Triggers Degradation of Nascent Peptides and Signals Translation Stress. *Cell*. 151, 1042–1054
18. Brandman, O., and Hegde, R. S. (2016) Ribosome-associated protein quality control. *Nat Struct Mol Biol*. 23, 7–15
19. Moreno, S. P., Bailey, R., Campion, N., Herron, S., and Gambus, A. (2014) Polyubiquitylation drives replisome disassembly at the termination of DNA replication. *Science*. 346, 477–481
20. Maric, M., Maculins, T., Piccoli, G. D., and Labib, K. (2014) Cdc48 and a ubiquitin ligase drive disassembly of the CMG helicase at the end of DNA replication. *Science*. 346, 1253596
21. van den Boom, J., Wolf, M., Weimann, L., Schulze, N., Li, F., Kaschani, F., Riemer, A., Zierhut, C., Kaiser, M., Iliakis, G., Funabiki, H., and Meyer, H. (2016) VCP/p97 Extracts Sterically Trapped Ku70/80 Rings from DNA in Double-Strand Break Repair. *Mol Cell*. 64, 189–198
22. Papadopoulos, C., Kirchner, P., Bug, M., Grum, D., Koerver, L., Schulze, N., Poehler, R., Dressler, A., Fengler, S., Arhzaouy, K., Lux, V., Ehrmann, M., Weihl, C. C., and Meyer, H. (2016) VCP/p97 cooperates with YOD1, UBXD1 and PLAA to drive clearance of ruptured lysosomes by autophagy. *Embo J*. 36, 135–150
23. Bento, A. C., Bippes, C. C., Kohler, C., Hemion, C., Frank, S., and Neutzner, A. (2018) UBXD1 is a mitochondrial recruitment factor for p97/VCP and promotes mitophagy. *Sci Rep-uk*. 8, 12415

24. Tanaka, A., Cleland, M. M., Xu, S., Narendra, D. P., Suen, D.-F., Karbowski, M., and Youle, R. J. (2010) Proteasome and p97 mediate mitophagy and degradation of mitofusins induced by Parkin. *J Cell Biology*. 191, 1367–1380

25. McLelland, G.-L., Goiran, T., Yi, W., Dorval, G., Chen, C. X., Lauinger, N. D., Krahn, A. I., Valimehr, S., Rakovic, A., Rouiller, I., Durcan, T. M., Trempe, J.-F., and Fon, E. A. (2018) Mfn2 ubiquitination by PINK1/parkin gates the p97-dependent release of ER from mitochondria to drive mitophagy. *Elife*. 7, e32866

26. Uchiyama, K., and Kondo, H. (2005) p97/p47-Mediated Biogenesis of Golgi and ER. *J Biochem*. 137, 115–119

27. Kondo, H., Rabouille, C., Newman, R., Levine, T. P., Pappin, D., Freemont, P., and Warren, G. (1997) p47 is a cofactor for p97-mediated membrane fusion. *Nature*. 388, 75–78

28. Kracht, M., Boom, J. van den, Seiler, J., Kröning, A., Kaschani, F., Kaiser, M., and Meyer, H. (2020) Protein Phosphatase-1 Complex Disassembly by p97 is Initiated through Multivalent Recognition of Catalytic and Regulatory Subunits by the p97 SEP-domain Adapters. *J Mol Biol*. 432, 6061–6074

29. Boom, J. van den, Meyer, H., and Saibil, H. (2022) Structural basis of ubiquitin-independent PP1 complex disassembly by p97. *Biorxiv*. 10.1101/2022.06.24.497491

30. Weith, M., Seiler, J., Boom, J. van den, Kracht, M., Hülsmann, J., Primorac, I., Garcia, J. del P., Kaschani, F., Kaiser, M., Musacchio, A., Bollen, M., and Meyer, H. (2018) Ubiquitin-Independent Disassembly by a p97 AAA-ATPase Complex Drives PP1 Holoenzyme Formation. *Mol Cell*. 72, 766-777.e6

31. Boom, J. van den, Kueck, A. F., Kravic, B., Müschenborn, H., Giesing, M., Pan, D., Kaschani, F., Kaiser, M., Musacchio, A., and Meyer, H. (2021) Targeted substrate loop insertion by VCP/p97 during PP1 complex disassembly. *Nat Struct Mol Biol*. 28, 964–971

32. Saha, I., Yuste-Checa, P., Padilha, M. D. S., Guo, Q., Körner, R., Holthusen, H., Trinkaus, V. A., Dudanova, I., Fernández-Busnadiego, R., Baumeister, W., Sanders, D. W., Gautam, S.,

Diamond, M. I., Hartl, F. U., and Hipp, M. S. (2023) The AAA+ chaperone VCP disaggregates Tau fibrils and generates aggregate seeds in a cellular system. *Nat Commun*. 14, 560

33. DeLaBarre, B., and Brunger, A. T. (2003) Complete structure of p97/valosin-containing protein reveals communication between nucleotide domains. *Nat Struct Mol Biol*. 10, 856–863
34. DeLaBarre, B., and Brunger, A. T. (2005) Nucleotide Dependent Motion and Mechanism of Action of p97/VCP. *J Mol Biol*. 347, 437–452
35. Rouiller, I., DeLaBarre, B., May, A. P., Weis, W. I., Brunger, A. T., Milligan, R. A., and Wilson-Kubalek, E. M. (2002) Conformational changes of the multifunction p97 AAA ATPase during its ATPase cycle. *Nat Struct Biol*. 9, 950–957
36. Banerjee, S., Bartesaghi, A., Merk, A., Rao, P., Bulfer, S. L., Yan, Y., Green, N., Mroczkowski, B., Neitz, R. J., Wipf, P., Falconieri, V., Deshaies, R. J., Milne, J. L. S., Huryn, D., Arkin, M., and Subramaniam, S. (2016) 2.3 Å resolution cryo-EM structure of human p97 and mechanism of allosteric inhibition. *Science*. 351, 871–875
37. Bodnar, N. O., and Rapoport, T. A. (2017) Molecular Mechanism of Substrate Processing by the Cdc48 ATPase Complex. *Cell*. 169, 722-735.e9
38. Twomey, E. C., Ji, Z., Wales, T. E., Bodnar, N. O., Ficarro, S. B., Marto, J. A., Engen, J. R., and Rapoport, T. A. (2019) Substrate processing by the Cdc48 ATPase complex is initiated by ubiquitin unfolding. *Science*. 365, eaax1033
39. Cooney, I., Han, H., Stewart, M. G., Carson, R. H., Hansen, D. T., Iwasa, J. H., Price, J. C., Hill, C. P., and Shen, P. S. (2019) Structure of the Cdc48 segregase in the act of unfolding an authentic substrate. *Science*. 365, 502–505
40. Stapf, C., Cartwright, E., Bycroft, M., Hofmann, K., and Buchberger, A. (2011) The General Definition of the p97/Valosin-containing Protein (VCP)-interacting Motif (VIM) Delineates a New Family of p97 Cofactors*. *J Biol Chem*. 286, 38670–38678
41. Buchberger, A., Howard, M. J., Proctor, M., and Bycroft, M. (2001) The UBX domain: a widespread ubiquitin-like module11Edited by P. E. Wright. *J Mol Biol*. 307, 17–24

42. Dreveny, I., Kondo, H., Uchiyama, K., Shaw, A., Zhang, X., and Freemont, P. S. (2004) Structural basis of the interaction between the AAA ATPase p97/VCP and its adaptor protein p47. *Embo J*. 23, 1030–1039

43. Li, Z., Wang, Y., Xu, M., and Jiang, T. (2017) Crystal structures of the UBX domain of human UBXD7 and its complex with p97 ATPase. *Biochem Bioph Res Co*. 486, 94–100

44. Hänzelmann, P., Buchberger, A., and Schindelin, H. (2011) Hierarchical Binding of Cofactors to the AAA ATPase p97. *Structure*. 19, 833–843

45. Lee, J.-J., Park, J. K., Jeong, J., Jeon, H., Yoon, J.-B., Kim, E. E., and Lee, K.-J. (2013) Complex of Fas-associated Factor 1 (FAF1) with Valosin-containing Protein (VCP)-Npl4-Ufd1 and Polyubiquitinated Proteins Promotes Endoplasmic Reticulum-associated Degradation (ERAD)*. *J Biol Chem*. 288, 6998–7011

46. Kim, S. J., Cho, J., Song, E. J., Kim, S. J., Kim, H. M., Lee, K. E., Suh, S. W., and Kim, E. E. (2014) Structural Basis for Ovarian Tumor Domain-containing Protein 1 (OTU1) Binding to p97/Valosin-containing Protein (VCP)*. *J Biol Chem*. 289, 12264–12274

47. Hänzelmann, P., and Schindelin, H. (2011) The Structural and Functional Basis of the p97/Valosin-containing Protein (VCP)-interacting Motif (VIM) MUTUALLY EXCLUSIVE BINDING OF COFACTORS TO THE N-TERMINAL DOMAIN OF p97*. *J Biol Chem*. 286, 38679–38690

48. Lim, J. J., Lee, Y., Ly, T. T., Kang, J. Y., Lee, J.-G., An, J. Y., Youn, H.-S., Park, K. R., Kim, T. G., Yang, J. K., Jun, Y., and Eom, S. H. (2016) Structural insights into the interaction of p97 N-terminus domain and VBM in rhomboid protease, RHBDL4. *Biochem J*. 473, 2863–2880

49. Lim, J. J., Lee, Y., Yoon, S. Y., Ly, T. T., Kang, J. Y., Youn, H., An, J. Y., Lee, J., Park, K. R., Kim, T. G., Yang, J. K., Jun, Y., and Eom, S. H. (2016) Structural insights into the interaction of human p97 N-terminal domain and SHP motif in Derlin-1 rhomboid pseudoprotease. *Febs Lett*. 590, 4402–4413

50. Blueggel, M., Boom, J. van den, Meyer, H., Bayer, P., and Beuck, C. (2019) Structure of the PUB Domain from Ubiquitin Regulatory X Domain Protein 1 (UBXD1) and Its Interaction with the p97 AAA+ ATPase. *Biomol*. 9, 876

51. Qiu, L., Pashkova, N., Walker, J. R., Winistorfer, S., Allali-Hassani, A., Akutsu, M., Piper, R., and Dhe-Paganon, S. (2010) Structure and Function of the PLAA/Ufd3-p97/Cdc48 Complex*. *J Biological Chem*. 285, 365–372

52. Allen, M. D., Buchberger, A., and Bycroft, M. (2006) The PUB Domain Functions as a p97 Binding Module in Human Peptide N-Glycanase*. *J Biol Chem*. 281, 25502–25508

53. Zhao, G., Zhou, X., Wang, L., Li, G., Schindelin, H., and Lennarz, W. J. (2007) Studies on peptide:N-glycanase–p97 interaction suggest that p97 phosphorylation modulates endoplasmic reticulum-associated degradation. *Proc National Acad Sci*. 104, 8785–8790

54. Arumughan, A., Roske, Y., Barth, C., Forero, L. L., Bravo-Rodriguez, K., Redel, A., Kostova, S., McShane, E., Opitz, R., Faelber, K., Rau, K., Mielke, T., Daumke, O., Selbach, M., Sanchez-Garcia, E., Rocks, O., Panáková, D., Heinemann, U., and Wanker, E. E. (2016) Quantitative interaction mapping reveals an extended UBX domain in ASPL that disrupts functional p97 hexamers. *Nat Commun*. 7, 13047

55. Bodnar, N. O., Kim, K. H., Ji, Z., Wales, T. E., Svetlov, V., Nudler, E., Engen, J. R., Walz, T., and Rapoport, T. A. (2018) Structure of the Cdc48 ATPase with its ubiquitin-binding cofactor Ufd1-Npl4. *Nat Struct Mol Biol*. 25, 616–622

56. Trusch, F., Matena, A., Vuk, M., Koerver, L., Knævelsrud, H., Freemont, P. S., Meyer, H., and Bayer, P. (2015) The N-terminal Region of the Ubiquitin Regulatory X (UBX) Domain-containing Protein 1 (UBXD1) Modulates Interdomain Communication within the Valosin-containing Protein p97. *J Biol Chem*. 290, 29414–27

57. Meyer, H. H., Shorter, J. G., Seemann, J., Pappin, D., and Warren, G. (2000) A complex of mammalian Ufd1 and Npl4 links the AAA-ATPase, p97, to ubiquitin and nuclear transport pathways. *Embo J*. 19, 2181–2192

58. Maric, M., Mukherjee, P., Tatham, M. H., Hay, R., and Labib, K. (2017) Ufd1-Npl4 Recruit Cdc48 for Disassembly of Ubiquitylated CMG Helicase at the End of Chromosome Replication. *Cell Reports*. 18, 3033–3042

59. Mosbech, A., Gibbs-Seymour, I., Kagias, K., Thorslund, T., Beli, P., Povlsen, L., Nielsen, S. V., Smedegaard, S., Sedgwick, G., Lukas, C., Hartmann-Petersen, R., Lukas, J., Choudhary, C., Pocock, R., Bekker-Jensen, S., and Mailand, N. (2012) DVC1 (C1orf124) is a DNA damage–targeting p97 adaptor that promotes ubiquitin-dependent responses to replication blocks. *Nat Struct Mol Biol*. 19, 1084–1092

60. Davis, E. J., Lachaud, C., Appleton, P., Macartney, T. J., Näthke, I., and Rouse, J. (2012) DVC1 (C1orf124) recruits the p97 protein segregase to sites of DNA damage. *Nat Struct Mol Biol*. 19, 1093–1100

61. Ghosal, G., Leung, J. W.-C., Nair, B. C., Fong, K.-W., and Chen, J. (2012) Proliferating Cell Nuclear Antigen (PCNA)-binding Protein C1orf124 Is a Regulator of Translesion Synthesis*. *J Biol Chem*. 287, 34225–34233

62. Rao, B., Li, S., Yao, D., Wang, Q., Xia, Y., Jia, Y., Shen, Y., and Cao, Y. (2021) The cryo-EM structure of an ERAD protein channel formed by tetrameric human Derlin-1. *Sci Adv*. 7, eabe8591

63. Fang, S., Ferrone, M., Yang, C., Jensen, J. P., Tiwari, S., and Weissman, A. M. (2001) The tumor autocrine motility factor receptor, gp78, is a ubiquitin protein ligase implicated in degradation from the endoplasmic reticulum. *Proc National Acad Sci*. 98, 14422–14427

64. Tang, W. K., Zhang, T., Ye, Y., and Xia, D. (2017) Structural basis for nucleotide-modulated p97 association with the ER membrane. *Cell Discov*. 3, 17045

65. Hou, X., Wei, H., Rajagopalan, C., Jiang, H., Wu, Q., Zaman, K., Xie, Y., and Sun, F. (2018) Dissection of the Role of VIMP in Endoplasmic Reticulum-Associated Degradation of CFTRΔF508. *Sci Rep-uk*. 8, 4764

66. Cheng, Y. (2015) Single-Particle Cryo-EM at Crystallographic Resolution. *Cell*. 161, 450–457

67. Xu, Y., Han, H., Cooney, I., Guo, Y., Moran, N. G., Zuniga, N. R., Price, J. C., Hill, C. P., and Shen, P. S. (2022) Active conformation of the p97-p47 unfoldase complex. *Nat Commun*. 13, 2640

68. Scheres, S. H. W. (2016) Processing of Structurally Heterogeneous Cryo-EM Data in RELION, pp. 125–157, Methods in Enzymology, Elsevier, 579, 125–157

69. Varadi, M., Anyango, S., Deshpande, M., Nair, S., Natassia, C., Yordanova, G., Yuan, D., Stroe, O., Wood, G., Laydon, A., Žídek, A., Green, T., Tunyasuvunakool, K., Petersen, S., Jumper, J., Clancy, E., Green, R., Vora, A., Lutfi, M., Figurnov, M., Cowie, A., Hobbs, N., Kohli, P., Kleywegt, G., Birney, E., Hassabis, D., and Velankar, S. (2021) AlphaFold Protein Structure Database: massively expanding the structural coverage of protein-sequence space with high-accuracy models. *Nucleic Acids Res*. 50, D439–D444

70. Jumper, J., Evans, R., Pritzel, A., Green, T., Figurnov, M., Ronneberger, O., Tunyasuvunakool, K., Bates, R., Žídek, A., Potapenko, A., Bridgland, A., Meyer, C., Kohl, S. A. A., Ballard, A. J., Cowie, A., Romera-Paredes, B., Nikolov, S., Jain, R., Adler, J., Back, T., Petersen, S., Reiman, D., Clancy, E., Zielinski, M., Steinegger, M., Pacholska, M., Berghammer, T., Bodenstein, S., Silver, D., Vinyals, O., Senior, A. W., Kavukcuoglu, K., Kohli, P., and Hassabis, D. (2021) Highly accurate protein structure prediction with AlphaFold. *Nature*. 596, 583–589

71. Baek, M., DiMaio, F., Anishchenko, I., Dauparas, J., Ovchinnikov, S., Lee, G. R., Wang, J., Cong, Q., Kinch, L. N., Schaeffer, R. D., Millán, C., Park, H., Adams, C., Glassman, C. R., DeGiovanni, A., Pereira, J. H., Rodrigues, A. V., Dijk, A. A. van, Ebrecht, A. C., Opperman, D. J., Sagmeister, T., Buhlheller, C., Pavkov-Keller, T., Rathinaswamy, M. K., Dalwadi, U., Yip, C. K., Burke, J. E., Garcia, K. C., Grishin, N. V., Adams, P. D., Read, R. J., and Baker, D. (2021) Accurate prediction of protein structures and interactions using a three-track neural network. *Science*. 373, 871–876

72. Lin, Z., Akin, H., Rao, R., Hie, B., Zhu, Z., Lu, W., Smetanin, N., Verkuil, R., Kabeli, O., Shmueli, Y., Costa, A. dos S., Fazel-Zarandi, M., Sercu, T., Candido, S., and Rives, A. (2022) Evolutionary-scale prediction of atomic level protein structure with a language model. *Biorxiv*. 10.1101/2022.07.20.500902

73. Conicella, A. E., Huang, R., Ripstein, Z. A., Nguyen, A., Wang, E., Löhr, T., Schuck, P., Vendruscolo, M., Rubinstein, J. L., and Kay, L. E. (2020) An intrinsically disordered motif regulates the interaction between the p47 adaptor and the p97 AAA+ ATPase. *Proc National Acad Sci*. 117, 26226–26236

74. Petrović, S., Roske, Y., Rami, B., Phan, M. H. Q., Panáková, D., and Heinemann, U. (2023) Structural remodeling of AAA+ ATPase p97 by adaptor protein ASPL facilitates posttranslational methylation by METTL21D. *Proc National Acad Sci*. 120, e2208941120

Chapter 2

The p97/VCP adapter UBXD1 drives AAA+ remodeling and ring opening through multi-domain tethered interactions

Contributing Authors:

Julian R. Braxton[1,2], Chad R. Altobelli[1,3], Maxwell R. Tucker[2,4], Eric Tse[2], Aye C. Thwin[2], Michelle R. Arkin[3], and Daniel R. Southworth[2]

[1]Graduate Program in Chemistry and Chemical Biology; University of California, San Francisco; San Francisco, CA 94158, USA

[2]Department of Biochemistry and Biophysics and Institute for Neurodegenerative Diseases; University of California, San Francisco; San Francisco, CA 94158, USA

[3]Department of Pharmaceutical Chemistry and Small Molecule Discovery Center; University of California, San Francisco; San Francisco, CA 94158, USA

[4]Graduate Program in Biophysics; University of California, San Francisco; San Francisco, CA 94158, USA

Abstract

p97/VCP is an essential cytosolic AAA+ ATPase hexamer that extracts and unfolds substrate polypeptides during protein homeostasis and degradation. Distinct sets of p97 adapters guide cellular functions but their roles in direct control of the hexamer are unclear. The UBXD1 adapter localizes with p97 in critical mitochondria and lysosome clearance pathways and contains multiple p97-interacting domains. We identify UBXD1 as a potent p97 ATPase inhibitor and report structures of intact p97:UBXD1 complexes that reveal extensive UBXD1 contacts across p97 and an asymmetric remodeling of the hexamer. Conserved VIM, UBX, and PUB domains tether adjacent protomers while a connecting strand forms an N-terminal domain lariat with a helix wedged at the interprotomer interface. An additional VIM-connecting helix binds along the second AAA+ domain. Together these contacts split the hexamer into a ring-open conformation. Structures, mutagenesis, and comparisons to other adapters further reveal how adapters containing conserved p97-remodeling motifs regulate p97 ATPase activity and structure.

Introduction

p97 (also called valosin-containing protein or VCP) is a AAA+ (ATPases Associated with diverse cellular Activities) molecular chaperone unfoldase with critical functions in many cellular processes including membrane fusion, chromatin remodeling, and protein homeostasis (proteostasis) (1, 2). Reflecting its critical roles in the cell, missense mutations in p97 cause multisystem proteinopathy (MSP, also called IBMPFD), amyotrophic lateral sclerosis, and vacuolar tauopathy, all characterized by defects in protein quality control and clearance pathways (3–5). Additionally, p97 is under investigation as a cancer target due to its central roles in maintaining proteostasis, and is upregulated in many carcinomas (6, 7). The central mechanism of p97 that governs its diverse activities is the extraction of proteins from macromolecular complexes and membranes through hydrolysis-driven substrate translocation (8, 9). This process frequently facilitates substrate degradation by the 26S proteasome, as in the endoplasmic

reticulum-associated degradation (ERAD) and ribosome quality control pathways (10, 11). In less-understood pathways, p97 enables autophagic clearance of endosomes and damaged organelles such as lysosomes or mitochondria, potentially by regulatory remodeling of their surface proteomes (12–14). p97 functions are directed by more than 30 adapter proteins that bind p97 to facilitate substrate delivery, control subcellular localization, and couple additional substrate processing functions such as deubiquitylation (15). Thus, the many possible adapter interaction combinations may in part drive p97 functional diversity (16). Some of these adapters are well-characterized, for example, the ERAD-related UFD1/NPL4 and YOD1 recruit ubiquitylated substrates to p97 and catalyze ubiquitin chain removal, respectively (10). However, the function of many adapters, such as the mitophagy- and lysophagy-related UBXD1, is unknown (12, 17).

p97 forms homohexamers that enclose a central channel through which unfolded proteins are threaded; each protomer consists of two AAA+ ATPase domains (D1 and D2), an N-terminal domain (NTD), and an unstructured C-terminal (CT) tail (18). Initial structures of full-length or truncated p97 revealed a planar, symmetric hexamer in which the NTD adopts an ‘up’ conformation when D1 is bound to ATP, or a ‘down’ conformation co-planar with the ADP-bound D1 ring (18–24). More recent substrate-bound structures revealed that the hexamer adopts a right-handed spiral with the conserved pore loops in D1 and D2 extending into the channel, contacting the substrate polypeptide in a manner similar to many AAA+ translocase complexes (8, 9, 25–27). Based on comparisons with related AAA+s, p97 may extract and unfold substrates by a similar processive ‘hand over hand’ mechanism involving stepwise cycles of substrate binding and release (26–29). However, given its diverse pathways and the central involvement of numerous adapters, alternate translocation paths may occur, potentially for processing substrates with complex topologies including those bearing branched ubiquitin chains (16). Notably, substrate recognition and engagement are largely dependent on p97-adapter coordination (15),

yet with the exceptions of UFD1/NPL4 (9, 30, 31) and p37 (32–34), little is known about the mechanism by which adapters control p97 activity to enable these processes.

UBXD1 is a p97 adapter implicated in the autophagic clearance of damaged mitochondria and lysosomes, among other functions (12, 14, 17, 35, 36). MSP mutations impair UBXD1 binding and affect its associated cellular functions, demonstrating the importance of this adapter in multiple p97 pathways, but its function in p97 substrate processing is unknown (14, 37, 38). UBXD1 contains three structurally defined p97 interaction motifs, but no known enzymatic or substrate interaction activities. A conserved VIM (VCP-interacting motif) helix interacts with the p97 NTD, while the PUB (peptide:*N*-glycanase and UBA or UBX-containing proteins) domain interacts with the CT tail (36, 39–42). Notably, UBXD1 contains a canonical UBX (ubiquitin regulatory X) domain that is also expected to bind the NTD. However, it is unclear how the VIM and UBX could function together given the overlapping binding sites. Moreover, the UBX domain is reported to not interact with p97 potentially due to changes in binding pocket residues compared to other UBX domains (17, 39, 43). Crystal structures of p97 truncations in complex with VIM, UBX, and PUB domains from other adapters have provided insight into isolated p97-adapter interactions, but how all these domains function together in an intact p97:UBXD1 complex is unknown. Furthermore, UBXD1 is the only known p97 adapter with both N- and C-terminal-interacting domains; this feature, coupled with the absence of substrate-binding domains and multiple NTD-interacting domains, raises key questions about the arrangement of UBXD1 on p97 hexamers, its binding stoichiometry, and effect on p97 structure and function.

To address these questions, we determined high-resolution cryo-EM structures of p97 in complex with full-length UBXD1. The structures reveal multiple stoichiometric arrangements of UBXD1 that involve extensive contacts with p97 via its VIM, PUB, and UBX domains, as well as previously uncharacterized helices. Remarkably, in singly-bound states, UBXD1 interacts across three p97 protomers, dramatically remodeling the planar p97 hexamer into a partial spiral, open-

ring state in which the separated protomers remain tethered by UBXD1. A lariat structure wraps around an NTD with two helices interacting at the protomer interface, functioning as a wedge that displaces D1 interprotomer contacts, while a short helix adjacent to the VIM alters the D2 conformation. These UBXD1 interactions coincide with a potent loss of p97 ATPase activity. Together with mutagenesis and additional structural characterization, this work reveals distinct roles for the UBXD1 domains and identifies how a network of protein-protein adapter interactions coordinate to remodel p97 structure and control function.

Results

Structures of p97:UBXD1 reveal extensive interactions and hexamer remodeling

In addition to the canonical VIM, UBX, and PUB domains, UBXD1 is also identified to contain transiently structured helices, here referred to as H1/H2 (residues 1-25) and H4 (residues 75-93), that weakly interact with p97 (36, 37) as well as additional uncharacterized regions (residues 278-334). To further investigate the predicted structure of full-length UBXD1, we analyzed the AlphaFold model (44, 45), which revealed structures for the canonical domains, H1/H2, H4, and an additional four-helical element between the PUB and UBX, while the remaining sequence appears unstructured (**Figure 2.1A,B**). The four-helical region hereinafter is referred to as the helical lariat based on our structural analysis and homology to the ASPL adapter (see below) (46). Notably, this AlphaFold analysis indeed predicts structures for uncharacterized regions across UBXD1 that, in addition to the VIM, UBX, and PUB, may interact with p97 and contribute to UBXD1 function.

To analyze the p97-UBXD1 interaction, we first determined the effect of UBXD1 on p97 ATPase activity using full-length, wild-type, human proteins (**Figure 2.1C**). This revealed a potent inhibitory activity, with an IC_{50} of ~25 nM for UBXD1. We next analyzed the nucleotide dependence of the p97-UBXD1 interaction, as many adapters exhibit nucleotide binding specificity to p97 that is related to the up/down conformational plasticity of the NTDs (37, 47, 48).

By analytical size exclusion chromatography (SEC) we identify that following incubation with either ADP or the slowly hydrolyzable ATP analog ATPγS, UBXD1 co-elutes with p97 in fractions slightly shifted from the hexamer peak, indicating complex formation under both nucleotide conditions (**Figure 2.S1A,B**). A modest shift in elution is identified with ADP compared to ATPγS, however both nucleotide-bound states appear to support UBXD1 binding under these conditions, indicating UBXD1 may interact irrespective of the NTD state. Nonetheless, based on the reduced band intensity of UBXD1 compared to p97, UBXD1 binding appears to be sub-stoichiometric with respect to p97 hexamer despite incubations at high concentration (20 and 10 μM, respectively). A previous study reported that UBXD1 binds p97 sub-stoichiometrically, but with a modest affinity (K_D ~3.5 μM), consistent with our SEC results (41). However, we predict a much higher binding affinity based on the ~25 nM IC_{50} for ATPase inhibition we identify (**Figure 2.1C**).

Based on these results and the reported increased NTD stability in the ADP state (19), p97:UBXD1 cryo-EM samples were first prepared with saturating concentrations of ADP (5 mM). Reference-free two-dimensional (2D) class averages show well-defined top and side views of the p97 hexamer with the NTDs in the down conformation and co-planar with the D1 ring, as expected based on the presence of ADP (**Figure 2.1D** and **Figure 2.S1C**). However, additional density around the hexamer was not identified in these initial classifications. Considering potential UBXD1 flexibility and binding heterogeneity could impact 2D analysis, rounds of three-dimensional (3D) classification were performed next with a large (~5.5 million particle) dataset in order to better classify potential bound states. Following an initial classification, three well-defined states were identified. Classes 1 and 2 contained additional globular density likely corresponding to the UBX domain of UBXD1 while class 3 appeared as a well-resolved p97 hexamer without the additional globular density (**Figure 2.S1D**). Subsequent classification and refinement of the UBX-containing states enabled high-resolution structure determination (3.3-3.5 Å) of p97:UBXD1 in two configurations termed p97:UBXD1^{closed} and p97:UBXD1^{open} (**Figure 2.1E,F**, **Table 2.1**). Individual

p97 protomers are denoted counterclockwise P1-P6 based on asymmetry of p97:UBXD1^{open}. Additional UBXD1 binding configurations were identified in the classification and further characterized (see below and **Figure 2.S1D**). Notably, the singly-bound closed and open states exhibit the most p97 conformational changes and extensive contacts by UBXD1 and thus are largely the focus of this study. Analysis of the closed and open states revealed that the protomers unbound to UBXD1 were well-resolved, while protomers P1 and P6 contain additional density corresponding to UBXD1 and comprise a flexible seam that in the open state is more poorly resolved relative to the rest of the hexamer (**Figure 2.1E,F**). Therefore, focused classification and local refinement of P1 and P6 in the open state was performed separately to improve the resolution of these regions, and a composite map was generated (**Figure 2.S1D** and methods). High-resolution map features in both the closed and open states enabled building of atomic models for both structures, and the UBXD1 domains predicted to be structured by the AlphaFold model are all identified except H1/H2 and H4 (**Figure 2.1E,F**, **Figure 2.S2A-D,K**, and **Movie 2.1**).

The p97 domains are well resolved in both structures with the NTDs adopting the down conformation and density corresponding to bound ADP is present in all D1 and D2 nucleotide pockets and coordinated by conserved AAA+ residues (**Figure 2.S1E-G**). In the p97:UBXD1^{closed} structure the D1 and D2 are in a planar, double ring conformation and one molecule of UBXD1 is identified, binding across protomers P1 and P6. For the p97:UBXD1^{open} structure a single UBXD1 is similarly bound but the protomer-protomer interface between P1 and P6 is separated by ~8 Å relative to p97:UBXD1^{closed}, creating an open-ring arrangement of the p97 hexamer. For both structures, strong density corresponding to the VIM and UBX domains is observed, as well as for two previously uncharacterized helices and an associated N-terminal linker (**Figure 2.1E,F**). Together, these helices and linker encircle the NTD of the P6 protomer, forming a helical lariat (discussed below). At lower density threshold, the PUB domain becomes apparent and is positioned below the UBX, adjacent to the p97 D2 ring, but appears to make no substantial contact

with the hexamer, likely resulting in significant flexibility and explaining the lower resolution (**Figure 2.1G**). Weak density resembling the VIM is also present in the NTDs of P2-P5 in both the closed and open states, indicating partial binding to these protomers, which is likely a consequence of protein concentrations needed for cryo-EM (**Figure 2.S1H**). Overall, these structures indicate that UBXD1 binding drives conformational changes and ring opening at a protomer interface that is tethered by multi-domain interactions involving the VIM, UBX, and a lariat structure across the two seam protomers.

Additional structures identify alternate UBXD1 binding stoichiometries and nucleotide-dependent hexamer remodeling

During 3D classification additional structures with different UBXD1 configurations were identified (**Figure 2.S1D,I**, **Figure 2.S2**, and **Table 2.1**). A prevalent class in the initial classification, termed p97:UBXD1^{VIM}, closely resembles the structure of the planar ADP-bound p97 (Cα root-mean-square deviation (RMSD) = 1.0 Å) (19), but features additional helical density in the NTD cleft of all protomers that corresponds to the UBXD1 VIM (**Figure 2.S1I**). Similar to P2 through P5 in the closed and open states, we surmise that under our *in vitro* conditions VIM binding predominates for this class, potentially displacing the UBX and other contacts. Notably, given the identical hexamer arrangement compared to p97^{ADP}, we conclude that VIM interactions on their own are insufficient to induce conformational rearrangements in p97. Subclassification additionally revealed two more minor states, termed p97:UBXD1^{meta} and p97:UBXD1^{para}, in which density for the VIM, PUB, lariat, and UBX are also observed at other positions (across P2-P3 or P3-P4, respectively) in the p97 hexamer, in conformations similar to p97:UBXD1^{closed} (**Figure 2.S1D,I**). These structures reveal that two UBXD1 molecules can bind the hexamer with productive VIM, UBX, and lariat interactions when properly spaced to allow for binding across two adjacent protomers. Notably, for all classifications the p97 open ring is only observed in the singly-bound

UBXD1 configuration, indicating that this conformation is specifically driven by one fully-bound UBXD1 per p97 hexamer.

We identify UBXD1 also binds p97 in the presence of ATPγS, but with a reduced shift in elution volume compared to ADP (**Figure 2.S1A,B**). Therefore, we next sought to determine the extent of UBXD1-mediated structural remodeling of p97 in its ATP state. Cryo-EM analysis revealed three predominant classes: a UBXD1-bound hexamer closely resembling the closed state from the ADP dataset, a symmetric hexamer with NTDs in the up, ATP conformation and no density for UBXD1, and a symmetric hexamer with 'down' NTDs and VIM density, similar to the VIM-only state from the ADP dataset (**Figure 2.S3A**). Notably, no state analogous to the open p97:UBXD1 complex was identified. Refinement of these states allowed for the unambiguous assignment of ATPγS for density in all nucleotide-binding pockets (**Figure 2.S3B,C**). The observation of 'down' NTDs in ATPγS-bound D1 domains is striking, indicating that UBXD1 interactions may override nucleotide-promoted NTD conformation, a finding not previously described in intact complexes. Indeed, the NTD-down arrangement is identified even in the VIM-only state with ATPγS, suggesting that interaction by the UBXD1 VIM alone is sufficient to regulate p97 NTD conformation. In sum, these results suggest that while UBXD1 readily binds p97 in the ATP state, the interactions are insufficient to promote full ring opening, as observed with ADP. The absence of an open state may be due to increased inter-protomer interactions and hexamer stability, such as through trans-arginine finger contacts with the γ-phosphate. Indeed, in substrate-bound AAA+ complexes, hydrolysis at the spiral seam is thought to destabilize the interprotomer interface, facilitating substrate release and rebinding during stepwise translocation (49). Our findings therefore indicate that UBXD1 may function during the p97 catalytic cycle by promoting ring opening specifically in a post-hydrolysis state.

UBXD1 drives large D1-D2 conformational changes that open the p97 hexamer ring

To identify conformational changes in ADP-bound p97 complexes that are driven by UBXD1 binding, the p97:UBXD1^{closed} and p97:UBXD1^{open} structures were aligned to the previously published structure of ADP-bound p97 (19). RMSD values reveal extensive changes across the D1 and D2 for the seam protomers (P1 and P6) in both UBXD1-bound states (**Figure 2.2A,B** and **Figure 2.S4A,B**). While P1 and P6 are similarly rotated away from each other in both states, the magnitudes of these displacements are larger in the open state, resulting in the observed disruption of the protomer interface. This indicates that these states are intermediates in the same conformational path of hexamer opening (**Movie 2.2**). Additionally, while the hexamer in the closed state is planar and resembles substrate-free structures, the open state has a right-handed spiral with an overall elevation change of 7 Å (**Figure 2.2C**). This is largely due to a significant 9° downward rotation of P1, which has the largest RMSD values of any protomer in either state (**Figure 2.2C**). In addition to the movements of entire protomers, there is a notable rotation between the small and large subdomains of the D2 in protomer P1 in both the closed and open states (**Figure 2.2D**). This rotation is particularly evident in the open state, where the small subdomain is rotated upward by 10° relative to p97^{ADP} and 12° relative to p97:UBXD1^{closed} (**Figure 2.2D**). This rotation, and the separation of P1 and P6, causes a small helix (α5') (18, 24) mediating contact between the D2 domains of the seam protomers to disappear from the density map, likely as a result of increased flexibility; this helix is normally positioned on top of α12' of the D2 domain of the counterclockwise protomer (**Figure 2.S4C** and **Figure 2.2B**).

Notably, the P1-P6 conformational changes are different across the D1 and D2 domains (**Figure 2.2E**). In the closed state the D1 domains of P1 and P6 are separated by 3 Å relative to p97^{ADP}, while there is negligible D2 separation. In the open state the D1 and D2 domains are separated by 8 Å and 11 Å, respectively. These changes dramatically remodel the nucleotide binding pockets of P1 by displacing the arginine fingers from P6 (**Figure 2.2D**). These separations

likely preclude ATP hydrolysis in P1, which could explain the ATPase inhibition observed biochemically (**Figure 2.1C**). Additionally, due to the expansion of the P1-P6 interface in the open state, contacts between other protomers are compressed: the average rotation between adjacent protomers is 57°, or 3° smaller than the angle in a perfectly symmetric hexamer. These compressions could potentially cause subtle deformations of nucleotide binding pocket geometry, which could also impair hydrolysis. Finally, to confirm the spiral architecture of the open state, 3D variability analysis was performed jointly on particles from the closed and open states (**Movie 2.3**). This reveals the transition from a planar UBXD1-bound hexamer to a spiral, indicating that the closed and open states are likely in equilibrium and UBXD1 binding splits the p97 hexamer at P1-P6, causing all protomers to rotate along the hexamer C6 symmetry axis.

Canonical interactions by the VIM, UBX and PUB indicate binding across three protomers of p97

The p97:UBXD1^{closed} and p97:UBXD1^{open} structures reveal high-resolution views of p97 bound to an adapter containing conserved VIM, UBX, and PUB domains, revealing how these domains together coordinate interactions across the hexamer. In contrast to previous binding studies (17, 39, 43), both the VIM and UBX interact with p97, making canonical interactions with adjacent NTDs (**Figure 2.3**). The 18-residue VIM helix is positioned in the NTD cleft of P1, similar to structures of isolated domains, but is distal to other UBXD1 density, and comprises the only major contact with the P1 protomer (**Figure 2.3A,B** and **Figure 2.S5A,B**). Notably, a conserved Arg residue (R62) required for p97 binding projects into the NTD in a manner similar to that of other NTD-VIM complexes, potentially forming a salt bridge with D35 of the NTD and a hydrogen bond with the backbone carbonyl of A142 (41). The VIM appears anchored at its N-terminus by an additional salt bridge between E51 of UBXD1 and K109 of the NTD and by hydrogen bonding between the backbone carbonyl of E51 and Y143 of the NTD. Additional hydrophobic contacts along the VIM could further stabilize this interaction (**Figure 2.3B**, right panel).

The UBX domain is bound to the NTD of the clockwise protomer (P6) in a manner similar to UBX-NTD structures from other adapter proteins (**Figure 2.3C,D** and **Figure 2.S5C,D**). This is surprising because the canonical Phe-Pro-Arg p97-interacting motif located on the S3/S4 loop is replaced by Ser-Gly-Gly in UBXD1, thus eliminating electrostatic and hydrophobic interactions identified in other structures (15). However, another Arg residue important for interaction with p97, R342, is conserved in UBXD1, and likely hydrogen bonds with the backbone carbonyl of P106. While the UBX in this structure contains the canonical β-grasp fold characteristic of all UBX domains, it features an additional β-strand (Uβ0) proximal to the N-terminal lobe of the NTD (Nn) that connects the PUB to the UBX to the helical lariat (**Figure 2.3E**). Additionally, a C-terminal extension consisting of two alpha helices (UBX helices 2 and 3, hereafter referred to as Uα2 and Uα3) connected by unstructured linkers is positioned on the apical surface of the canonical UBX and wraps over the β-sheet. Finally, a potential salt bridge between K419 of Uα2 and D179 of the NTD could also stabilize the UBX-NTD interaction.

The PUB domain binds the HbYX (hydrophobic, Tyr, any amino acid) motif located at the end of the flexible p97 CT tail (40). Density for this domain is more poorly resolved in both the closed and open structures, which prompted us to perform focused classification of this region (**Figure 2.S1D**). Two resulting classes show improved definition for the PUB, enabling the AlphaFold model for this region to be fit unambiguously into the density (**Figure 2.S5E,F**). In class 1 (hereafter referred to as p97:UBXD1-PUB_{out}), the PUB domain is positioned similarly to that in the closed model, projecting straight downward from the UBX domain. In class 2 (hereafter referred to as p97:UBXD1-PUB_{in}) the PUB domain is rotated 46° about a linker connecting the PUB and UBX domains, and points towards P6 (**Figure 2.3F**, **Figure 2.S2**, **Figure 2.S5F**, and **Table 2.1**). In this class strong connecting density is observed between the PUB and the bottom surface of P6, indicative of binding to a p97 CT tail (**Figure 2.3G,H**). Notably, these tails project across the base of the adjacent counterclockwise protomer, such that UBXD1 density on P6 is

closest to the P5 tail, not that of P6. Thus, the position of the PUB domain in p97:UBXD1-PUB$_{in}$ indicates binding to the P5 tail (**Figure 2.3G,H**). Inspection of the p97:UBXD1-PUB$_{out}$ map reveals weak density suggestive of a similar P5-PUB interaction, indicating that the CT tail may remain bound in multiple PUB conformations (**Figure 2.S5H-K**), though the strongest density is present in p97:UBXD1-PUB$_{in}$. In sum, a single molecule of UBXD1 appears to interact across three p97 protomers (P1, P5, and P6) simultaneously through interactions by the VIM, UBX and PUB domains (**Figure 2.3I**). These extensive interactions with both faces of the p97 hexamer are a remarkable feature of UBXD1, and are unique among all adapters currently structurally characterized.

The UBXD1 helical lariat and H4 make distinct p97 D1-D2 interprotomer interactions

The UBXD1 helical lariat is among the most striking structural features of the p97:UBXD1 complexes due to its intimate interaction with all three domains of the P6 protomer (**Figure 2.4A-E** and **Figure 2.S6A**). Based on the AlphaFold prediction and what is resolved in our structures, it is composed of four helices (hereafter referred to as Lα1-4) that are inserted between Uβ0 and Uβ1 of the UBX domain. Together, these helices completely encircle the P6 NTD (**Figure 2.4A**). Lα1 and Lα2 are positioned along the top of the P6 NTD, while the longer Lα3 and Lα4 helices bind at the P6-P1 protomer interface. Lα3 is situated at the D1 interface, and makes numerous electrostatic contacts with residues in both the N-terminal and D1 domains of P6, as well as minor hydrophobic contacts with the D1 domain of P1 (**Figure 2.4B,C**). Lα4 is positioned proximal to the D2 domain, and connects back to the UBX domain, completing the lariat. A salt bridge involving K325 of Lα4 and E498 of the D2 domain is the only significant contact this helix makes with p97. Lα2 also contacts the NTD using two Phe residues (F292 and F293) that project into the NTD, making van der Waals contacts with K62, V99, and R25 (**Figure 2.4D**). A short loop connects Lα3 and Lα4, and anchors the lariat into the D2 domain using residues L317 and T319 (**Figure 2.4B,E**). Additionally, the Lα3-Lα4 arrangement is stabilized by a tripartite electrostatic

network involving R313 of Lα3, R318 of the Lα3-Lα4 loop, and E326 of Lα4 (**Figure 2.4E**). Considering the interaction of Lα3 along the D1 domain of P6 displaces typical D1-D1 contacts between P1 and P6, we postulate these contacts likely contribute substantially to the D1 conformational changes and ring-opening identified in the closed and open states of p97. Interestingly, the binding site of the linker between Lα3 and Lα4 overlaps with that of the p97 allosteric inhibitor UPCDC30245 (19), suggesting that occupancy of this site is a productive means to alter p97 function (**Figure 2.S6B**).

Further classification of p97:UBXD1^{closed}, which was chosen due to the reduced flexibility compared to the open state, was performed to potentially resolve additional regions reported to interact with p97 (36, 37), including H1/H2 and H4 (**Figure 2.S1D**). This analysis revealed an additional state with an overall similar conformation to p97:UBXD1^{closed}, but features low-resolution density on top of the D2 domain of the P1 protomer (**Figure 2.4F**, **Figure 2.S2**, and **Table 2.1**). This region likely corresponds to H4 because of its proximity to the C-terminus of the VIM, which is predicted to be connected to H4 by a 7-residue linker (**Figure 2.1B**). Indeed, the H4 helix docks well into this density, albeit the resolution was not sufficient for its precise orientation (**Figure 2.S6C**). In this structure (p97:UBXD1^{H4}), H4 binding is associated with an upward rigid body rotation of the D2 small subdomain by ~17° relative to the analogous domain in the closed state (**Figure 2.4G** and **Movie 2.4**). This upward rotation displaces a short helix (α5') from the D2 domain of P6, and therefore breaks D2-D2 contacts between the seam protomers. As in p97:UBXD1^{open}, α5' is not present in the density map, likely due to increased flexibility (**Figure 2.S6D**). Notably, a similar rotation of the D2 small subdomain of P1 is identified in p97:UBXD1^{open}, supporting potential H4 occupancy (**Figure 2.2E**). This prompted further inspection of the experimental density for this state. Indeed, weak density positioned atop the D2 domain was identified by examining the open state map at a low threshold, in a similar position as in p97:UBXD1^{H4} (**Figure 2.S6E**). This indicates that H4 may be associated with the hexamer

during ring opening, and places p97:UBXD1^{H4} as an intermediate between the closed and open states. Based on this analysis, we predict that H4 interactions play a key role in weakening the D2 interprotomer contacts, thereby driving localized opening of the D2 ring.

The helical lariat and H4 are conserved p97-remodeling motifs

Given the striking rearrangements of the p97 hexamer driven by UBXD1, efforts were undertaken to identify other p97 adapters with helical lariat or VIM-H4 motifs that could similarly remodel p97 contacts. To this end, Dali searches (50) against all structures in the Protein Data Bank and against the AlphaFold database were performed, first using the UBXD1 UBX-helical lariat structure as an input. This search revealed one protein, alveolar soft part sarcoma locus (ASPL, also called TUG or UBXD9), with a highly similar UBX-helical lariat arrangement (**Figure 2.5A** and **Figure 2.S7A**). Comparison of p97:UBXD1 structures determined here to structures of a heterotetramer of a truncated ASPL construct bound to p97 (46) reveal a conserved interaction with p97 (**Figure 2.5B**). The FF motif in Lα2, as well as the highly charged nature of the helices corresponding to Lα3 and Lα4, are conserved in ASPL (**Figure 2.S7A**). Intriguingly, ASPL also inhibits p97 ATPase activity, and has been demonstrated to completely disassemble p97 hexamers into smaller oligomers and monomers (46, 51). However, the construct used for structure determination lacks several other p97-interacting domains, leaving unclear the effect on hexamer remodeling in the context of the full-length protein. While we find no evidence of a similar hexamer disruption in UBXD1 based on our SEC or cryo-EM analysis (**Figure 2.S1A-C**), the split ring of the p97:UBXD1^{open} structure is compelling as a related function of the UBX-helical lariat in the context of UBXD1 with its additional p97 binding domains.

Dali searches using the VIM-H4 motif did not produce any significant hits, likely due to the structural simplicity of this region. However, examination of other adapters for unannotated structural elements proximal to a VIM suggested that the p97 adapter small VCP/p97-interacting protein (SVIP) might harbor an additional helix in a similar arrangement as in the VIM-H4 of

UBXD1 (52). SVIP is a 77-residue minimal adapter that inhibits p97-dependent functions in ERAD, among other functions (52–54). The SVIP VIM helix is reported to significantly contribute to p97 binding (42), though a previous study has suggested that additional elements might confer binding affinity (41). Though no structures of SVIP have been reported, the AlphaFold model of SVIP indeed predicts the VIM helix, as well as an adjacent helix with modest similarity to the UBXD1 H4 (**Figure 2.5C** and **Figure 2.S7B**). Given the predicted structural similarity to UBXD1 and inhibition of specific cellular functions, we hypothesized that SVIP may similarly remodel p97 D2 contacts and inhibit ATPase activity.

We next purified a previously characterized ASPL construct (ASPL-C, see methods) (46) and SVIP and analyzed their effect on p97 ATPase activity. ASPL-C potently inhibits p97 ATPase activity, with an IC_{50} of ~97 nM (**Figure 2.5D**). Notably, the complete loss of activity at high ASPL-C concentrations and highly cooperative inhibition (Hill slope ~3) are likely a consequence of hexamer disassembly, as has been previously reported (46). SVIP also strongly inhibits p97 ATPase activity (IC_{50} ~72 nM). This is striking given its minimal size and indicates that the predicted helix C-terminal to the VIM may contribute to ATPase inhibition through additional interactions with p97. Together these results support a functional conservation between UBXD1, ASPL and SVIP through the inhibition of p97 ATPase activity. Based on our structures and comparison to ASPL and SVIP we postulate that the helical lariat and the H4 helix function as noncanonical control elements that, when paired with well-conserved binding motifs such as UBX and VIM, serve critical functions in ATPase control and p97 remodeling.

To further investigate the helical lariat and H4 in UBXD1, mutations were introduced into the full-length UBXD1 sequence (**Figure 2.S7C** and methods), and their effect on p97 ATPase activity and structure was determined. We also constructed a double mutant containing both the lariat and H4 changes. Analytical SEC revealed that these constructs bound p97 to a similar extent as did wild-type UBXD1 (**Figure 2.S7D,E**). When tested for p97 ATPase inhibition, the

lariat mutant (LX) only modestly increased the IC_{50} compared to wild-type UBXD1 (25 nM to 41 nM), indicating its disruption alone does not abolish ATPase inhibition (**Figure 2.5E**). The IC_{50} for the H4 mutant (H4X) was also only modestly shifted compared to wild-type (37 nM vs. 25 nM, respectively); rather, the major effect was a ~60% increase in p97 ATPase activity at maximal inhibition (0.42 compared to 0.26 for wild type) (**Figure 2.5E**, dashed lines). This indicates a substantial loss in maximal ATPase inhibition with the H4 mutant. Notably, the double mutant exhibited an increased IC_{50} of 114 nM as well as a similarly elevated maximal inhibition value, indicating a more substantial loss of ATPase inhibition by UBXD1 when both the lariat and H4 are disrupted. Considering the minor IC_{50} effects observed for these mutants individually, these results indicate that lariat and H4 may contribute cooperatively to p97 ATPase control. However, disruption of these elements did not fully abrogate ATPase inhibition, thus additional UBXD1 interactions likely contribute.

Finally, cryo-EM analysis of p97 incubated with ADP and the UBXD1 lariat and H4 mutants was performed to understand structural changes associated with mutation of these motifs (**Figure 2.6A-D**, **Figure 2.S7F-J**, and **Table 2.1**). In both datasets, the predominant class contains only VIM UBXD1 density bound in all p97 NTDs, identical to p97:UBXD1^{VIM} in which the p97 hexamer is symmetric and unchanged from the p97^{ADP} state (**Figure 2.S7K,L**). Additional prevalent classes contain UBXD1 density corresponding to VIM-H4 for the lariat mutant (p97:UBXD1^{LX}) and the VIM, PUB, lariat and UBX for the H4 mutant (p97:UBXD1^{H4X}, essentially identical to p97:UBXD1^{closed}) (**Figure 2.6A** and **Figure 2.S7M,N**). Density for the mutated regions (lariat or H4) was not observed, indicating loss of these specific interactions was achieved for these variants. Notably, the open-ring state of p97 was not observed in any class, demonstrating that interactions by the lariat and H4 are likely necessary for complete separation of the P1-P6 interface. For p97:UBXD1^{LX} VIM density is better resolved on one protomer (denoted P1) compared to other sites, and following focused classification we identify that this protomer also

features H4 density interacting with the D2 domain, as identified in p97:UBXD1^{H4} (**Figure 2.6B**). The clockwise adjacent D2 exhibits strikingly weak density, reminiscent of the D2 flexibility we observed in the p97:UBXD1 closed and open states (**Figure 2.S7M**). This likely occurs because mutation of Lα3 results in loss of interactions by the UBX and lariat, thereby localizing UBXD1-induced conformational changes to the D2 ring of p97. To explore this state further, 3D variability analysis was performed, revealing a variability mode in which continuous flexibility is observed between two distinct states of the VIM-H4 and adjacent D2 domain. In one state, strong density for both the VIM and H4 is identified and is associated with a disordered D2 domain of the clockwise protomer (**Figure 2.6C** and **Movie 2.5**). Conversely, the second state exhibits a well-resolved clockwise D2 but weak to no density for the VIM-H4. This analysis indicates these states are in equilibrium and H4 binding correlates with destabilization of the adjacent D2. Thus, these structures further demonstrate that VIM-H4 binding destabilizes p97 through disruption of D2 interprotomer contacts and, together with our ATPase analysis, support a role for the VIM-H4 interaction in D2 hydrolysis control.

Considering both p97:UBXD1^{LX} and p97:UBXD1^{H4X} exhibit some P1-P6 asymmetry similar to p97:UBXD1^{closed}, we sought to characterize distances between these protomers to further define remodeling of the D1 and D2 by UBXD1. This was achieved by measuring distances between individual AAA+ domains based on centroids calculated from the fitted models (**Figure 2.S7O**). As expected, the symmetric p97^{ADP} state exhibits the shortest centroid distances (~35Å for D1 and D2) while p97:UBXD1^{closed} and p97:UBXD1^{open} structures show a partial (D1: ~37Å, D2: ~36 Å) and greatly expanded (D1: ~43Å, D2: ~46 Å) separation of the AAA+ domains, respectively (**Figure 2.6D**). As shown above (**Figure 2.2A**), in p97:UBXD1^{closed} the D1 domains are more separated than the D2, which we propose to be caused by lariat binding. Notably, mutation of the lariat (in p97:UBXD1^{LX}) decreases the D1-D1 distance relative to p97:UBXD1^{closed} while mutation of H4 (in p97:UBXD1^{H4X}) shows no changes in D1-D1, further supporting that the

D1 remodeling effects are driven by the lariat interaction. Intriguingly, the D2-D2 distance in p97:UBXD1^{LX} is substantially increased to ~40Å relative to p97:UBXD1^{closed} (at ~36Å). We postulate that this reflects a VIM-H4 interaction that is more pronounced when uncoupled from lariat binding to the D1 (as observed in **Figure 2.6C**), thus supporting that the VIM-H4 interactions indeed contribute to opening the p97 ring through D2 displacement. In sum, these results indicate the helical lariat and H4 independently regulate the D1 and D2 and function as critical p97 hexamer disrupting motifs that are necessary for full UBXD1 remodeling activity.

Discussion

Adapter proteins of the p97/VCP AAA+ hexamer serve critical roles in binding and regulating function in its many diverse and essential cellular pathways. How adapters may directly regulate p97 structure and mechanism has been an open question. Here we characterized the multi-domain adapter UBXD1 associated with lysosomal and mitochondrial autophagy, among other functions (12, 14, 17, 35, 36). We identify UBXD1 as a potent ATPase inhibitor and determined structures of full-length p97:UBXD1 that reveal how its interactions drive dramatic remodeling and ring-opening of the hexamer. These p97 conformational changes are coordinated by UBXD1 through a network of interprotomer interactions across the N-terminal, D1, and D2 domains. Based on these structures we propose a model describing how UBXD1 interactions coalesce to remodel p97 (**Figure 2.6E** and **Movie 2.6**).

We identify VIM binding to the NTD to be a primary contact given its established interaction (36, 39, 41, 42) and the prevalence of the p97:UBXD1^{VIM} state (**Figure 2.6E**, state II and **Figure 2.S1D**), which contains only the VIM helix bound to all protomers. We attribute no p97 structural changes to this interaction alone given this state is unchanged from p97^{ADP}. Conversely, interactions made by the helical lariat, including strong contacts by Lα3 along the D1 interprotomer interface, drive remodeling and separation of adjacent D1 domains (**Figure 2.6E**, state III). This is likely supported by UBX binding to the clockwise NTD, given its close connection to the lariat

and its conservation with ASPL. Through subclassification of the closed state we identify a class with the UBXD1 H4 helix, which is connected to the VIM by a short linker, bound at the D2 interface (**Figure 2.4F**). This interaction appears critical for separation of the D2 domains given conformational changes identified in this state that destabilize the interface, including displacement of helix α5' (**Figure 2.4G**). Moreover, variability analysis of the p97:UBXD1^{LX} structure, containing mutations in the lariat, reveals that H4 interactions are dynamic and displace the adjacent D2 (of protomer P6), further supporting a direct role in disrupting the D2 interface (**Figure 2.6C**). Thus, we propose that VIM-H4 specifically functions in p97 D2 remodeling while the combined interactions from the lariat and H4 together drive hexamer opening (**Figure 2.6E**, state V). Additionally, the connecting UBX and VIM domains tether these interactions to the respective NTDs, likely providing additional binding energy to leverage ring opening. Although more flexible, the PUB interaction with the C-terminus of the next clockwise protomer may further support D1-D2 remodeling and ring opening.

Notably, while other UBXD1-bound configurations are identified (**Figure 2.6D** and **Figure 2.S1I**), the open state is only observed with a singly-bound, wild-type UBXD1, thus indicating all UBXD1 contacts across three protomers are required for ring opening. Additional UBXD1 molecules may transiently bind p97, however, opening of the hexamer at one site would likely displace other molecules due to steric interactions and conformational changes across the ring. Given the continuity between the symmetric (p97^{ADP}), closed, and open conformations (**Movie 2.2**) and relation to the right-handed spiral adopted by the substrate-bound state (8, 9, 25), we propose that a single UBXD1 binds and remodels p97 in this manner to support its substrate processing and translocation cycle. Indeed, UBXD1 cooperates with YOD1 (a deubiquitinase) and PLAA (a ubiquitin-binding adapter) in lysophagy, further supporting its involvement in a substrate-related function (12). The spiral arrangement facilitated by UBXD1 might allow large substrates or those with complex topologies to enter the central channel for subsequent

processing; alternatively, UBXD1 could act as a release factor, allowing stalled substrates to diffuse out of the channel. Furthermore, UBXD1 activity in several pathways appears independent of the ubiquitin-binding adapter UFD1/NPL4 (12, 14). This observation, coupled with the unique structural remodeling facilitated by UBXD1, suggests that this adapter enables a function distinct from canonical substrate engagement and processing.

UBXD1's potent inhibition of p97 ATPase activity is striking and indicates a distinct role for adapters in regulating hydrolysis by p97. Inhibition may result from disruption of D1 and D2 inter-protomer contacts, given the nucleotide pocket resides at the interface and the arginine finger and other intersubunit signaling contacts from the adjacent protomer are lost (**Figure 2.2D,E**) (25). Indeed, we identify D1 and D2 displacements of 8 and 11 Å, respectively, at the disrupted P6-P1 interface of the open state (**Figure 2.2D**). Additionally, occupancy by the helical lariat of the binding site of UPCDC30245, an allosteric inhibitor that prevents cycling between ADP- and ATP-bound states (19), indicates that this motif may contribute to ATPase inhibition through an additional mechanism. However, given that the ATPase inhibition activity of the UBXD1 LX mutant is modestly impaired, full inhibition must result through other UBXD1 interactions (**Figure 2.5E** and **Figure 2.6D**). Interaction and remodeling of the D2 small subdomain by UBXD1 H4 is also a likely contributor to hydrolysis control and we identify mutation of this helix reduces the maximal inhibition by UBXD1. Hydrolysis inhibition through the D2 is consistent with previous observations that the D2 domain is responsible for the majority of p97 ATPase activity (55). While we consider the helical lariat and H4 to be primary drivers of ring separation and thus ATPase inhibition, the effects of these remodeling elements are likely buttressed by other UBXD1 domains, given that mutation of the lariat or H4 does not completely ablate UBXD1's inhibitory activity (**Figure 2.5E**). Therefore, the potent inhibitory effect of UBXD1 may be driven by avidity, without a single interaction domain being specifically responsible for hydrolysis control. Supporting this, many UBXD1 interactions are weak or weakened compared

to homologous domains in other adapters. Specifically, H1/H2, though highly conserved (**Figure 2.S8**), weakly interacts by NMR (36–38, 56), its VIM is lacking an Arg residue present in many other adapters (41, 42), its UBX has residues in the S3/S4 loop mutated and does not bind the NTD in isolation (17, 39, 43), and H4 also weakly binds as measured by NMR (36). Notably, UBXD1-mediated inhibition of ATPase activity does not necessitate an overall inhibitory role of this adapter; UBXD1 could potentially stabilize a stalled, ATPase-inhibited state until association of a substrate, at which point hydrolysis-dependent substrate processing might occur.

We propose UBXD1, ASPL, and SVIP are structurally related adapters with conserved motifs that mediate distinct effects on p97 activity. In addition to being potent inhibitors of p97 ATPase activity, these adapters appear to not bind substrate or possess enzymatic activity, suggesting their primary activity is modulation of p97 structure rather than direct involvement in substrate engagement. In contrast to many other AAA+ proteins, p97 requires an extensive set of adapter proteins, including those that deliver substrates, to facilitate its functions. This is likely due to the relative stability of the p97 hexamer, which adopts a stable, planar conformation in the absence of substrate and even nucleotide (18, 57). It is therefore reasonable to conclude that p97 relies on a set of adapters to structurally remodel the hexamer for various purposes, in the same manner as its dependence on adapters directly involved in substrate processing. We identify the helical lariat and H4-like sequences to be critical control elements in these adapters. The different degrees of remodeling of lariat-containing adapters (complete hexamer disassembly with ASPL compared to intact hexamers with UBXD1) likely reflect the different assembles of p97-interacting domains in these two adapters. In addition to the lariat-UBX module, ASPL has a UBXL domain and a SHP box that both bind the NTD, while UBXD1 features a much larger complement of domains that flank the lariat on both sides. These extra domains could potentially ‘hold’ the hexamer together during binding, preventing complete dissociation, possibly to facilitate an as-yet unknown step of substrate processing. Indeed, a recent study revealed that ASPL-mediated

hexamer disassembly enables binding and modification by the methyltransferase VCPKMT, suggesting that disruptions of hexamer architecture are biologically relevant (58). Likewise, the extra p97-interacting domains of UBXD1 compared to SVIP indicate a more sophisticated function than merely ATPase inhibition, as SVIP similarly inhibits hydrolysis with only VIM and H4-like sequences. In sum, the characterization of adapters as structural modulators of p97 reported here and the large number of still-uncharacterized p97-interacting proteins suggest that there are more classes of adapters with distinct effects on p97 activity yet to be discovered, likely with novel regulatory effects on unfoldase function.

Figures

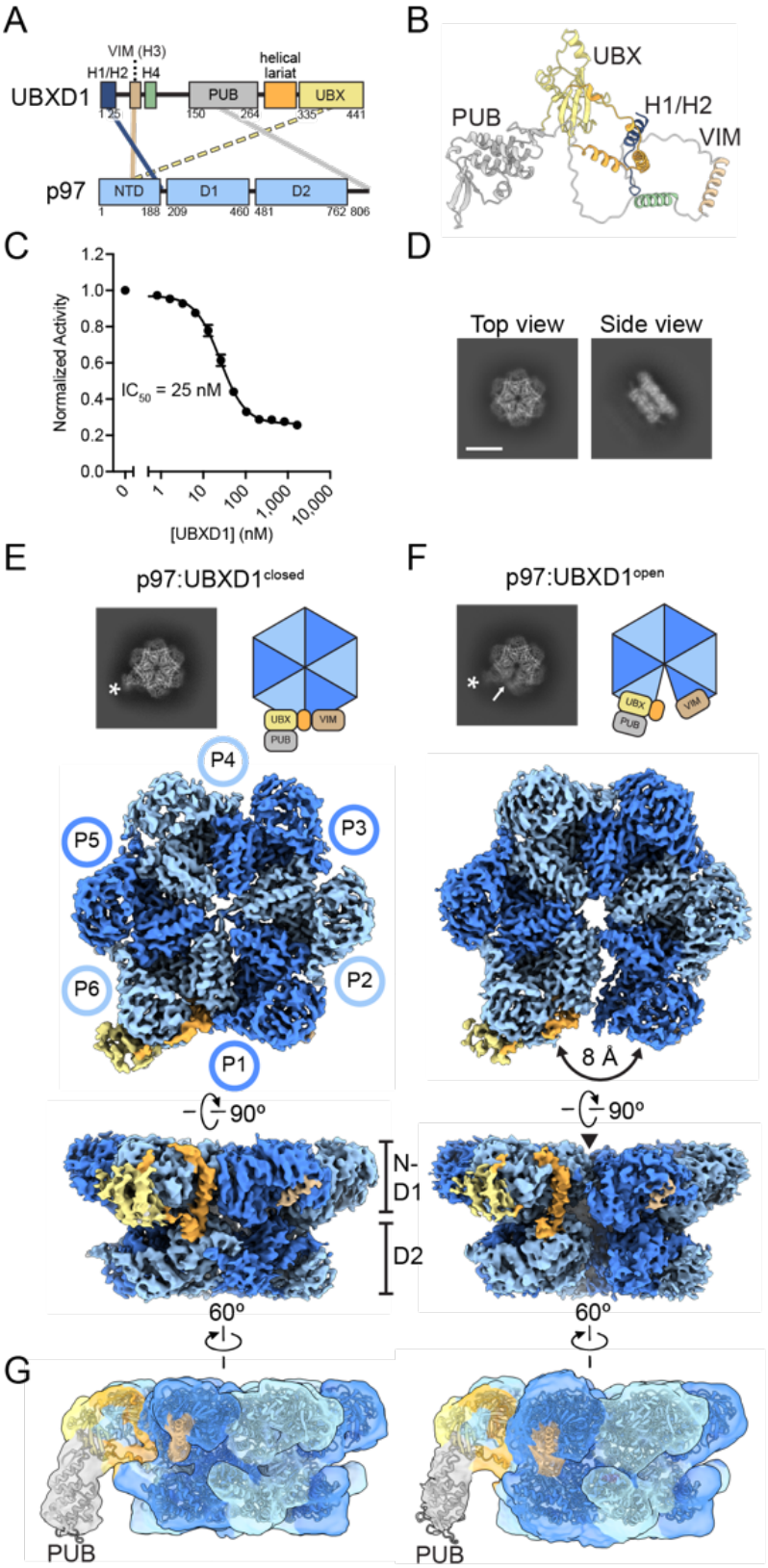
A
VIM (H3)
H1/H2
H4
helical lariat
UBXD1
PUB
UBX
1
25
150
264
335
441
p97
NTD
D1
D2
1
188
209
460
481
762
806
B
UBX
PUB
H1/H2
VIM
C
Normalized Activity
IC50 = 25 nM
[UBXD1] (nM)
D
Top view
Side view
E
p97:UBXD1closed
UBX
VIM
PUB
P4
P5
P3
P6
P2
P1
90°
N-D1
D2
60°
F
p97:UBXD1open
8 Å
90°
60°
G
PUB
PUB

Figure 2.1 Cryo-EM structures of p97:UBXD1 closed and open states
(**A**) Domain schematics of UBXD1 and p97 (not to scale) showing reported interactions (solid lines) between conserved domains (36, 39–41) and the canonical UBX-NTD interaction previously reported to not occur for UBXD1 (dashed line) (17, 39, 43). (**B**) AlphaFold model of UBXD1 showing structured regions (H1/H2, VIM, H4, PUB, helical lariat, and UBX) colored as in (A). (**C**) Steady-state ATPase activity (Y-axis, normalized to activity at 0 nM UBXD1) of p97 at increasing concentrations of UBXD1 (X-axis), resulting in a calculated IC_{50} of 25 nM. Error bars represent standard deviation and data are from three independently performed experiments. (**D**) Representative 2D class averages following initial classification of the full p97:UBXD1/ADP dataset, showing p97 hexamer and no additional density for UBXD1 (scale bar equals 100 Å). Final cryo-EM reconstructions of (**E**) p97:UBXD1^{closed} and (**F**) p97:UBXD1^{open} states with top-view 2D projections showing UBX/PUB density (*) and open p97 ring (arrow) compared to cartoon depiction of p97:UBXD1 complexes (top row); (below) cryo-EM density maps (p97:UBXD1^{open} is a composite map, see methods), colored to show the p97 hexamer (light and dark blue, with protomers labeled P1-P6) and UBXD1 density for the VIM (brown), UBX (yellow) and lariat (orange) domains. The 8 Å separation between protomers P1 and P6 is indicated for p97:UBXD1^{open}. (**G**) Low-pass filtered maps and fitted models of p97:UBXD1^{closed} (left) and p97:UBXD1^{open} (right) exhibiting low-resolution density for the PUB domain (gray).

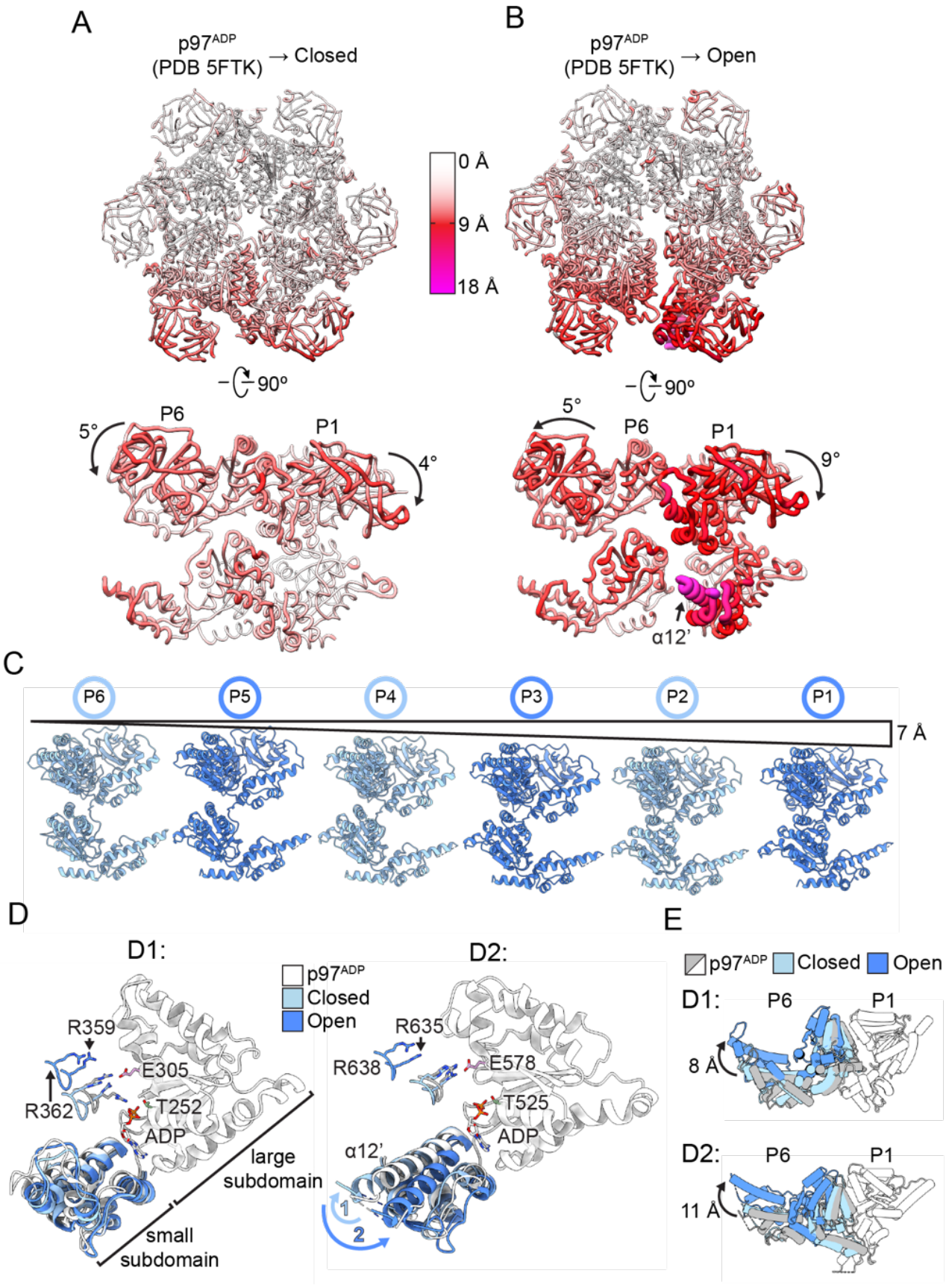
A
p97ADP
(PDB 5FTK) → Closed
0 Å
9 Å
18 Å
90°
P6
P1
5°
4°
B
p97ADP
(PDB 5FTK) → Open
90°
5°
P6
P1
9°
α12'
C
P6
P5
P4
P3
P2
P1
7 Å
D
D1:
D2:
p97ADP
Closed
Open
R359
E305
R362
T252
ADP
large
subdomain
small
subdomain
R635
R638
E578
T525
ADP
α12'
1
2
E
p97ADP
Closed
Open
D1:
P6
P1
8 Å
D2:
P6
P1
11 Å

Figure 2.2 UBXD1-mediated p97 hexamer remodeling
The p97 hexamer and rotated side view of the seam protomers P1 and P6 for (**A**) p97:UBXD1^{closed} and (**B**) p97:UBXD1^{open} structures, colored according to Cα RMSD values relative to the p97^{ADP} symmetric state (PDB 5FTK, aligned to P3 and P4). The largest changes (>15 Å, magenta with wider tubes) are identified for P1 α12' (arrow) in the open state, intermediate changes (~10 Å, red) for P1 and P6 with rotations of the NTDs relative to p97^{ADP} shown, and small/no changes for the remaining regions (<5 Å, white). (**C**) Side-by-side view of individual protomers aligned based on position in the p97:UBXD1^{open} hexamer, showing vertical displacement along the pseudo-C6 symmetry axis. (**D**) Overlay of the D1 (left) and D2 (right) AAA+ domains of P1 for p97^{ADP}, p97:UBXD1^{closed}, and p97:UBXD1^{open}, aligned to the large subdomains and colored as indicated. ADP is shown with conserved Walker A/B and trans-acting (P6) Arg finger residues indicated. The large rotation of the D2 small subdomain, exemplified by α12', is shown (relative to p97^{ADP}) for the closed (label 1) and open (label 2) states. (**E**) Top view overlay of the D1 (upper) and D2 (lower) domains for the P6-P1 pair in the three states and aligned to P1 to show relative rotations of P6, colored as indicated. Rotations shown are from the p97^{ADP} to the p97:UBXD1^{open} state and determined from centroid positions of the D1 and D2 domains.

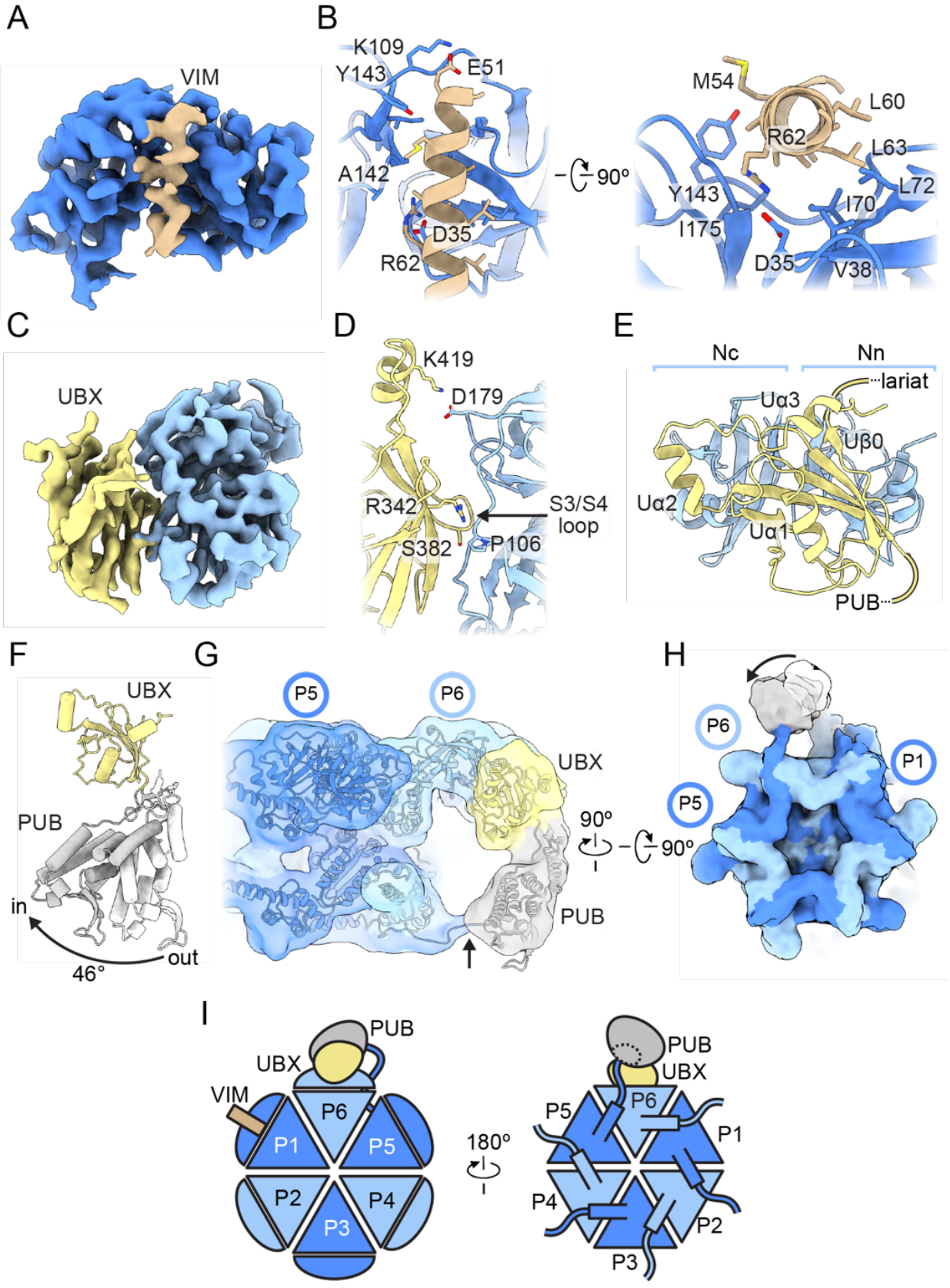
A
VIM
B
K109
Y143
E51
A142
D35
R62
90°
M54
L60
R62
L63
L72
Y143
I70
I175
D35
V38
C
UBX
D
K419
D179
R342
S3/S4
loop
S382
P106
E
Nc
Nn
lariat
Uα3
Uβ0
Uα2
Uα1
PUB
F
UBX
PUB
in
out
46°
G
P5
P6
UBX
90°
90°
PUB
H
P6
P1
P5
I
PUB
UBX
VIM
P6
P1
P5
P2
P4
P3
180°
PUB
UBX
P5
P6
P1
P4
P2
P3

Figure 2.3 Interactions by conserved VIM, UBX, and PUB domains of UBXD1 across the p97 hexamer

(**A**) Sharpened map of P1 NTD (dark blue) and the VIM helix (brown) from the p97:UBXD1^{closed} structure. (**B**) Model showing VIM helix interactions with the NTD, colored as in (A) with labeled interacting residues. (**C**) Sharpened map of the P6 NTD (light blue) and UBX domain (yellow). The model of the UBX and NTD in p97:UBXD1^{closed} is shown (**D**) depicting UBX-NTD contacts, including the conserved S3/S4 loop contact (59) (arrow) and (**E**) with non-canonical structural elements Uα2, Uα3, and Uβ0, colored as in (C). (**F**) Overlay of PUB from p97:UBXD1-PUB$_{in}$ (gray) and p97:UBXD1-PUB$_{out}$ (white) (see methods), aligned to the UBX (yellow) domain, showing 46° rotation of the PUB domain position. (**G**) Low-pass filtered map and model of p97:UBXD1-PUB$_{in}$ depicting PUB domain contact with p97 and model for C-terminal HbYX tail interaction from the adjacent P5 protomer (arrow) and (h) bottom view of the hexamer map with out (white) and in (gray) positions of the PUB. (**I**) Cartoon of p97:UBXD1^{closed} depicting UBXD1 interactions across three p97 protomers (P1:VIM, P6:UBX, and P5:PUB) through canonical p97-interacting domains.

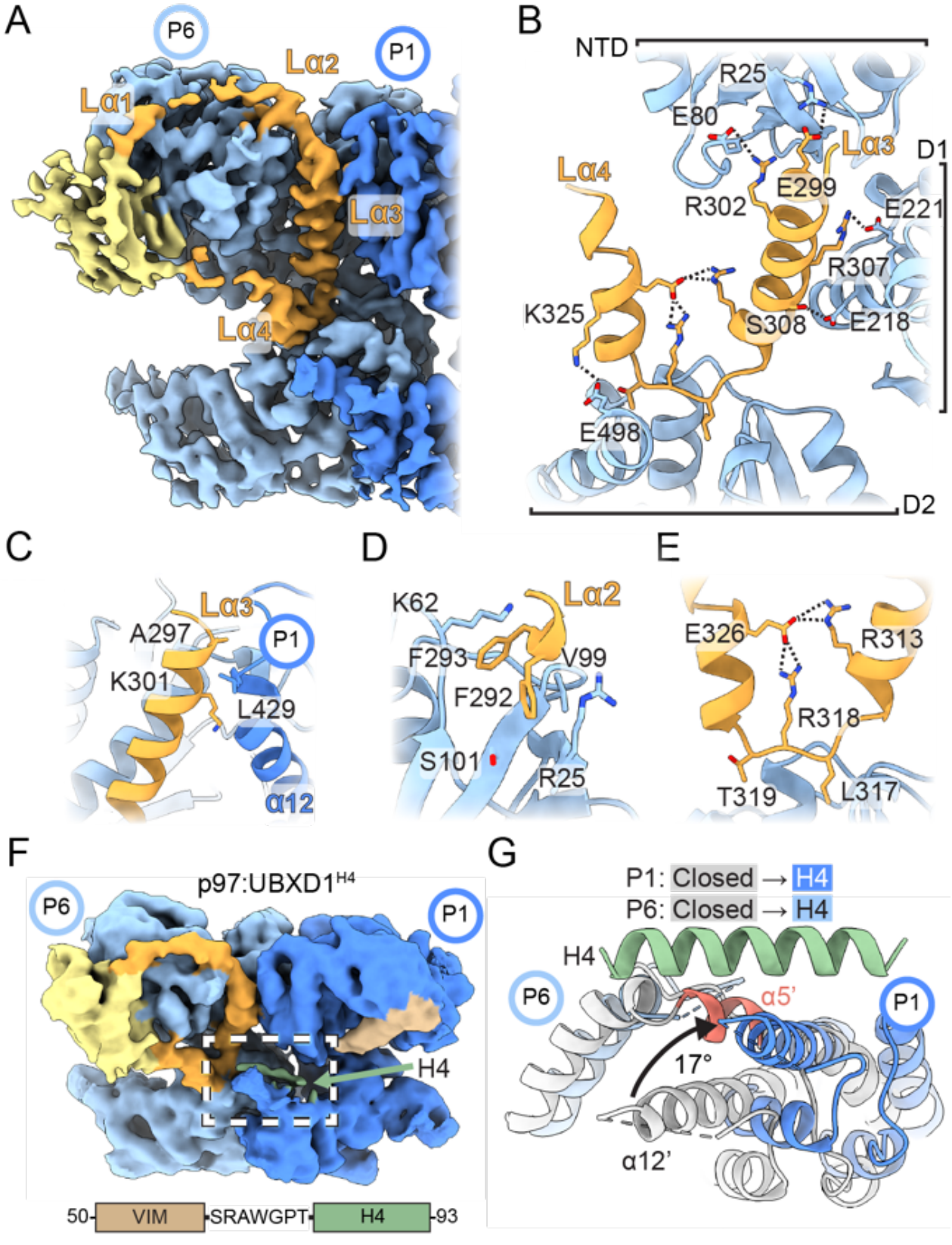
A
P6
P1
Lα2
Lα1
Lα3
Lα4
B
NTD
R25
E80
Lα3
D1
Lα4
E299
R302
E221
R307
K325
S308
E218
E498
D2
C
Lα3
A297
P1
K301
L429
α12
D
K62
Lα2
F293
V99
F292
S101
R25
E
E326
R313
R318
T319
L317
F
p97:UBXD1H4
P6
P1
H4
50
VIM
SRAWGPT
H4
93
G
P1: Closed → H4
P6: Closed → H4
H4
P6
α5'
P1
17°
α12'

Figure 2.4 p97 remodeling interactions by the UBXD1 helical lariat and VIM-H4
(**A**) Closed state map (from p97:UBXD1^{meta}) showing density for the UBXD1 helical lariat (orange) and UBX (yellow) encircling the P6 NTD with Lα2, Lα3, and Lα4 interacting along the P6-P1 interprotomer interface. (**B**) Expanded view showing Lα3 and Lα4 (orange) contacts with P6 across the NTD, D1, and D2, including putative electrostatic interactions (dashed lines). (**C**) View of the P6-P1 interface showing key contacts by Lα3 with the D1 α12 helix of protomer P1. View of (**D**) Lα2 interactions involving hydrophobic packing into the NTD and (**E**) Lα3 and Lα4 intra-lariat contacts and contacts with D2, stabilizing the helical lariat. (**F**) Unsharpened map of p97:UBXD1^{H4}, showing density for H4 (green) adjacent to the VIM (brown) and along the P6-P1 interface. Shown below is an expanded view of the VIM-H4 sequence, featuring only a short 7-amino acid linker connecting the two helices. (**G**) Modeled view (see **Figure 2.S6C**) of helix H4 interacting across the D2 domains at the P1-P6 interface with p97 from p97:UBXD1^{H4} (P1: dark blue, P6: light blue), and p97:UBXD1^{closed} (gray) overlaid (by alignment of the P1 D2 large subdomain) to show conformational changes at the P6-P1 interface including displacement of P6 helix α5' (red) and large rotation of P1 α12' in p97:UBXD1^{H4}.

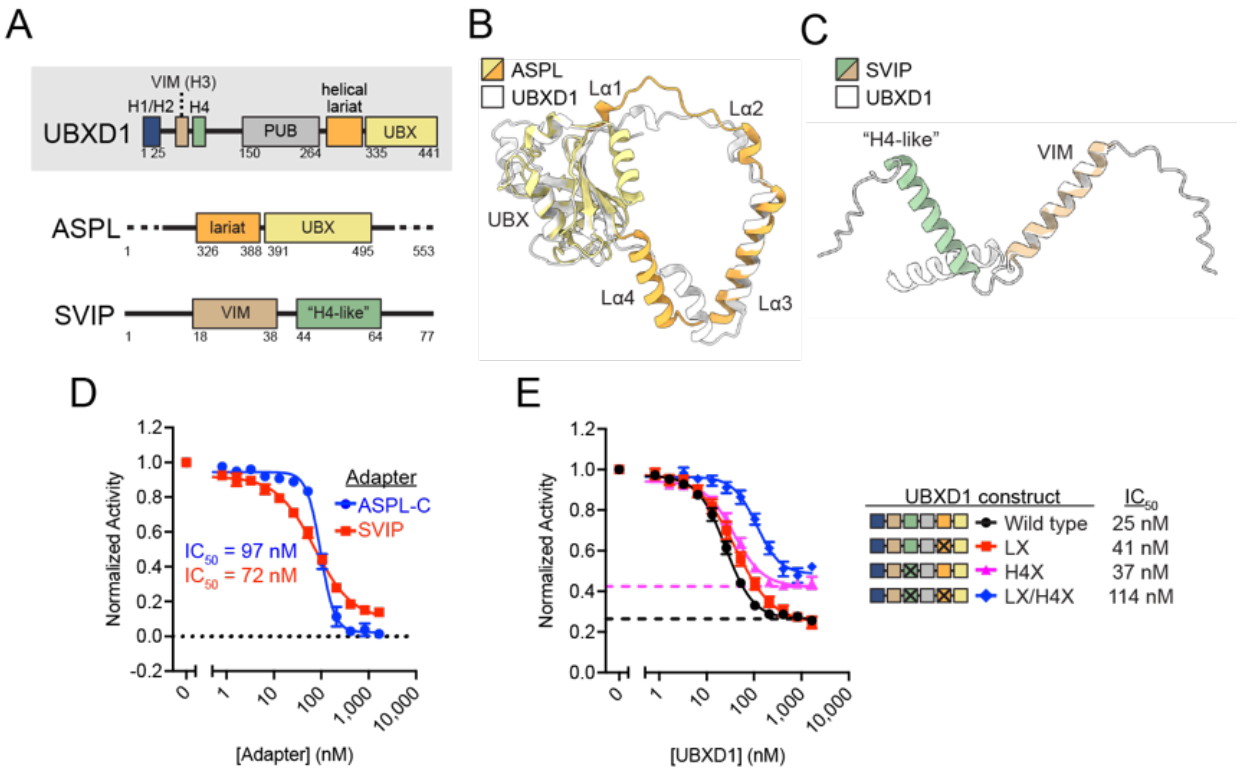

Figure 2.5 Analysis of the helical lariat and VIM-H4 as conserved p97-remodeling motifs
(**A**) Domain schematics of UBXD1, ASPL, and SVIP (not to scale). Overlay of the (**B**) UBX-helical lariat of ASPL (residues 318-495 from PDB 5IFS, colored as in (A)) and UBXD1 (residues 270-441 from the p97:UBXD1^{closed} model, in white) and the (**C**) VIM-"H4-like" region of SVIP (AlphaFold model, colored as in (A)) and UBXD1 (residues 50-93 from the AlphaFold model, in white). (**D**) Steady-state ATPase activity of p97 as a function of ASPL-C or SVIP concentration. Error bars represent standard deviation and data are from three independently performed experiments. Calculated IC_{50}s are shown below. (**E**) Steady-state ATPase activity of p97 as a function of UBXD1 protein concentration for WT, LX (lariat mutant: E299R/R302E/R307E/E312R), or H4X (helix H4 sequence scramble); maximum concentration tested was 1.67 μM. Dashed lines represent the minimal activity (or maximal UBXD1 inhibition) obtained from the corresponding curve fit. Error bars represent standard deviation and data are from three independently performed experiments. Calculated IC_{50}s and schematics of UBXD1 constructs used are shown at right.

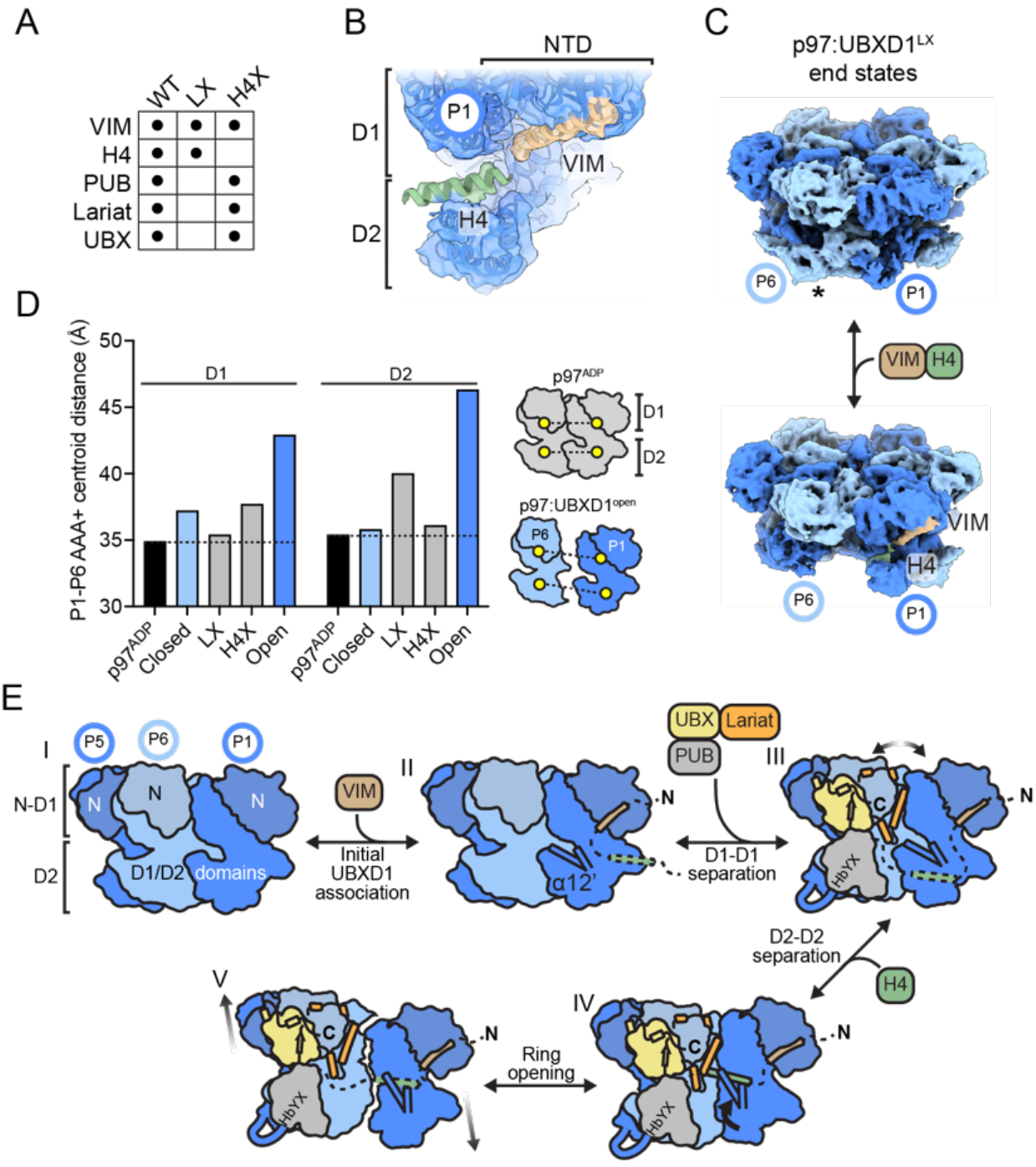
A
WT
LX
H4X
VIM
H4
PUB
Lariat
UBX
B
NTD
D1
D2
P1
VIM
H4
C
p97:UBXD1LX
end states
P6
*
P1
VIM
H4
P6
P1
D
P1-P6 AAA+ centroid distance (Å)
50
45
40
35
30
D1
D2
p97ADP
Closed
LX
H4X
Open
p97ADP
Closed
LX
H4X
Open
p97ADP
D1
D2
p97:UBXD1open
P6
P1
E
I
P5
P6
P1
N-D1
D2
N
N
N
D1/D2 domains
VIM
Initial UBXD1 association
II
N
α12'
UBX
Lariat
PUB
III
D1-D1 separation
C
N
HbYX
D2-D2 separation
H4
V
C
N
HbYX
Ring opening
IV
C
N
HbYX

Figure 2.6 Structural analysis of p97:UBXD1 mutant complexes and model for p97 hexamer remodeling through UBXD1 domain interactions

(**A**) Table of ADP-bound p97:UBXD1 cryo-EM datasets (WT, lariat mutant (LX), and H4 mutant (H4X)) and corresponding UBXD1 domains observed as densities in the reconstructions. (**B**) Unsharpened map and fitted model of the VIM-H4-bound P1 protomer from p97:UBXD1^{LX} (**Figure 2.S7F**), colored as in **Figure 2.1**. (**C**) First and last frames of the 3D variability analysis output for p97:UBXD1^{LX} showing P6 D2 density (*) but no VIM-H4 in one end state (top) and no P6 D2 in the other when VIM-H4 density is present (bottom). (**D**) P1-P6 interprotomer distances (based on centroid positions) for the D1 and D2 domains of p97^{ADP} (PDB 5FTK), p97:UBXD1^{closed}, p97:UBXD1^{LX}, p97:UBXD1^{H4X}, and p97:UBXD1^{open}. Dashed lines represent the minimal distances observed in p97^{ADP}. A schematic representing distances calculated is shown (right). (**E**) Model of p97:UBXD1 interactions and structural remodeling of the hexamer. State I: side view of p97^{ADP} (PDB 5FTK), colored as in Figure 2.1. NTDs are shaded for clarity. State II: p97:UBXD1^{VIM}, in which the VIM initially associates with the NTD of P1. The position of the D2 small subdomain is illustrated by α12' and an adjacent helix. State III: the p97:UBXD1^{closed} state, in which the UBX, PUB, and helical lariat contact P5 and P6, resulting in the disruption of D1-D1 contacts at the P1-P6 interface. State IV: the p97:UBXD1^{H4} state, in which H4 is positioned on top of the D2 domain of P1, causing it to rotate upward, and displacing a helix from the D2 domain of P6. State V: the p97:UBXD1^{open} state, in which P6 and P1 have completely separated, and all protomers are arranged into a shallow right-handed helix.

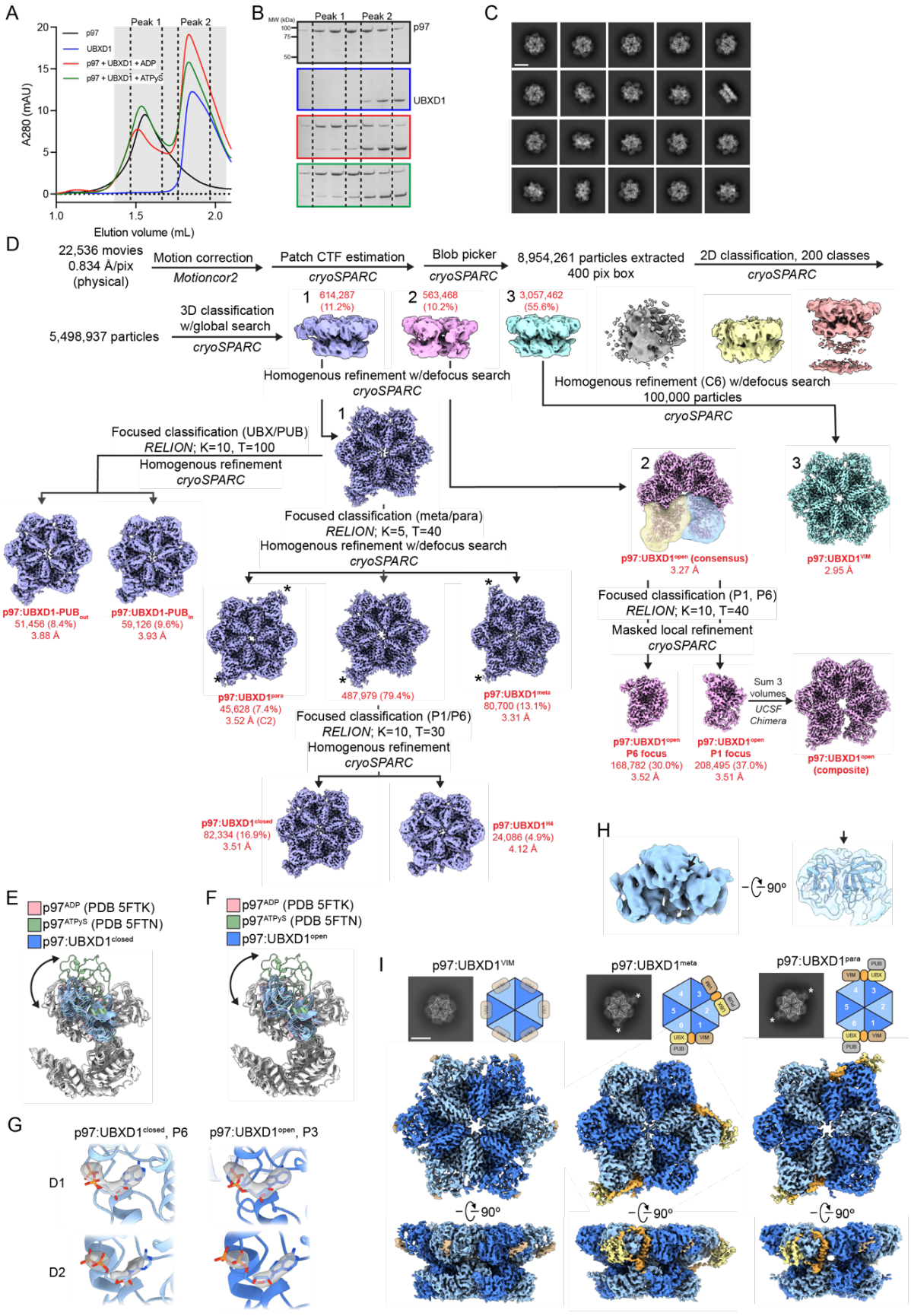
A
Peak 1
Peak 2
p97
UBXD1
p97 + UBXD1 + ADP
p97 + UBXD1 + ATPγS
A280 (mAU)
Elution volume (mL)
B
MW (kDa)
Peak 1
Peak 2
p97
UBXD1
C
D
22,536 movies
0.834 Å/pix
(physical)
Motion correction
Motioncor2
Patch CTF estimation
cryoSPARC
Blob picker
cryoSPARC
8,954,261 particles extracted
400 pix box
2D classification, 200 classes
cryoSPARC
5,498,937 particles
3D classification
w/global search
cryoSPARC
1 614,287 (11.2%)
2 563,468 (10.2%)
3 3,057,462 (55.6%)
Homogenous refinement w/defocus search
cryoSPARC
Homogenous refinement (C6) w/defocus search
100,000 particles
cryoSPARC
Focused classification (UBX/PUB)
RELION; K=10, T=100
Homogenous refinement
cryoSPARC
p97:UBXD1-PUBout
51,456 (8.4%)
3.88 Å
p97:UBXD1-PUBin
59,126 (9.6%)
3.93 Å
Focused classification (meta/para)
RELION; K=5, T=40
Homogenous refinement w/defocus search
cryoSPARC
p97:UBXD1para
45,628 (7.4%)
3.52 Å (C2)
487,979 (79.4%)
p97:UBXD1meta
80,700 (13.1%)
3.31 Å
Focused classification (P1/P6)
RELION; K=10, T=30
Homogenous refinement
cryoSPARC
p97:UBXD1closed
82,334 (16.9%)
3.51 Å
p97:UBXD1H4
24,086 (4.9%)
4.12 Å
p97:UBXD1open (consensus)
3.27 Å
p97:UBXD1VIM
2.95 Å
Focused classification (P1, P6)
RELION; K=10, T=40
Masked local refinement
cryoSPARC
p97:UBXD1open
P6 focus
168,782 (30.0%)
3.52 Å
p97:UBXD1open
P1 focus
208,495 (37.0%)
3.51 Å
Sum 3 volumes
UCSF Chimera
p97:UBXD1open
(composite)
E
p97ADP (PDB 5FTK)
p97ATPγS (PDB 5FTN)
p97:UBXD1closed
F
p97ADP (PDB 5FTK)
p97ATPγS (PDB 5FTN)
p97:UBXD1open
G
p97:UBXD1closed, P6
p97:UBXD1open, P3
D1
D2
H
90°
I
p97:UBXD1VIM
p97:UBXD1meta
p97:UBXD1para
90°
90°
90°

Figure 2.S1 Biochemical and cryo-EM analysis of the p97:UBXD1 interaction
(**A**) SEC traces of p97:UBXD1 complexes, showing a left shift in peak elution volume for p97 samples with UBXD1. Fractions in the shaded range were analyzed by SDS-PAGE. No p97 monomer peak was observed with UBXD1 incubation. (**B**) Coomassie Brilliant Blue-stained SDS-PAGE gels of fractions from SEC runs in (A). (**C**) Representative 2D class averages of the p97/UBXD1^{WT}/ADP dataset (scale bar equals 100 Å). No p97 monomers were identified during 2D classification. (**D**) Processing workflow for structures obtained from the p97/UBXD1^{WT}/ADP dataset. Masks used for the P1 and P6 focused classification and masked local refinement of p97:UBXD1^{open} are shown in transparent blue and yellow, respectively. (**E**) Overlay of all protomers from p97:UBXD1^{closed} (blue) with a protomer in the ADP-bound, down NTD conformation (pink, PDB 5FTK) and a protomer in the ATPγS-bound, up NTD conformation (green, PDB 5FTN), aligned by the D1 large subdomain (residues 211-368). For all protomers, the NTDs are colored, and the D1 and D2 domains are white. (**F**) As in (E), but depicting protomers from p97:UBXD1^{open} (blue). (**G**) Nucleotide densities for representative D1 and D2 pockets in p97:UBXD1^{closed} and p97:UBXD1^{open}. (**H**) Representative additional density in NTD corresponding to a VIM helix (unsharpened map of P4 in p97:UBXD1^{open}). (**I**) Cartoons, top view projections of sharpened maps showing UBX/PUB density (*), and sharpened maps of p97:UBXD1^{VIM}, p97:UBXD1^{meta}, and p97:UBXD1^{para} (scale bar equals 100 Å). In p97:UBXD1^{VIM}, the VIM density is depicted as a difference map of p97:UBXD1^{VIM} and a map generated from a model without VIM helices.

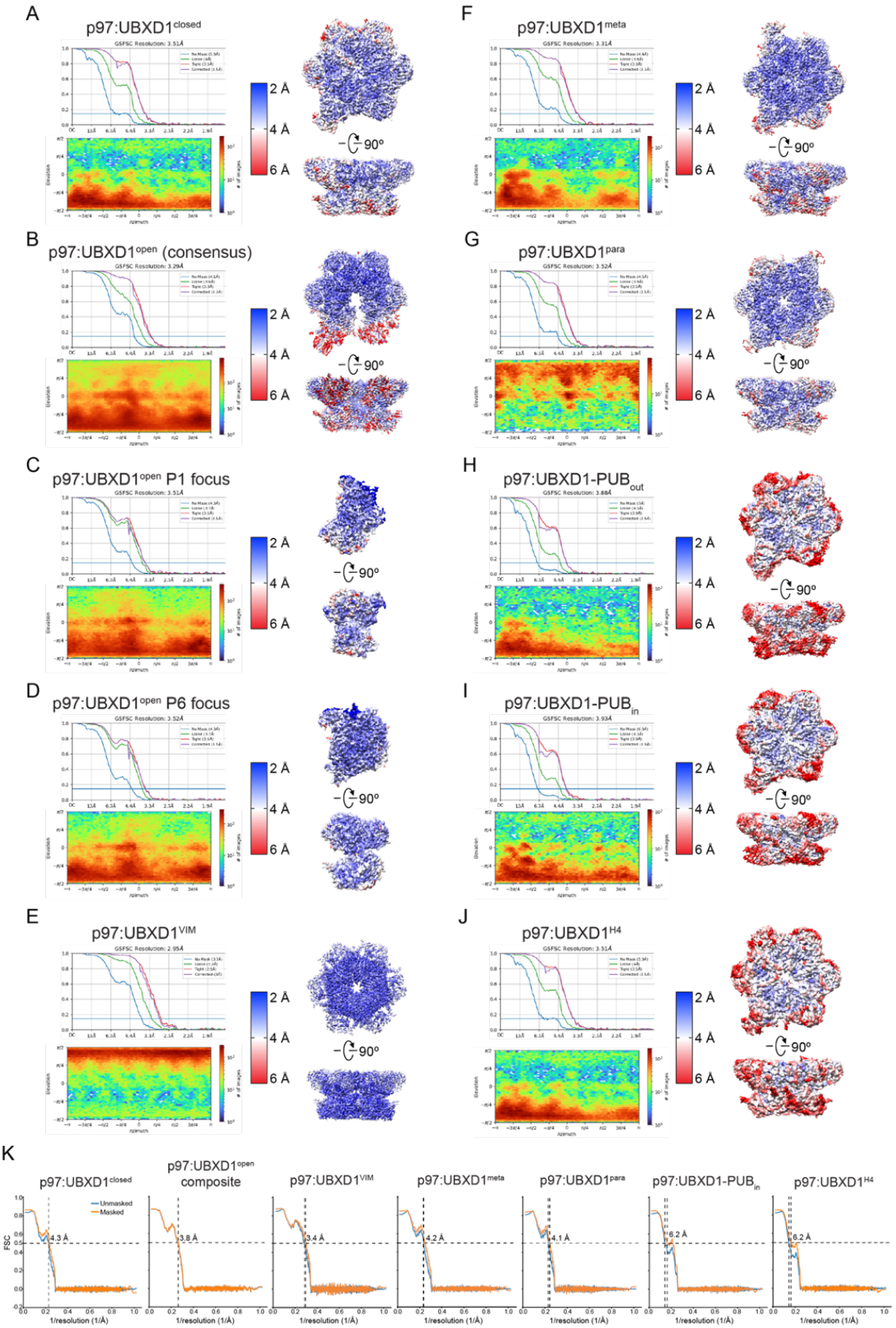
A
p97:UBXD1closed
GSFSC Resolution: 3.31Å
2 Å
4 Å
6 Å
90°
B
p97:UBXD1open (consensus)
GSFSC Resolution: 3.29Å
C
p97:UBXD1open P1 focus
GSFSC Resolution: 3.51Å
D
p97:UBXD1open P6 focus
GSFSC Resolution: 3.52Å
E
p97:UBXD1VIM
GSFSC Resolution: 2.95Å
F
p97:UBXD1meta
GSFSC Resolution: 3.31Å
G
p97:UBXD1para
GSFSC Resolution: 3.52Å
H
p97:UBXD1-PUBout
GSFSC Resolution: 3.88Å
I
p97:UBXD1-PUBin
GSFSC Resolution: 3.93Å
J
p97:UBXD1H4
GSFSC Resolution: 3.31Å
K
p97:UBXD1closed
p97:UBXD1open composite
p97:UBXD1VIM
p97:UBXD1meta
p97:UBXD1para
p97:UBXD1-PUBin
p97:UBXD1H4
Unmasked
Masked
FSC
4.3 Å
3.8 Å
3.4 Å
4.2 Å
4.1 Å
6.2 Å
6.2 Å
1/resolution (1/Å)

Figure 2.S2 Cryo-EM densities and resolution estimation from the ADP-bound p97:UBXD1^{WT} dataset

Fourier shell correlation (FSC) curves, particle orientation distribution plots, and sharpened density maps colored by local resolution (0.143 cutoff) for (**A**) p97:UBXD1^{closed}, (**B**) p97:UBXD1^{open} (consensus map), (**C**) p97:UBXD1^{open} P1 focus, (**D**) p97:UBXD1^{open} P6 focus, (**E**) p97:UBXD1^{VIM}, (**F**) p97:UBXD1^{meta}, (**G**) p97:UBXD1^{para}, (**H**) p97:UBXD1-PUB$_{out}$, (**I**) p97:UBXD1-PUB$_{in}$, and (**J**) p97:UBXD1^{H4}. (**K**) Map-model FSC curves for p97:UBXD1^{closed}, p97:UBXD1^{open} (composite map), p97:UBXD1^{VIM}, p97:UBXD1^{meta}, p97:UBXD1^{para}, p97:UBXD1-PUB$_{in}$, and p97:UBXD1^{H4}. Displayed model resolutions were determined using the masked maps.

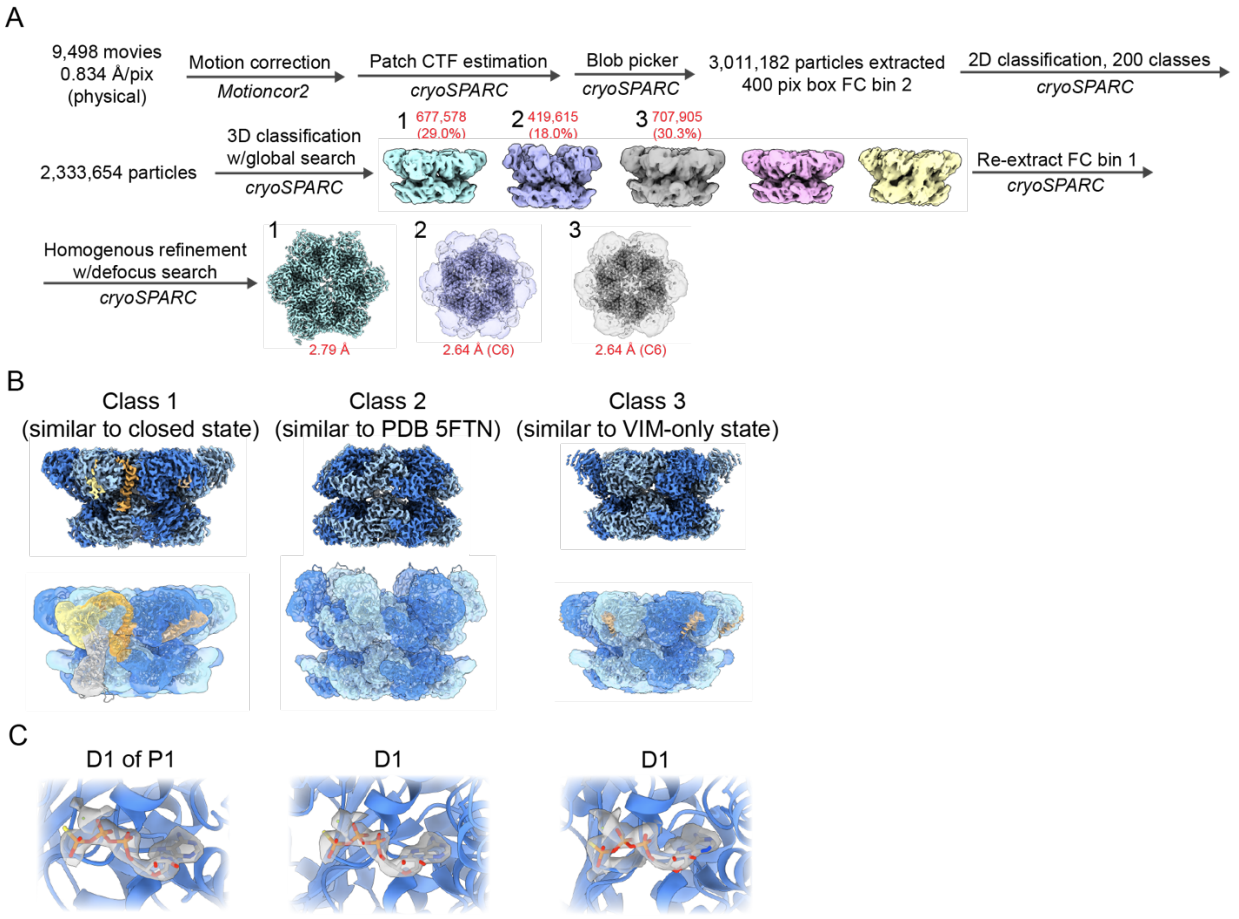

Figure 2.S3 Cryo-EM analysis of p97:UBXD1 incubated with ATPγS
(**A**) Processing workflow for structures obtained from the p97/UBXD1^{WT}/ATPγS dataset. (**B**) (Top row) sharpened maps of class 1-3 refinements. (Bottom row) p97:UBXD1^{closed} model overlaid with filtered map, unsharpened map, ATPγS-bound p97 hexamer with NTDs in the up state (PDB 5FTN) overlaid with the class 2 unsharpened map, and p97:UBXD1^{VIM} model overlaid with the class 3 unsharpened map, respectively. All maps are colored as in **Figure 2.1**. (**C**) Representative nucleotide densities for class 1-3 refinements (sharpened maps), showing clear γ-phosphate and Mg^{2+} density. The nucleotide and binding pocket from PDB 5FTN are shown for clarity.

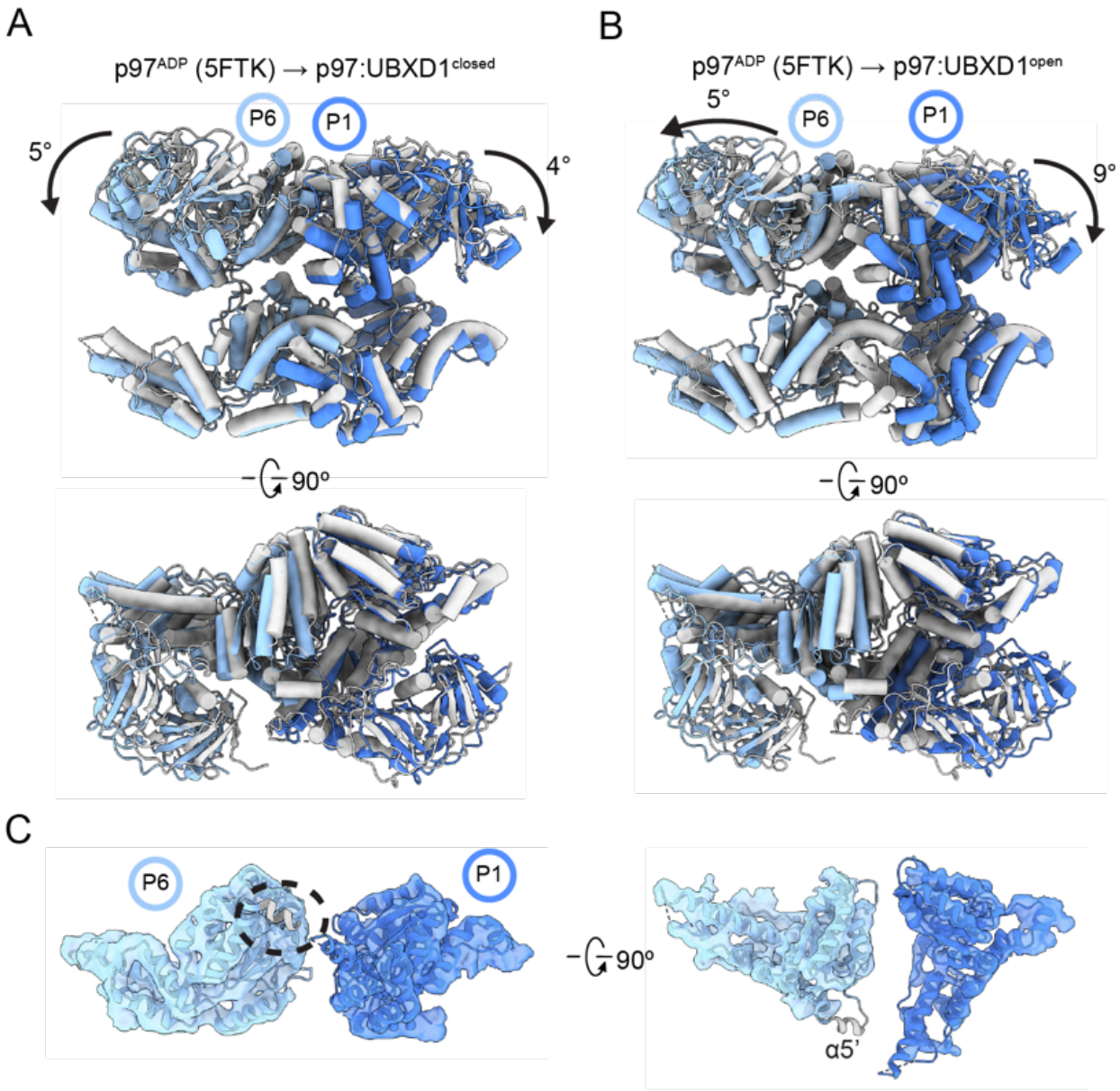

Figure 2.S4 Changes in p97:UBXD1^{closed} and p97:UBXD1^{open}
(**A**) Overlay of protomers P1 (dark blue) and P6 (light blue) from p97:UBXD1^{closed}, aligned to protomers P3 and P4 from PDB 5FTK. P1 and P6 protomers from 5FTK are shown in gray. (**B**) As in (A), but depicting p97:UBXD1^{open} protomers. (**C**) Unsharpened map of the D2 domains of protomers P1 and P6 of p97:UBXD1^{open}, overlaid with the D2 domain from p97^{ADP} on P6, showing lack of density for helix α5' (gray, encircled) normally contacting the counterclockwise D2 domain. The D2 domain of P1 of the open state is shown for clarity.

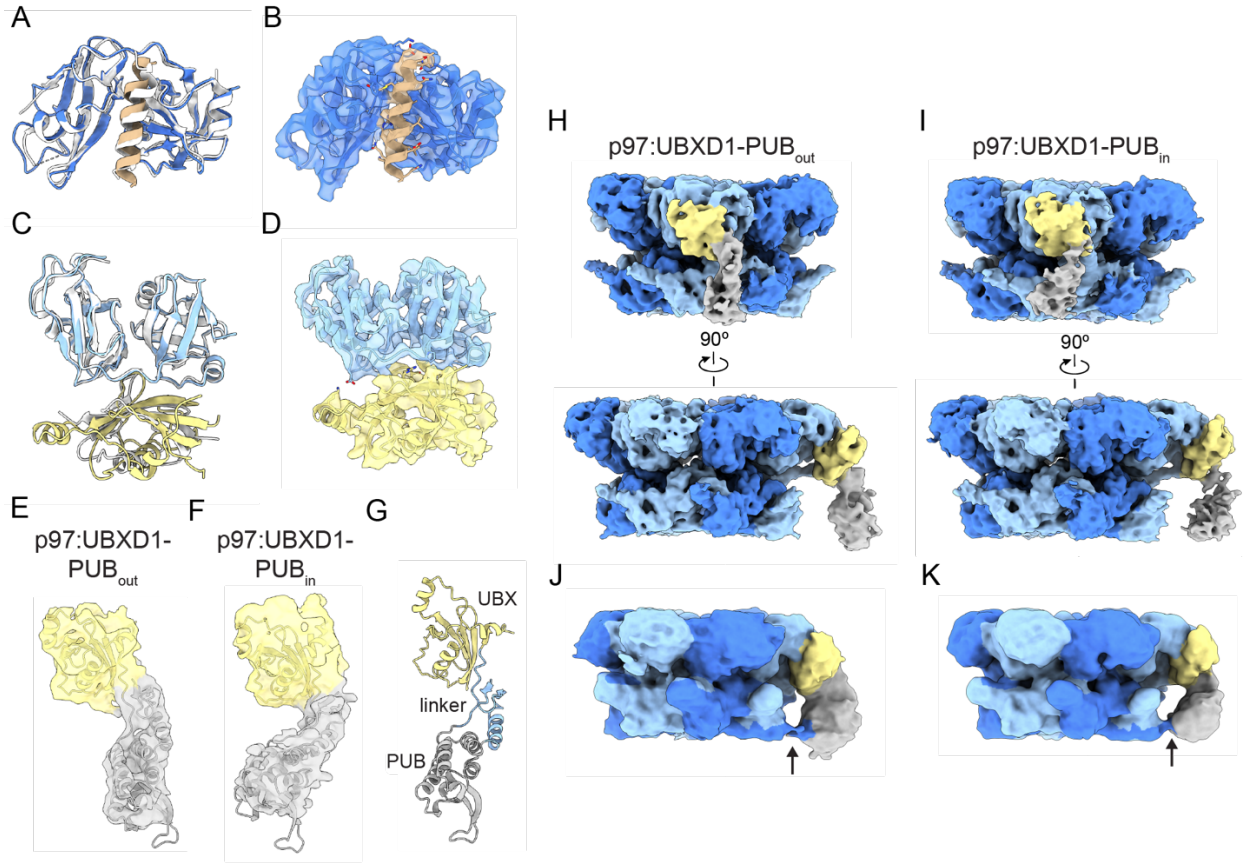

Figure 2.S5 VIM, UBX, and PUB comparisons and validation
(**A**) Overlay of NTD-VIM from p97:UBXD1^{closed} (colored) and gp78 (PDB 3TIW, white). (**B**) Map and model of the NTD and VIM from p97:UBXD1^{closed}, colored as in (A). (**C**) Overlay of NTD-UBX from p97:UBXD1^{closed} (colored) and UBXD7 (PDB 5X4L, white). (**D**) Map and model of the NTD and UBX from p97:UBXD1^{closed}, colored as in (C). (**E**) Unsharpened, zoned map and model of UBX and PUB from p97:UBXD1-PUB$_{out}$. (**F**) Unsharpened, zoned map and model of UBX and PUB from p97:UBXD1-PUB$_{in}$. (**G**) Model of the UBX (yellow), PUB (gray), and UBX-PUB linker (light blue) from p97:UBXD1^{closed}. (**H**) Unsharpened map of p97:UBXD1-PUB$_{out}$. The VIM and helical lariat are colored the same as their corresponding protomers for clarity. (**I**) Unsharpened map of p97:UBXD1-PUB$_{in}$. The VIM and helical lariat are colored the same as their corresponding protomers for clarity. (**J**) Filtered map of p97:UBXD1-PUB$_{out}$, colored as in (D), showing weak density connecting the PUB and P5 CT tail. (**K**) As in (J), but for p97:UBXD1-PUB$_{in}$.

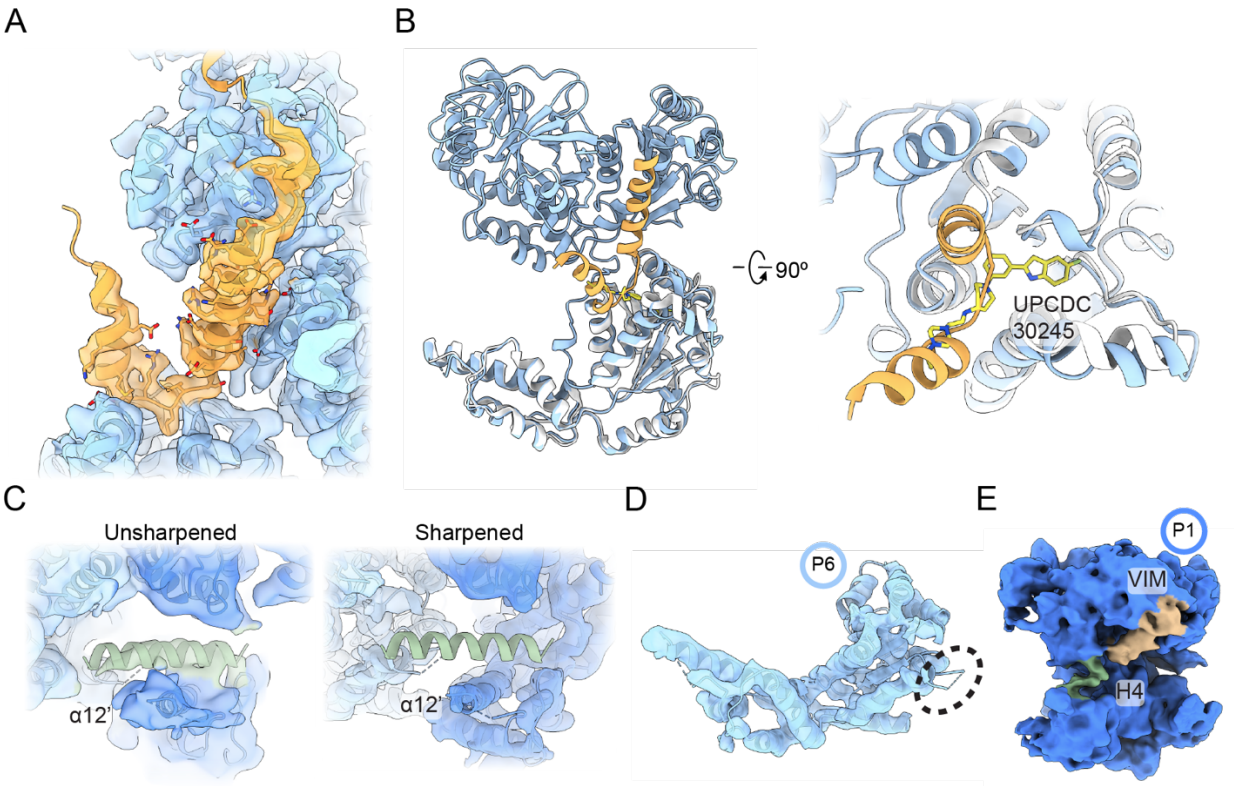

Figure 2.S6 Validation of the helical lariat, UPCDC30245 binding, and additional structural features of p97:UBXD1^{H4} and p97:UBXD1^{open}

(**A**) Sharpened map and model of Lα2-4, connecting strands of the helical lariat, and adjacent regions of P6 of p97:UBXD1^{meta}, colored as in **Figure 2.1**. (**B**) Overlay of P6 (blue) and Lα3-4 (orange) from p97:UBXD1^{closed} with a p97 protomer (white) bound to UPCDC30245 (yellow) (PDB 5FTJ), aligned by the D2 domain (residues 483-763). (**C**) View of H4 and surrounding p97 density in p97:UBXD1^{H4} (left: unsharpened, right: sharpened) overlaid with the model for this state. (**D**) Sharpened map and model of the D2 domain of protomer P6 of p97:UBXD1^{H4}, showing lack of density for α5' (encircled). (**E**) Unsharpened map of protomer P1 of p97:UBXD1^{open}. Density putatively corresponding to H4 is colored in green.

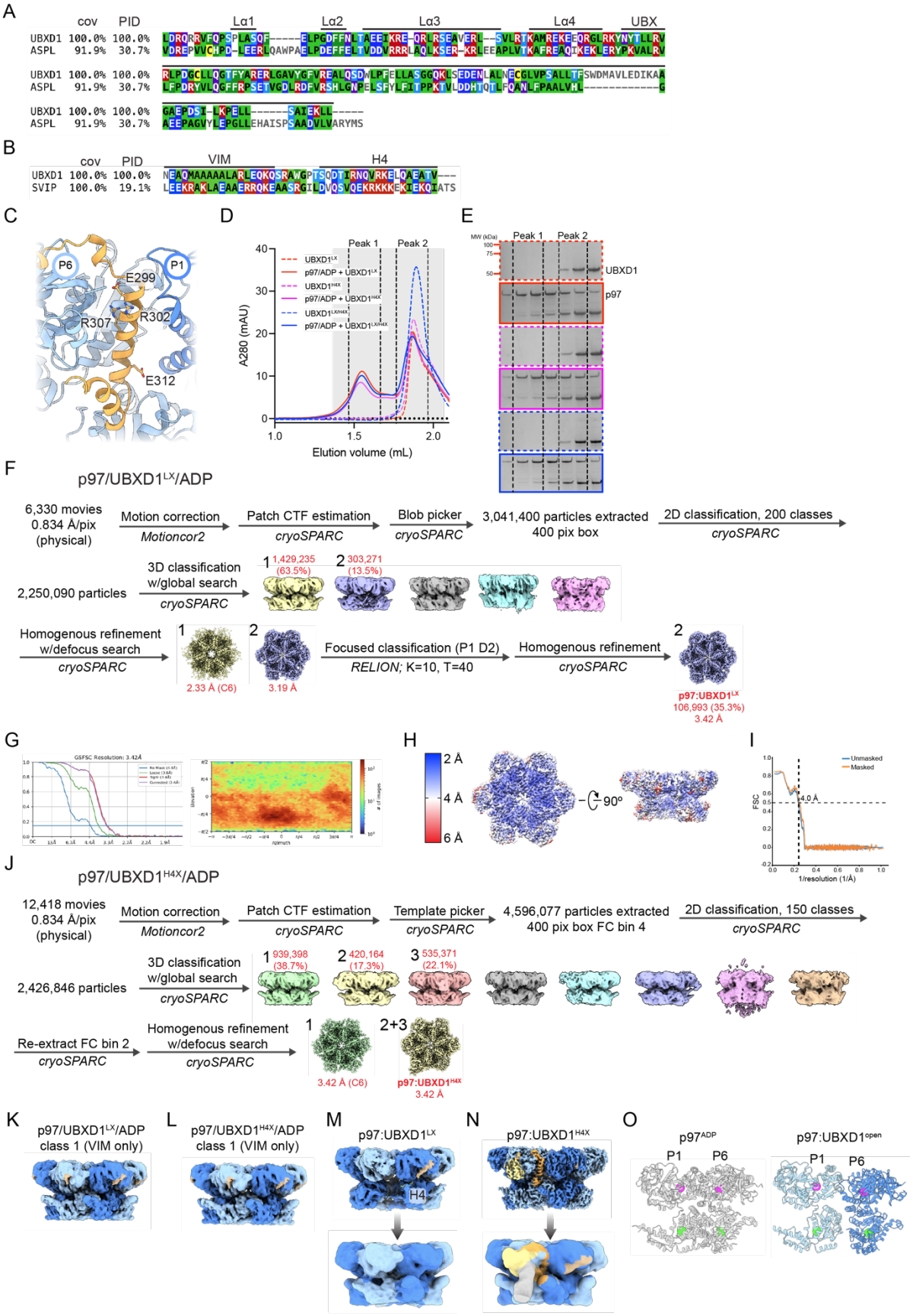
A
cov PID
Lα1 Lα2 Lα3 Lα4 UBX
UBXD1 100.0% 100.0%
ASPL 91.9% 30.7%
B
cov PID
VIM H4
UBXD1 100.0% 100.0%
SVIP 100.0% 19.1%
C
P6
P1
E299
R307
R302
E312
D
Peak 1
Peak 2
UBXD1LX
p97/ADP + UBXD1LX
UBXD1H4X
p97/ADP + UBXD1H4X
UBXD1LX/H4X
p97/ADP + UBXD1LX/H4X
A280 (mAU)
Elution volume (mL)
E
MW (kDa)
Peak 1
Peak 2
UBXD1
p97
F
p97/UBXD1LX/ADP
6,330 movies
0.834 Å/pix
(physical)
Motion correction
Motioncor2
Patch CTF estimation
cryoSPARC
Blob picker
cryoSPARC
3,041,400 particles extracted
400 pix box
2D classification, 200 classes
cryoSPARC
2,250,090 particles
3D classification
w/global search
cryoSPARC
1,429,235
(63.5%)
303,271
(13.5%)
Homogenous refinement
w/defocus search
cryoSPARC
2.33 Å (C6)
3.19 Å
Focused classification (P1 D2)
RELION; K=10, T=40
Homogenous refinement
cryoSPARC
p97:UBXD1LX
106,993 (35.3%)
3.42 Å
G
GSFSC Resolution: 3.42Å
H
2 Å
4 Å
6 Å
90°
I
Unmasked
Masked
4.0 Å
FSC
1/resolution (1/Å)
J
p97/UBXD1H4X/ADP
12,418 movies
0.834 Å/pix
(physical)
Motion correction
Motioncor2
Patch CTF estimation
cryoSPARC
Template picker
cryoSPARC
4,596,077 particles extracted
400 pix box FC bin 4
2D classification, 150 classes
cryoSPARC
2,426,846 particles
3D classification
w/global search
cryoSPARC
939,398
(38.7%)
420,164
(17.3%)
535,371
(22.1%)
Re-extract FC bin 2
cryoSPARC
Homogenous refinement
w/defocus search
cryoSPARC
3.42 Å (C6)
p97:UBXD1H4X
3.42 Å
K
p97/UBXD1LX/ADP
class 1 (VIM only)
L
p97/UBXD1H4X/ADP
class 1 (VIM only)
M
p97:UBXD1LX
H4
N
p97:UBXD1H4X
O
p97ADP
P1
P6
p97:UBXD1open
P1
P6

Figure 2.S7 Conservation and structural analysis of UBXD1, ASPL, and SVIP
(**A**) Alignment of UBX-lariat sequences from UBXD1 (residues 270-441) and ASPL (residues 318-495). Structural elements in the UBXD1 sequence are indicated above. Cov = covariance relative to the human sequence, Pid = percent identity relative to the human sequence. (**B**) Alignment of VIM-H4 sequences from UBXD1 (residues 50-93) and SVIP (residues 18-64). Structural elements in the UBXD1 sequence are indicated above. (**C**) Residues mutated in Lα3 of the UBXD1 helical lariat, shown on p97:UBXD1^{closed}. (**D**) SEC traces of UBXD1 mutants alone or incubated with p97 and ADP, showing a left shift in peak elution volume for p97 samples with UBXD1. Fractions in the shaded range were analyzed by SDS-PAGE. (**E**) Coomassie Brilliant Blue-stained SDS-PAGE gels of fractions from SEC runs in (D). (**F**) Cryo-EM processing workflow for the p97/UBXD1^{LX}/ADP dataset. (**G**) FSC curve and particle orientation distribution plot for p97:UBXD1^{LX}. (**H**) Sharpened density map colored by local resolution (0.143 cutoff) of p97:UBXD1^{LX}. (**I**) Map-model FSC for p97:UBXD1^{LX}. Displayed resolution was determined using the masked map. (**J**) Cryo-EM processing workflow for the p97/UBXD1^{H4X}/ADP dataset. (**K**) Unsharpened map of class 1 from p97/UBXD1^{LX}/ADP dataset. (**L**) Unsharpened map of class 1 from p97/UBXD1^{H4X}/ADP. (**M**) Top: unsharpened map of p97:UBXD1^{LX}. Note lack of density for the D2 domain of the protomer clockwise from the VIM/H4 bound protomer. Bottom: filtered map, colored only by p97 density, confirming that density for the aforementioned D2 domain is present. (**N**) Top: sharpened map of p97:UBXD1^{H4X}, colored as in **Figure 2.1**. Bottom: filtered map, confirming that density for the PUB domain is present. (**O**) Positions of calculated centroids for D1 (residues 210-458, magenta spheres) and D2 domains (residues 483-763, green spheres) of P1 and P6, for p97^{ADP} and p97:UBXD1^{open}.

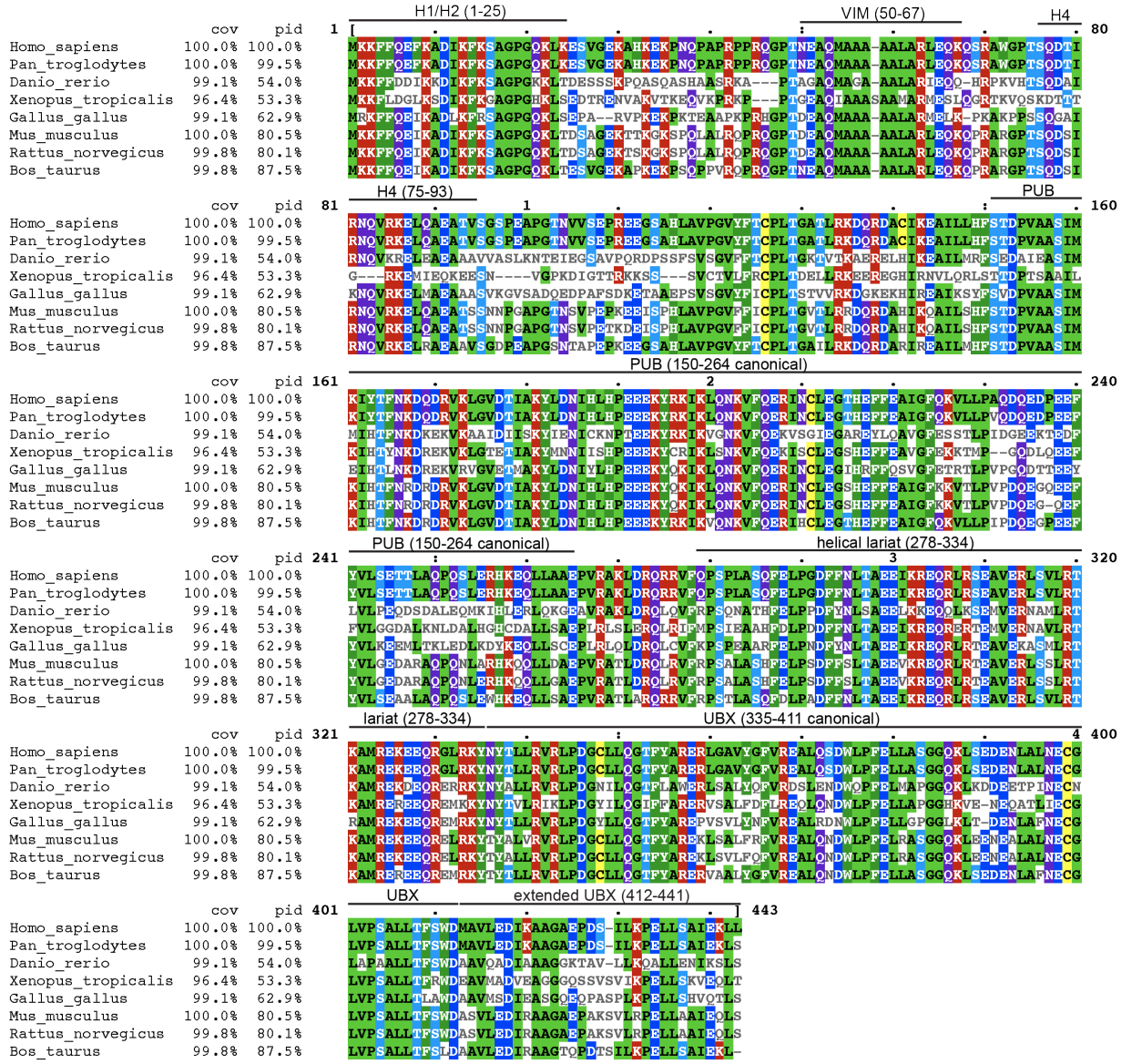

Figure 2.S8 Alignment of UBXD1 sequences

Multiple sequence alignment of UBXD1 homologs from *Homo sapiens*, *Mus musculus*, *Xenopus tropicalis*, *Gallus gallus*, *Rattus norvegicus*, *Bos taurus*, *Pan troglodytes*, and *Danio rerio*. Structural elements and residue ranges (in the human sequence) are marked above. Cov = covariance relative to the human sequence, Pid = percent identity relative to the human sequence.

Tables

Table 2.1 Cryo-EM data collection, refinement, and validation statistics of structures from the p97/UBXD1^{WT}/ADP and p97/UBXD1^{LX}/ADP datasets

	p97: UBXD1^{closed} (EMD-28982, PDB 8FCL)	p97: UBXD1^{open} (EMD-28983, PDB 8FCM)	p97: UBXD1^{VIM} (EMD-28987, PDB 8FCN)	p97: UBXD1^{meta} (EMD-28988, PDB 8FCO)	p97: UBXD1^{para} (EMD-28989, PDB 8FCP)	p97: UBXD1-PUB$_{in}$ (EMD-28990, PDB 8FCQ)	p97: UBXD1^{H4} (EMD-28991, PDB 8FCR)	p97: UBXD1^{LX} (EMD-28992, PDB 8FCT)
Data collection and processing								
Microscope and camera	Titan Krios, K3	Titan Krios, K3	Titan Krios, K3	Titan Krios, K3	Titan Krios, K3	Titan Krios, K3	Titan Krios, K3	Titan Krios, K3
Magnification	59,952	59,952	59,952	59,952	59,952	59,952	59,952	59,952
Voltage (kV)	300	300	300	300	300	300	300	300
Data acquisition software	SerialEM	SerialEM	SerialEM	SerialEM	SerialEM	SerialEM	SerialEM	SerialEM
Exposure navigation	Image shift	Image shift	Image shift	Image shift	Image shift	Image shift	Image shift	Image shift
Electron exposure ($e^-/Å^2$)	43	43	43	43	43	43	43	43
Defocus range (μm)	-0.5 to -2.0	-0.5 to -2.0	-0.5 to -2.0	-0.5 to -2.0	-0.5 to -2.0	-0.5 to -2.0	-0.5 to -2.0	-0.5 to -2.0
Pixel size (Å)	0.834	0.834	0.834	0.834	0.834	0.834	0.834	0.834
Symmetry imposed	C1	C1	C6	C1	C2	C1	C1	C1
Initial particle images (no.)	5,498,937	5,498,937	5,498,937	5,498,937	5,498,937	5,498,937	5,498,937	2,250,090
Final particle images (no.)	82,334	563,468	100,000	80,700	45,628	59,126	24,086	106,993
Map resolution (Å)	3.5	3.3 (consensus)	3.0	3.3	3.5	3.9	4.1	3.4
FSC threshold	0.143	0.143	0.143	0.143	0.143	0.143	0.143	0.143
Map resolution range (Å)	2-10	2-10	2-10	2-10	2-10	3-12	3-12	2.5-10
Refinement								
Model resolution (Å)	4.3	3.8	3.4	4.2	4.1	6.2	6.2	4.0
FSC threshold	0.5	0.5	0.5	0.5	0.5	0.5	0.5	0.5
Map sharpening *B* factor ($Å^2$)	-93.5	-86.1 (consensus)	-113.6	-96.8	-108.4	-90.4	-133.3	-107.0
Model composition								
Nonhydrogen atoms	36,904	36,829	35,034	39,569	39,494	36,904	36,931	34,329
Protein residues	4,667	4,658	4,446	4,999	4,990	4,667	4,679	4,356
Ligands	12	12	12	12	12	12	12	12
B factors ($Å^2$)								
Protein	30.09	30.08	27.06	33.80	33.80	30.09	30.19	26.10
Ligand	13.34	13.34	13.34	13.34	13.34	13.34	13.34	13.34
R. m. s. deviations								
Bond lengths (Å)	0.011	0.011	0.011	0.011	0.011	0.011	0.011	0.011
Bond angles (°)	1.087	1.064	1.040	1.091	1.092	1.063	1.067	1.040
Validation								
MolProbity score	0.72	0.83	0.71	0.82	0.81	0.83	0.87	0.71
Clashscore	0.67	1.16	0.65	1.13	1.07	1.15	1.40	0.62
Poor rotamers (%)	0.10	0.00	0.11	0.00	0.00	0.03	0.00	0.05
Ramachandran plot								
Favored (%)	98.17	98.08	98.66	98.27	98.12	98.23	98.19	98.52
Allowed (%)	1.79	1.77	1.20	1.65	1.76	1.70	1.70	1.34
Disallowed (%)	0.04	0.15	0.14	0.08	0.12	0.06	0.11	0.14

Supplemental Files

Movie 2.1 p97:UBXD1^{closed} and p97:UBXD1^{open} states

Sharpened maps and models for p97:UBXD1^{closed} and p97:UBXD1^{open} are shown.

Movie 2.2 Transition between p97^{ADP}, p97:UBXD1^{closed} and p97:UBXD1^{open}

Morphs between models of p97^{ADP} (PDB 5FTK), p97:UBXD1^{closed} and p97:UBXD1^{open} are shown.

Movie 2.3 3D variability analysis of p97:UBXD1^{closed} and p97:UBXD1^{open}

Volumes calculated from the first component of a 3D Variability Analysis job using particles in the closed and open states are shown, colored as in **Figure 2.1**. This identifies a clear hexamer opening and upward and downward rotation of protomers P6 and P1, respectively.

Movie 2.4 H4 binding disrupts p97 D2 inter-protomer contacts

Morph between p97:UBXD1^{closed} and p97:UBXD1^{H4} is shown, showing rotation of bound D2 domain and disruption of contact with α5' (red) of clockwise adjacent protomer.

Movie 2.5 3D variability analysis of p97:UBXD1^{LX}

Volumes calculated from the third principal component of a 3D Variability Analysis job using particles from class 2 of the p97:UBXD1^{LX} dataset are shown. This reveals a transition from a p97 hexamer without appreciable density corresponding to UBXD1 and ordered D2 domains to a hexamer with strong VIM and H4 density. In this state, the H4-bound D2 domain rotates upward and density for the D2 domain of the clockwise protomer disappears, indicating flexibility.

Movie 2.6 Summary of p97:UBXD1 interactions

UBXD1 domains are shown binding to the p97 hexamer in p97:UBXD1^{H4}.

Methods

Molecular cloning

The coding sequence of full-length human UBXD1 was cloned with an N-terminal 6xHis tag, MBP tag, and TEV protease cleavage site into an insect cell expression vector (Addgene plasmid #55218). The same expression construct was cloned into a bacterial expression vector (Addgene plasmid #29708). ASPL-C (residues 313-553) and full-length SVIP were cloned into the same expression vector. The NEB Q5 Site-Directed Mutagenesis kit was used to introduce mutations into the UBXD1 construct. The UBXD1 lariat was mutated by making four charge reversals in Lα3 predicted to disrupt contacts with P1 and P6 (E299R/R302E/R307E/E312R), given this helix makes the most significant contacts with p97. As we could not obtain high-resolution structural information about H4, we scrambled the sequence of this helix rather than making point mutants, using Peptide Nexus Sequence Scrambler (https://peptidenexus.com/article/sequence-scrambler). This resulted in the sequence 75-QSRDVTQERIQNKAVLTEA-93.

Protein expression and purification

p97 was expressed and purified as described previously (55). Briefly, BL21-Gold(DE3) chemically competent *E. coli* (Agilent) were transformed with pET15b p97, encoding full-length p97 with an N-terminal 6xHis tag, grown in 2xYT media supplemented with 100 µg/mL carbenicillin, and induced with 0.5 mM isopropyl β-D-1-thiogalactopyranoside (IPTG) at 20°C overnight. Cells were harvested and lysed by sonication in lysis buffer (50 mM Tris pH 8.0, 250 mM NaCl, 10 mM imidazole, 0.5 mM Tris(2-carboxyethyl)phosphine (TCEP), 1 mM phenylmethylsulfonyl fluoride (PMSF)) supplemented with cOmplete Protease Inhibitor Cocktail, EDTA-free (Roche) then clarified by centrifugation. The supernatant was then incubated with HisPur Ni-NTA resin (Thermo Scientific), and p97 was eluted with nickel elution buffer (lysis buffer supplemented with 320 mM imidazole, no PMSF). The eluate was supplemented with TEV protease and dialyzed overnight at 4°C into p97 dialysis buffer (10 mM Tris pH 8.0, 100 mM NaCl, 1 mM dithiothreitol (DTT)). The

following day, the cleavage product was passed through fresh Ni-NTA resin, and the flowthrough was concentrated and applied to a HiLoad 16/600 Superdex 200 pg size exclusion chromatography (SEC) column (GE Healthcare) equilibrated in p97 SEC buffer (25 mM HEPES pH 7.4, 150 mM KCl, 5 mM $MgCl_2$, 0.5 mM TCEP). Fractions containing p97 were concentrated to >200 µM, filtered, and flash frozen in liquid nitrogen.

Initial attempts at expression of UBXD1 in *E. coli* resulted in large amounts of insoluble material. Therefore, to obtain amounts sufficient for initial studies, a UBXD1 construct with a TEV-cleavable N-terminal 6xHis-MBP tag was expressed in Sf9 insect cells using standard methods. This protocol (including cleavage of the 6xHis-MBP tag) yielded sufficient material for preliminary cryo-EM studies, and was used for the p97/UBXD1^{WT}/ADP dataset. Thereafter, an optimization campaign for soluble expression of 6xHis-MBP-UBXD1 in *E. coli* was performed, which resulted in the following protocol. *E. coli*-derived UBXD1 and mutants thereof were used for all biochemical experiments, and the p97/UBXD1/ATPγS, p97/UBXD1^{LX}/ADP and p97/UBXD1^{H4X}/ADP datasets. BL21-Gold(DE3) chemically competent *E. coli* (Agilent) were transformed with the UBXD1 expression vectors and used for large-scale expression. Cells were grown in 2xYT media supplemented with 100 µg/mL carbenicillin at 37°C until OD_{600} reached ~1.25, then protein expression was induced with 0.5 mM IPTG, and grown for 1 hour at 37°C. Cells were rapidly cooled in an ice bath for 10 min, then harvested by centrifugation at 10,000 RCF and stored at -80°C until use. All subsequent steps were performed at 4°C. Pellets were resuspended in lysis buffer (see above) supplemented with cOmplete Protease Inhibitor Cocktail, EDTA-free (Roche), and lysed by sonication. Lysates were clarified by centrifugation at 85,000 RCF and incubated with HisPur Ni-NTA resin (Thermo Scientific) for 15 min. The resin was washed with nickel wash buffer (lysis buffer without imidazole or PMSF) and eluted with nickel elution buffer (see above). The eluate was concentrated, filtered, and applied to a HiLoad 16/600 Superdex 200 pg SEC column (GE Healthcare) equilibrated in adapter SEC buffer (25 mM HEPES pH 7.4, 150 mM KCl,

5% glycerol (v/v), 0.5 mM TCEP). TEV protease was added to fractions containing MBP-UBXD1 and incubated overnight without agitation. The following day, the sample was passed through a 5 mL MBPTrap HP column (GE Healthcare) to remove the cleaved 6xHis-MBP tag, and the flowthrough was concentrated before 15x dilution with anion exchange (AEX) binding buffer (25 mM HEPES pH 7.5, 0.5 mM TCEP). The diluted sample was then applied to a 1 mL HiTrap Q HP column (GE Healthcare), and UBXD1 was eluted with a 0-50% gradient of AEX elution buffer (AEX binding buffer supplemented with 1000 mM KCl), concentrated to >200 μM, and flash frozen in liquid nitrogen.

To express ASPL-C and SVIP, BL21-Gold(DE3) were transformed with pET MBP-ASPL-C and pET MBP-SVIP, and grown in Terrific Broth supplemented with 100 μg/mL ampicillin at 37°C until OD_{600} reached ~2, then protein expression was induced with 0.4 mM IPTG, and grown overnight at 18°C. Cells were harvested by centrifugation at 4,000 RCF and stored at -80°C or processed immediately. All subsequent steps were performed at 4°C. Cell lysis and nickel immobilized metal affinity chromatography were performed as for UBXD1. TEV protease was added to the eluates, and the solutions were dialyzed overnight in adapter dialysis buffer (25 mM Tris pH 8.0, 150 mM NaCl, 0.5 mM TCEP). The following day, the samples were passed through fresh Ni-NTA resin to remove the 6xHis-MBP tags, concentrated, and applied to a HiLoad 16/600 Superdex 200 pg SEC column equilibrated in adapter SEC buffer. Fractions containing adapter proteins were concentrated to >200 μM and flash frozen in liquid nitrogen.

Purity of all proteins was verified by SDS-PAGE and concentration was determined using the Pierce BCA Protein Assay Kit (Thermo Scientific).

ATPase assays

The ATPase assay protocol was modified from previously published methods (60). In an untreated 384-well microplate (Grenier 781101), 50 μL solutions were prepared to a final concentration of 10 nM p97 hexamer, variable adapter (UBXD1 and mutants, ASPL-C, and SVIP),

and 200 μM ATP (Thermo Fisher Scientific) in ATPase buffer (25 mM HEPES pH 7.4, 100 mM KCl, 3 mM $MgCl_2$, 1 mM TCEP, 0.1 mg/mL BSA). ATP was added last to initiate the reaction, and the solutions were incubated at room temperature until 8% substrate hydrolysis was achieved. To quench the reaction, 50 μL of BIOMOL Green (Enzo Life Sciences) was added and allowed to develop at room temperature for 25 min before reading at 620 nm.

Analytical size exclusion chromatography

60 μL samples (10 μM p97 monomer, 20 μM UBXD1, and 5 mM nucleotide where applicable) were prepared in p97 SEC buffer and incubated on ice for 10 minutes. Samples were filtered and injected on a Superose 6 Increase 3.2/300 column (GE Healthcare) equilibrated in p97 SEC buffer and operated at 8°C. 100 μL fractions were collected and analyzed by SDS-PAGE with Coomassie Brilliant Blue R-250 staining (Bio-Rad).

Cryo-EM data collection and processing

For all p97/UBXD1 datasets, 10 μM p97 monomer and 20 μM UBXD1 were incubated with 5 mM ADP or ATPγS in p97 SEC buffer for 10 minutes on ice before vitrification. A 3 μL drop was applied to a glow-discharged (PELCO easiGlow, 15 mA, 2 min) holey carbon grid (Quantifoil R1.2/1.3 on gold 200 mesh support), blotted for 3-4 seconds with Whatman Grade 595 filter paper (GE Healthcare), and plunge frozen into liquid ethane cooled by liquid nitrogen using a Vitrobot (Thermo Fisher Scientific) operated at 4°C and 100% humidity. Samples were imaged on a Titan Krios TEM (Thermo Fisher Scientific) operated at 300 kV and equipped with a BioQuantum K3 Imaging Filter (Gatan) using a 20 eV zero loss energy slit. Movies were acquired with SerialEM (61) in super-resolution ($UBXD1^{WT}$/ADP, $UBXD1^{H4X}$/ADP, $UBXD1^{WT}$/ATPγS) or counted ($UBXD1^{LX}$/ADP) mode at a calibrated magnification of 59,952x, corresponding to a physical pixel size of 0.834 Å. A nominal defocus range of -0.8 to -1.8 μm was used with a total exposure time of 2 sec fractionated into 0.255 sec frames for a total dose of 43 $e^-/Å^2$ at a dose rate of 15 e^-/pix/s.

Movies were subsequently corrected for drift and dose-weighted using MotionCor2 (62), and the micrographs collected in super-resolution mode were Fourier cropped by a factor of 2.

For the p97/UBXD1^{WT}/ADP sample, a total of 22,536 micrographs were collected and initially processed in cryoSPARC (63). After Patch CTF estimation, micrographs were manually curated to exclude those of poor quality, followed by blob-based particle picking, 2D classification, *ab initio* modeling, and initial 3D classification. Three classes of interest from the initial 3D classification were identified, corresponding to a closed-like state (class 1), an open-like state (class 2), and p97:UBXD1^{VIM} (class 3). For p97:UBXD1^{VIM}, 100,000 particles were randomly selected and refined with C6 symmetry imposed. For the open state, refinement of all particles produced a map with poor resolution for protomers P1 and P6, so focused classification without image alignment (skip-align) of these individual protomers was performed in RELION (64), followed by masked local refinement in cryoSPARC. A composite map of these two local refinements and protomers P2-P5 from the consensus map was generated in UCSF Chimera by docking the local refinement maps into the consensus map, zoning each map by a radius of 4 Å using the associated chains, and summing the aligned volumes (65). For the closed state, refinement of the closed-like particles revealed additional UBXD1 density at protomers other than P1 and P6, so skip-align focused classification using a mask encompassing protomers with additional density was performed in RELION, followed by homogenous refinement in cryoSPARC, yielding the p97:UBXD1^{meta} and p97:UBXD1^{para} states. The class from focused classification corresponding to a singly-bound hexamer was also refined in cryoSPARC, and then subjected to skip-align focused classification of P1 and P6 in RELION, followed by homogenous refinement in cryoSPARC. This yielded the p97:UBXD1^{closed} and p97:UBXD1^{H4} states. To obtain better density for the PUB domain, all particles from the closed-like class from the initial 3D classification were used for skip-align focused classification of the PUB and UBX domain in RELION, followed by homogenous refinement in cryoSPARC. This yielded p97:UBXD1-PUB$_{out}$ and p97:UBXD1-PUB$_{in}$.

To visualize variability in this dataset, 3D Variability Analysis in cryoSPARC was performed using particles from the closed-like and open-like states.

For the p97/UBXD1^{WT}/ATPγS dataset, a total of 9,498 micrographs were collected and initially processed as for p97/UBXD1^{WT}/ADP. An initial 3D classification revealed three classes of interest: a state resembling p97:UBXD1^{closed}, a state resembling a fully ATPγS-bound p97 hexamer with NTDs in the up state, and a state resembling the p97:UBXD1^{VIM} state. Homogenous refinement with defocus refinement was performed for each of these classes, and the resolution in all maps was sufficient to assign nucleotide density as ATPγS in all nucleotide pockets in all protomers in all structures.

For the p97/UBXD1^{LX}/ADP sample, a total of 6,330 micrographs were collected and initially processed as for p97/UBXD1^{WT}/ADP. An initial 3D classification revealed two high-resolution classes, one featuring density for the UBXD1 VIM in all NTDs (class 1), and the other featuring stronger density for the VIM in one NTD than in the others (class 2). In this class the D2 domain of the protomer counterclockwise from the best VIM-bound protomer had significantly weaker density, indicating flexibility. Homogenous refinement of class 1 produced a map essentially identical to p97:UBXD1^{VIM}. Homogenous refinement of class 2 produced a map with density weak density putatively corresponding to H4 on the strong VIM-bound protomer, so skip-align focused classification of the D2 domain of this protomer was performed in RELION, followed by a final homogenous refinement in cryoSPARC of the best class. This yielded a map with improved VIM and H4 density. To visualize variability in this dataset, 3D Variability Analysis in cryoSPARC was performed using particles from the class 2 refinement (pre-focused classification).

For the p97/UBXD1^{H4X}/ADP sample, a total of 12,418 micrographs were collected and initially processed as for p97/UBXD1^{WT}/ADP. An initial 3D classification revealed three high-resolution classes, one featuring density for the UBXD1 VIM in all NTDs (class 1), and the other

two (classes 2 and 3) featuring stronger density for the VIM and additional UBXD1 domains, including the PUB, helical lariat, and UBX. These classes strongly resemble p97:UBXD1^{closed}. Homogenous refinement of class 1 produced a map essentially identical to p97:UBXD1^{VIM}. Homogenous refinement of classes 2 and 3 combined produced a map with density for the VIM, PUB, lariat, and UBX, but without H4 density or associated movements of the D2 domains. To identify particles with H4 density, skip-align focused classification of protomers P1 and P6 was performed in RELION, which did not reveal any classes with density attributable to H4.

Molecular modeling

To generate the model for p97:UBXD1^{closed}, a model of the p97^{ADP} hexamer (19) and the AlphaFold model of UBXD1 (44, 45) were docked into the map using UCSF Chimera (65) and ISOLDE (66) in UCSF ChimeraX (67), followed by refinement using Rosetta Fast Torsion Relax. Models for all other structures were generated by docking individual chains from the closed model, followed by refinement using Rosetta Fast Torsion Relax. Coot (68), ISOLDE, and Phenix (69) were used to finalize all models. Sidechains for H4 residues in p97:UBXD1^{H4} and p97:UBXD1^{LX} are omitted due to low resolution.

UBXD1 sequence alignment

UBXD1 protein sequences were aligned in MUSCLE and the resulting alignment was visualized in MView (70).

Data analysis and figure preparation

Biochemical data was analyzed and plotted using Prism 9.3.1 (GraphPad). Figures were prepared using Adobe Illustrator, UCSF Chimera, and UCSF ChimeraX (65, 67).

Resource Availability

Materials availability:

Requests for resources and reagents should be directed to Daniel R. Southworth.

Data availability:

Cryo-EM densities have been deposited at the Electron Microscopy Data Bank under accession codes EMD: 28982 (p97:UBXD1^{closed}), EMD: 28983 (p97:UBXD1^{open} composite), EMD: 28984 (p97:UBXD1^{open} consensus), EMD: 28985 (p97:UBXD1^{open} P1 focused map), EMD: 28986 (p97:UBXD1^{open} P6 focused map), EMD: 28987 (p97:UBXD1^{VIM}), EMD: 28988 (p97:UBXD1^{meta}), EMD: 28989 (p97:UBXD1^{para}), EMD: 28990 (p97:UBXD1-PUB$_{in}$), EMD: 28991 (p97:UBXD1^{H4}), and EMD: 28992 (p97:UBXD1^{LX}). Atomic coordinates have been deposited at the Protein Data Bank under accession codes PDB: 8FCL (p97:UBXD1^{closed}), PDB: 8FCM (p97:UBXD1^{open}), PDB: 8FCN (p97:UBXD1^{VIM}), PDB: 8FCO (p97:UBXD1^{meta}), PDB: 8FCP (p97:UBXD1^{para}), PDB: 8FCQ (p97:UBXD1-PUB$_{in}$), PDB: 8FCR (p97:UBXD1^{H4}), and PDB: 8FCT (p97:UBXD1^{LX}).

Acknowledgments

This work was supported by NIH grants F31GM142279 (to J.R.B.), R01GM130145 (to M.R.A.), and R01GM138690 (to D.R.S.).

Author Contributions

J.R.B. expressed and purified proteins, performed biochemical and cryo-EM experiments, built models, developed figures, and wrote and edited the manuscript. C.R.A. expressed and purified proteins, performed biochemical experiments, and edited the manuscript. M.R.T. expressed and purified proteins and performed cryo-EM experiments. E.T. operated electron microscopes and assisted with data collection. A.T. expressed proteins. M.R.A. designed and supervised biochemistry and edited the manuscript. D.R.S. designed and supervised the project and wrote and edited the manuscript.

References

1. Stach, L., and Freemont, P. S. (2017) The AAA+ ATPase p97, a cellular multitool. *Biochem J*. 474, 2953–2976
2. Boom, J. van den, and Meyer, H. (2018) VCP/p97-Mediated Unfolding as a Principle in Protein Homeostasis and Signaling. *Mol Cell*. 69, 182–194
3. Watts, G. D. J., Wymer, J., Kovach, M. J., Mehta, S. G., Mumm, S., Darvish, D., Pestronk, A., Whyte, M. P., and Kimonis, V. E. (2004) Inclusion body myopathy associated with Paget disease of bone and frontotemporal dementia is caused by mutant valosin-containing protein. *Nat Genet*. 36, 377–381
4. Darwich, N. F., Phan, J. M., Kim, B., Suh, E., Papatriantafyllou, J. D., Changolkar, L., Nguyen, A. T., O'Rourke, C. M., He, Z., Porta, S., Gibbons, G. S., Luk, K. C., Papageorgiou, S. G., Grossman, M., Massimo, L., Irwin, D. J., McMillan, C. T., Nasrallah, I. M., Toro, C., Aguirre, G. K., Deerlin, V. M. V., and Lee, E. B. (2020) Autosomal dominant VCP hypomorph mutation impairs disaggregation of PHF-tau. *Science*. 10.1126/science.aay8826
5. Johnson, J. O., Mandrioli, J., Benatar, M., Abramzon, Y., Deerlin, V. M. V., Trojanowski, J. Q., Gibbs, J. R., Brunetti, M., Gronka, S., Wuu, J., Ding, J., McCluskey, L., Martinez-Lage, M., Falcone, D., Hernandez, D. G., Arepalli, S., Chong, S., Schymick, J. C., Rothstein, J., Landi, F., Wang, Y.-D., Calvo, A., Mora, G., Sabatelli, M., Monsurrò, M. R., Battistini, S., Salvi, F., Spataro, R., Sola, P., Borghero, G., Consortium, T. I., Galassi, G., Scholz, S. W., Taylor, J. P., Restagno, G., Chiò, A., and Traynor, B. J. (2010) Exome Sequencing Reveals VCP Mutations as a Cause of Familial ALS. *Neuron*. 68, 857–864
6. Huryn, D. M., Kornfilt, D. J. P., and Wipf, P. (2019) p97: An Emerging Target for Cancer, Neurodegenerative Diseases, and Viral Infections. *J Med Chem*. 63, 1892–1907
7. Fessart, D., Marza, E., Taouji, S., Delom, F., and Chevet, E. (2013) P97/CDC-48: Proteostasis control in tumor cell biology. *Cancer Lett*. 337, 26–34

8. Cooney, I., Han, H., Stewart, M. G., Carson, R. H., Hansen, D. T., Iwasa, J. H., Price, J. C., Hill, C. P., and Shen, P. S. (2019) Structure of the Cdc48 segregase in the act of unfolding an authentic substrate. *Science*. 365, 502–505
9. Twomey, E. C., Ji, Z., Wales, T. E., Bodnar, N. O., Ficarro, S. B., Marto, J. A., Engen, J. R., and Rapoport, T. A. (2019) Substrate processing by the Cdc48 ATPase complex is initiated by ubiquitin unfolding. *Science*. 365, eaax1033
10. Stein, A., Ruggiano, A., Carvalho, P., and Rapoport, T. A. (2014) Key Steps in ERAD of Luminal ER Proteins Reconstituted with Purified Components. *Cell*. 158, 1375–1388
11. Brandman, O., Stewart-Ornstein, J., Wong, D., Larson, A., Williams, C. C., Li, G.-W., Zhou, S., King, D., Shen, P. S., Weibezahn, J., Dunn, J. G., Rouskin, S., Inada, T., Frost, A., and Weissman, J. S. (2012) A Ribosome-Bound Quality Control Complex Triggers Degradation of Nascent Peptides and Signals Translation Stress. *Cell*. 151, 1042–1054
12. Papadopoulos, C., Kirchner, P., Bug, M., Grum, D., Koerver, L., Schulze, N., Poehler, R., Dressler, A., Fengler, S., Arhzaouy, K., Lux, V., Ehrmann, M., Weihl, C. C., and Meyer, H. (2016) VCP/p97 cooperates with YOD1, UBXD1 and PLAA to drive clearance of ruptured lysosomes by autophagy. *Embo J*. 36, 135–150
13. Tanaka, A., Cleland, M. M., Xu, S., Narendra, D. P., Suen, D.-F., Karbowski, M., and Youle, R. J. (2010) Proteasome and p97 mediate mitophagy and degradation of mitofusins induced by Parkin. *J Cell Biology*. 191, 1367–1380
14. Ritz, D., Vuk, M., Kirchner, P., Bug, M., Schütz, S., Hayer, A., Bremer, S., Lusk, C., Baloh, R. H., Lee, H., Glatter, T., Gstaiger, M., Aebersold, R., Weihl, C. C., and Meyer, H. (2011) Endolysosomal sorting of ubiquitylated caveolin-1 is regulated by VCP and UBXD1 and impaired by VCP disease mutations. *Nat Cell Biol*. 13, 1116–1123
15. Buchberger, A., Schindelin, H., and Hänzelmann, P. (2015) Control of p97 function by cofactor binding. *Febs Lett*. 589, 2578–2589

16. Hänzelmann, P., and Schindelin, H. (2017) The Interplay of Cofactor Interactions and Post-translational Modifications in the Regulation of the AAA+ ATPase p97. *Frontiers Mol Biosci*. 4, 21

17. Bento, A. C., Bippes, C. C., Kohler, C., Hemion, C., Frank, S., and Neutzner, A. (2018) UBXD1 is a mitochondrial recruitment factor for p97/VCP and promotes mitophagy. *Sci Rep-uk*. 8, 12415

18. DeLaBarre, B., and Brunger, A. T. (2003) Complete structure of p97/valosin-containing protein reveals communication between nucleotide domains. *Nat Struct Mol Biol*. 10, 856–863

19. Banerjee, S., Bartesaghi, A., Merk, A., Rao, P., Bulfer, S. L., Yan, Y., Green, N., Mroczkowski, B., Neitz, R. J., Wipf, P., Falconieri, V., Deshaies, R. J., Milne, J. L. S., Huryn, D., Arkin, M., and Subramaniam, S. (2016) 2.3 Å resolution cryo-EM structure of human p97 and mechanism of allosteric inhibition. *Science*. 351, 871–875

20. Huyton, T., Pye, V. E., Briggs, L. C., Flynn, T. C., Beuron, F., Kondo, H., Ma, J., Zhang, X., and Freemont, P. S. (2003) The crystal structure of murine p97/VCP at 3.6Å. *J Struct Biol*. 144, 337–348

21. Zhang, X., Shaw, A., Bates, P. A., Newman, R. H., Gowen, B., Orlova, E., Gorman, M. A., Kondo, H., Dokurno, P., Lally, J., Leonard, G., Meyer, H., Heel, M. van, and Freemont, P. S. (2000) Structure of the AAA ATPase p97. *Mol Cell*. 6, 1473–1484

22. Rouiller, I., DeLaBarre, B., May, A. P., Weis, W. I., Brunger, A. T., Milligan, R. A., and Wilson-Kubalek, E. M. (2002) Conformational changes of the multifunction p97 AAA ATPase during its ATPase cycle. *Nat Struct Biol*. 9, 950–957

23. Tang, W. K., Li, D., Li, C., Esser, L., Dai, R., Guo, L., and Xia, D. (2010) A novel ATP-dependent conformation in p97 N–D1 fragment revealed by crystal structures of disease-related mutants. *Embo J*. 29, 2217–2229

24. DeLaBarre, B., and Brunger, A. T. (2005) Nucleotide Dependent Motion and Mechanism of Action of p97/VCP. *J Mol Biol*. 347, 437–452

25. Pan, M., Yu, Y., Ai, H., Zheng, Q., Xie, Y., Liu, L., and Zhao, M. (2021) Mechanistic insight into substrate processing and allosteric inhibition of human p97. *Nat Struct Mol Biol*. 28, 614–625

26. Puchades, C., Rampello, A. J., Shin, M., Giuliano, C. J., Wiseman, R. L., Glynn, S. E., and Lander, G. C. (2017) Structure of the mitochondrial inner membrane AAA+ protease YME1 gives insight into substrate processing. *Science*. 358, eaao0464

27. Puchades, C., Sandate, C. R., and Lander, G. C. (2020) The molecular principles governing the activity and functional diversity of AAA+ proteins. *Nat Rev Mol Cell Bio*. 21, 43–58

28. Gates, S. N., Yokom, A. L., Lin, J., Jackrel, M. E., Rizo, A. N., Kendsersky, N. M., Buell, C. E., Sweeny, E. A., Mack, K. L., Chuang, E., Torrente, M. P., Su, M., Shorter, J., and Southworth, D. R. (2017) Ratchet-like polypeptide translocation mechanism of the AAA+ disaggregase Hsp104. *Science*. 357, 273–279

29. Rizo, A. N., Lin, J., Gates, S. N., Tse, E., Bart, S. M., Castellano, L. M., DiMaio, F., Shorter, J., and Southworth, D. R. (2019) Structural basis for substrate gripping and translocation by the ClpB AAA+ disaggregase. *Nat Commun*. 10, 2393

30. Bodnar, N. O., and Rapoport, T. A. (2017) Molecular Mechanism of Substrate Processing by the Cdc48 ATPase Complex. *Cell*. 169, 722-735.e9

31. Bodnar, N. O., Kim, K. H., Ji, Z., Wales, T. E., Svetlov, V., Nudler, E., Engen, J. R., Walz, T., and Rapoport, T. A. (2018) Structure of the Cdc48 ATPase with its ubiquitin-binding cofactor Ufd1-Npl4. *Nat Struct Mol Biol*. 25, 616–622

32. Weith, M., Seiler, J., Boom, J. van den, Kracht, M., Hülsmann, J., Primorac, I., Garcia, J. del P., Kaschani, F., Kaiser, M., Musacchio, A., Bollen, M., and Meyer, H. (2018) Ubiquitin-Independent Disassembly by a p97 AAA-ATPase Complex Drives PP1 Holoenzyme Formation. *Mol Cell*. 72, 766-777.e6

33. Kracht, M., Boom, J. van den, Seiler, J., Kröning, A., Kaschani, F., Kaiser, M., and Meyer, H. (2020) Protein Phosphatase-1 Complex Disassembly by p97 is Initiated through Multivalent Recognition of Catalytic and Regulatory Subunits by the p97 SEP-domain Adapters. *J Mol Biol*. 432, 6061–6074

34. Boom, J. van den, Kueck, A. F., Kravic, B., Müschenborn, H., Giesing, M., Pan, D., Kaschani, F., Kaiser, M., Musacchio, A., and Meyer, H. (2021) Targeted substrate loop insertion by VCP/p97 during PP1 complex disassembly. *Nat Struct Mol Biol*. 28, 964–971

35. Haines, D. S., Lee, J. E., Beauparlant, S. L., Kyle, D. B., Besten, W. den, Sweredoski, M. J., Graham, R. L. J., Hess, S., and Deshaies, R. J. (2012) Protein Interaction Profiling of the p97 Adaptor UBXD1 Points to a Role for the Complex in Modulating ERGIC-53 Trafficking*. *Mol Cell Proteomics*. 11, M111.016444

36. Trusch, F., Matena, A., Vuk, M., Koerver, L., Knævelsrud, H., Freemont, P. S., Meyer, H., and Bayer, P. (2015) The N-terminal Region of the Ubiquitin Regulatory X (UBX) Domain-containing Protein 1 (UBXD1) Modulates Interdomain Communication within the Valosin-containing Protein p97. *J Biol Chem*. 290, 29414–27

37. Schuetz, A. K., and Kay, L. E. (2016) A Dynamic molecular basis for malfunction in disease mutants of p97/VCP. *Elife*. 5, e20143

38. Huang, R., Ripstein, Z. A., Rubinstein, J. L., and Kay, L. E. (2018) Cooperative subunit dynamics modulate p97 function. *Proc National Acad Sci*. 116, 201815495

39. Kern, M., Fernandez-Sáiz, V., Schäfer, Z., and Buchberger, A. (2009) UBXD1 binds p97 through two independent binding sites. *Biochem Bioph Res Co*. 380, 303–307

40. Blueggel, M., Boom, J. van den, Meyer, H., Bayer, P., and Beuck, C. (2019) Structure of the PUB Domain from Ubiquitin Regulatory X Domain Protein 1 (UBXD1) and Its Interaction with the p97 AAA+ ATPase. *Biomol*. 9, 876

41. Hänzelmann, P., and Schindelin, H. (2011) The Structural and Functional Basis of the p97/Valosin-containing Protein (VCP)-interacting Motif (VIM) MUTUALLY EXCLUSIVE

BINDING OF COFACTORS TO THE N-TERMINAL DOMAIN OF p97*. *J Biol Chem*. 286, 38679–38690

42. Stapf, C., Cartwright, E., Bycroft, M., Hofmann, K., and Buchberger, A. (2011) The General Definition of the p97/Valosin-containing Protein (VCP)-interacting Motif (VIM) Delineates a New Family of p97 Cofactors*. *J Biol Chem*. 286, 38670–38678
43. Madsen, L., Andersen, K. M., Prag, S., Moos, T., Semple, C. A., Seeger, M., and Hartmann-Petersen, R. (2008) Ubxd1 is a novel co-factor of the human p97 ATPase. *Int J Biochem Cell Biology*. 40, 2927–2942
44. Jumper, J., Evans, R., Pritzel, A., Green, T., Figurnov, M., Ronneberger, O., Tunyasuvunakool, K., Bates, R., Žídek, A., Potapenko, A., Bridgland, A., Meyer, C., Kohl, S. A. A., Ballard, A. J., Cowie, A., Romera-Paredes, B., Nikolov, S., Jain, R., Adler, J., Back, T., Petersen, S., Reiman, D., Clancy, E., Zielinski, M., Steinegger, M., Pacholska, M., Berghammer, T., Bodenstein, S., Silver, D., Vinyals, O., Senior, A. W., Kavukcuoglu, K., Kohli, P., and Hassabis, D. (2021) Highly accurate protein structure prediction with AlphaFold. *Nature*. 596, 583–589
45. Varadi, M., Anyango, S., Deshpande, M., Nair, S., Natassia, C., Yordanova, G., Yuan, D., Stroe, O., Wood, G., Laydon, A., Žídek, A., Green, T., Tunyasuvunakool, K., Petersen, S., Jumper, J., Clancy, E., Green, R., Vora, A., Lutfi, M., Figurnov, M., Cowie, A., Hobbs, N., Kohli, P., Kleywegt, G., Birney, E., Hassabis, D., and Velankar, S. (2021) AlphaFold Protein Structure Database: massively expanding the structural coverage of protein-sequence space with high-accuracy models. *Nucleic Acids Res*. 50, D439–D444
46. Arumughan, A., Roske, Y., Barth, C., Forero, L. L., Bravo-Rodriguez, K., Redel, A., Kostova, S., McShane, E., Opitz, R., Faelber, K., Rau, K., Mielke, T., Daumke, O., Selbach, M., Sanchez-Garcia, E., Rocks, O., Panáková, D., Heinemann, U., and Wanker, E. E. (2016) Quantitative interaction mapping reveals an extended UBX domain in ASPL that disrupts functional p97 hexamers. *Nat Commun*. 7, 13047

47. Bulfer, S. L., Chou, T.-F., and Arkin, M. R. (2016) p97 Disease Mutations Modulate Nucleotide-Induced Conformation to Alter Protein–Protein Interactions. *Acs Chem Biol*. 11, 2112–2116

48. Blythe, E. E., Gates, S. N., Deshaies, R. J., and Martin, A. (2019) Multisystem Proteinopathy Mutations in VCP/p97 Increase NPLOC4·UFD1L Binding and Substrate Processing. *Structure*. 27, 1820-1829.e4

49. Shorter, J., and Southworth, D. R. (2019) Spiraling in Control: Structures and Mechanisms of the Hsp104 Disaggregase. *Csh Perspect Biol*. 11, a034033

50. Holm, L. (2020) Structural Bioinformatics, Methods and Protocols. *Methods Mol Biology*. 2112, 29–42

51. Orme, C. M., and Bogan, J. S. (2012) The Ubiquitin Regulatory X (UBX) Domain-containing Protein TUG Regulates the p97 ATPase and Resides at the Endoplasmic Reticulum-Golgi Intermediate Compartment*. *J Biol Chem*. 287, 6679–6692

52. Nagahama, M., Suzuki, M., Hamada, Y., Hatsuzawa, K., Tani, K., Yamamoto, A., and Tagaya, M. (2003) SVIP Is a Novel VCP/p97-interacting Protein Whose Expression Causes Cell Vacuolation. *Mol Biol Cell*. 14, 262–273

53. Ballar, P., Zhong, Y., Nagahama, M., Tagaya, M., Shen, Y., and Fang, S. (2007) Identification of SVIP as an Endogenous Inhibitor of Endoplasmic Reticulum-associated Degradation. *J Biol Chem*. 282, 33908–33914

54. Johnson, A. E., Orr, B. O., Fetter, R. D., Moughamian, A. J., Primeaux, L. A., Geier, E. G., Yokoyama, J. S., Miller, B. L., and Davis, G. W. (2021) SVIP is a molecular determinant of lysosomal dynamic stability, neurodegeneration and lifespan. *Nat Commun*. 12, 513

55. Chou, T.-F., Bulfer, S. L., Weihl, C. C., Li, K., Lis, L. G., Walters, M. A., Schoenen, F. J., Lin, H. J., Deshaies, R. J., and Arkin, M. R. (2014) Specific Inhibition of p97/VCP ATPase and Kinetic Analysis Demonstrate Interaction between D1 and D2 ATPase Domains. *J Mol Biol*. 426, 2886–2899

56. Schütz, A. K., Rennella, E., and Kay, L. E. (2017) Exploiting conformational plasticity in the AAA+ protein VCP/p97 to modify function. *Proc National Acad Sci*. 114, E6822–E6829

57. Wang, Q., Song, C., Yang, X., and Li, C.-C. H. (2003) D1 Ring Is Stable and Nucleotide-independent, whereas D2 Ring Undergoes Major Conformational Changes during the ATPase Cycle of p97-VCP*. *J Biol Chem*. 278, 32784–32793

58. Petrović, S., Roske, Y., Rami, B., Phan, M. H. Q., Panáková, D., and Heinemann, U. (2023) Structural remodeling of AAA+ ATPase p97 by adaptor protein ASPL facilitates posttranslational methylation by METTL21D. *Proc National Acad Sci*. 120, e2208941120

59. Buchberger, A., Howard, M. J., Proctor, M., and Bycroft, M. (2001) The UBX domain: a widespread ubiquitin-like module11Edited by P. E. Wright. *J Mol Biol*. 307, 17–24

60. Blythe, E. E., Olson, K. C., Chau, V., and Deshaies, R. J. (2017) Ubiquitin- and ATP-dependent unfoldase activity of P97/VCP•NPLOC4•UFD1L is enhanced by a mutation that causes multisystem proteinopathy. *Proc National Acad Sci*. 114, E4380–E4388

61. Mastronarde, D. N. (2005) Automated electron microscope tomography using robust prediction of specimen movements. *J Struct Biol*. 152, 36–51

62. Zheng, S. Q., Palovcak, E., Armache, J.-P., Verba, K. A., Cheng, Y., and Agard, D. A. (2017) MotionCor2: anisotropic correction of beam-induced motion for improved cryo-electron microscopy. *Nat Methods*. 14, 331–332

63. Punjani, A., Rubinstein, J. L., Fleet, D. J., and Brubaker, M. A. (2017) cryoSPARC: algorithms for rapid unsupervised cryo-EM structure determination. *Nat Methods*. 14, 290–296

64. Scheres, S. H. W. (2012) RELION: Implementation of a Bayesian approach to cryo-EM structure determination. *J Struct Biol*. 180, 519–530

65. Pettersen, E. F., Goddard, T. D., Huang, C. C., Couch, G. S., Greenblatt, D. M., Meng, E. C., and Ferrin, T. E. (2004) UCSF Chimera—A visualization system for exploratory research and analysis. *J Comput Chem*. 25, 1605–1612

66. Croll, T. I. (2018) ISOLDE: a physically realistic environment for model building into low-resolution electron-density maps. *Acta Crystallogr Sect D Struct Biology*. 74, 519–530

67. Pettersen, E. F., Goddard, T. D., Huang, C. C., Meng, E. C., Couch, G. S., Croll, T. I., Morris, J. H., and Ferrin, T. E. (2021) UCSF ChimeraX: Structure visualization for researchers, educators, and developers. *Protein Sci*. 30, 70–82

68. Emsley, P., Lohkamp, B., Scott, W. G., and Cowtan, K. (2010) Features and development of Coot. *Acta Crystallogr Sect D Biological Crystallogr*. 66, 486–501

69. Afonine, P. V., Poon, B. K., Read, R. J., Sobolev, O. V., Terwilliger, T. C., Urzhumtsev, A., and Adams, P. D. (2018) Real-space refinement in PHENIX for cryo-EM and crystallography. *Acta Crystallogr Sect D Struct Biology*. 74, 531–544

70. Madeira, F., Pearce, M., Tivey, A. R. N., Basutkar, P., Lee, J., Edbali, O., Madhusoodanan, N., Kolesnikov, A., and Lopez, R. (2022) Search and sequence analysis tools services from EMBL-EBI in 2022. *Nucleic Acids Res*. 50, W276–W279

Chapter 3

Asymmetric apical domain states of mitochondrial Hsp60 coordinate substrate engagement and chaperonin assembly

Contributing Authors:

Julian R. Braxton[1-4], Hao Shao[2,3], Eric Tse[2,4], Jason E. Gestwicki[2,3], and Daniel R. Southworth[2,4]

[1]Graduate Program in Chemistry and Chemical Biology; University of California, San Francisco; San Francisco, CA 94158, USA

[2]Institute for Neurodegenerative Diseases; University of California, San Francisco; San Francisco, CA 94158, USA

[3]Department of Pharmaceutical Chemistry; University of California, San Francisco; San Francisco, CA 94158, USA

[4]Department of Biochemistry and Biophysics; University of California, San Francisco; San Francisco, CA 94158, USA

Abstract

The mitochondrial chaperonin, mtHsp60, promotes the folding of newly imported and transiently misfolded proteins in the mitochondrial matrix, assisted by its co-chaperone mtHsp10. Despite its essential role in mitochondrial proteostasis, structural insights into how this chaperonin binds to clients and progresses through its ATP-dependent reaction cycle are not clear. Here, we determined cryo-electron microscopy (cryo-EM) structures of a hyperstable disease-associated mtHsp60 mutant, V72I, at three stages in this cycle. Unexpectedly, client density is identified in all states, revealing interactions with mtHsp60's apical domains and C-termini that coordinate client positioning in the folding chamber. We further identify a striking asymmetric arrangement of the apical domains in the ATP state, in which an alternating up/down configuration positions interaction surfaces for simultaneous recruitment of mtHsp10 and client retention. Client is then fully encapsulated in mtHsp60/mtHsp10, revealing prominent contacts at two discrete sites that potentially support maturation. These results identify a new role for the apical domains in coordinating client capture and progression through the cycle, and suggest a conserved mechanism of group I chaperonin function.

Introduction

Many proteins require the assistance of molecular chaperones to assume their native conformation(s) in the cell (1). Chaperonins are an essential and highly conserved class of molecular chaperones found in all domains of life that form distinct multimeric ring complexes featuring a central cavity in which client protein substrates are folded (2, 3). Chaperonins are classified into two groups: group I members, including bacterial GroEL, form heptameric rings and require a co-chaperonin (here GroES) to completely seal the folding chamber, while group II members, including human TRiC/CCT, form octa- or nonameric rings and have helical insertions that close the chamber (4). Both group I and II chaperonins play essential roles in protein

homeostasis (proteostasis), likely because their architecture allows them to act on a wide variety of important client proteins.

Much has been learned about the mechanisms of group I chaperonins through pioneering studies of GroEL/ES (5). Each GroEL promoter is composed of an apical domain, an intermediate domain, and an equatorial ATPase domain that coordinates inter-ring contacts to form the double-ring tetradecamer. In the intact heptamer, non-native client proteins bind tightly to exposed, inward-facing hydrophobic surfaces on GroEL apical domains, as well as to hydrophobic C-terminal tails found at the base of the folding cavity (6–9). ATP binding to the equatorial domains induces an upward rotation and elevation of the apical domains, resulting in a decreased affinity for client and an increased affinity for GroES (10–13). In this arrangement, GroES then binds the hydrophobic apical domain surfaces and seals the now-hydrophilic cavity, favoring the folding of the client protein (14–17). GroES dissociates in a post-hydrolysis state, enabling the client to be released in a folded, native state or partially folded intermediate that requires subsequent rounds of chaperone interaction (18). Through this mechanism, GroEL/ES promotes the folding of prokaryotic proteins and buffers cellular stress upon heat shock (19).

Mitochondrial heat shock protein 60 (mtHsp60) is the only group I chaperonin found in humans. Along with its co-chaperonin, mtHsp10, it promotes the folding of proteins newly imported into the mitochondrial matrix, as well as proteins that have become denatured upon thermal or chemical stress (20–22). This chaperonin has been implicated in the progression of several cancers (23, 24), and point mutations in mtHsp60 cause severe neurodegenerative diseases known as hereditary spastic paraplegias, which cause progressive muscle spasticity and lower limb weakness (25–29). Because of these links to disease, there is interest in understanding the structure and function of mtHsp60/mtHsp10, and in developing inhibitors as chemical probes or potential therapeutics (30–33).

Given the structural and sequence homology between mtHsp60 and GroEL, the general chaperone mechanisms are thought to be conserved (34). Indeed, client-free structures of mtHsp60 and mtHsp60/10 complexes confirm that several reaction intermediates in the chaperone cycle are shared, however there are important differences in ring-ring assembly and inter-ring allostery (35–38). Moreover, there are multiple gaps in our structural and mechanistic understanding of how mtHsp60/mtHsp10 binds and folds its clients during the ATP-dependent reaction cycle. Advances in understanding mtHsp60 mechanism have been limited by the relative instability of mtHsp60 complexes *in vitro* (39), likely explaining the lack of reported client-bound mtHsp60 structures. Thus, it is not clear which regions of mtHsp60 might be involved in these interactions or how clients might impact mtHsp60's structure. Additionally, in group I chaperonins client and co-chaperone appear to bind to the same region (8), namely the inward-facing hydrophobic apical domain helices H and I. It is therefore unclear how co-chaperonin binding occurs with a bound client given these overlapping interactions. A possible explanation comes from the observation that ATP binding decreases the affinity of GroEL for client: previous studies have suggested the existence of a series of ATP-bound intermediates in which chaperonin-client interactions are progressively weakened while chaperonin-co-chaperonin interactions are strengthened (13, 40–42). These states might feature sufficiently low client off-rates such that release is averted until co-chaperonin is bound. However, the structural details of such complexes remain elusive.

We sought to determine the structural basis for progression through the nucleotide- and mtHsp10-dependent mtHsp60 chaperone cycle using a disease-associated mutant that increases oligomeric stability (26, 28, 43). Cryo-EM structures of three mtHsp60 states in this cycle were determined: apo-mtHsp60, ATP-bound mtHsp60, and ATP-bound mtHsp60/mtHsp10. Unexpectedly, extensive sub-classification revealed low-resolution density corresponding to a bound client in the chamber for each state. The position of client density appears coordinated by

distinct sites of interaction that include the apical domains, equatorial domain stem loops, and disordered C-terminal tails. We identify a novel arrangement of ATP-bound mtHsp60 in which the apical domains alternate between a client-contacting 'down' conformation and an outward-facing 'up' conformation. The 'down' conformation allows contact with client but appears incompatible with mtHsp10 binding, while the 'up' conformation is disengaged with client but has accessible mtHsp10 binding sites. These results suggest a mechanism in which apical domain up/down positioning enables client retention within the folding cavity to occur simultaneously with mtHsp10 recruitment. The ATP-bound mtHsp60/mtHsp10 structure indicates that subsequent movement of the remaining apical domains completes the contact with all mtHsp10 protomers, sealing the chamber and allowing folding to progress. We propose that this mechanism may be conserved among group I chaperonins, including GroEL/ES, providing new insight into how these chaperone machines are able to retain clients during recruitment of their co-chaperonins.

Results

The hereditary spastic paraplegia variant mtHsp60^{V72I} forms stable heptamers and retains significant chaperone activity

Wild type mtHsp60 heptamers are unstable in the absence of mtHsp10 *in vitro*, and readily dissociate into monomers at low concentration or temperature, or when incubated with nucleotide (39), thereby complicating efforts to characterize the mtHsp60 chaperone cycle. To facilitate structural studies of mtHsp60, we focused on the previously identified mtHsp60^{V72I} variant that is associated with hereditary spastic paraplegia SPG13 (26, 29), and is reported to have increased oligomeric stability (43). Residue V72 (numbering corresponds to the mature mtHsp60 protein after cleavage of the mitochondrial import sequence) is located in the equatorial domain of mtHsp60 and packs into its hydrophobic core, but does not contact the ATP binding pocket (**Figure 3.1A** and **Figure 3.S1A**). Importantly, the V72I mutation retains some client refolding

activity *in vitro* (43), suggesting that general features of the mtHsp60 chaperone cycle are preserved.

To investigate the biochemical effects of the V72I mutation, we first confirmed the increased stability of this mutant using size exclusion chromatography coupled to multi-angle light scattering (SEC-MALS). This experiment revealed that the V72I mutant mostly remained as heptamers, while wild-type protein had almost completely dissociated into monomers (**Figure 3.1B**). Importantly, incubation with ATP caused the complete dissociation of wild-type protein, while an appreciable fraction remained oligomeric with the V72I mutation. Next, we analyzed the ATPase activity of the V72I mutant *in vitro*. In the absence of mtHsp10, an increase in nucleotide hydrolysis rate (~10 pmol ATP hydrolyzed/min for WT, ~21 for V72I) was observed (**Figure 3.S1B**), which is likely a result of the V72I protein's enhanced oligomerization (see **Figure 3.1B**) and the known effect of cooperative ATP hydrolysis (44, 45). To determine if mtHsp10 could further increase ATPase activity, we titrated with increasing concentrations of mtHsp10 and found that it stimulated hydrolysis in both WT and V72I, although the activity in WT was higher than in V72I at high mtHsp10 concentrations (~37 pmol/min for WT, ~31 for V72I at the highest concentration tested). Overall, we conclude that the V72I mutation only modestly impacts ATP hydrolysis. Next, to investigate client folding activity, we measured substrate turnover by chemically denatured mitochondrial malate dehydrogenase (mtMDH) after incubation with the mtHsp60/10 system using an established assay (46). We identify that the V72I mutation impairs, but does not eliminate, client refolding activity (initial velocity of mtMDH activity ~0.03 for WT, ~0.02 for V72I) (**Figure 3.1C**), indicating this mutant retains a significant amount of chaperone activity *in vitro*. In sum, based on the modest biochemical effects that we and others identify, we considered this mutation to be an attractive tool with which to structurally characterize the chaperone states of mtHsp60.

Structures of mtHsp60^{V72I} heptamers reveal asymmetric apical domain conformations that coordinate a bound client

We first sought to determine cryo-EM structures of the nucleotide-free (apo) mtHsp60^{V72I} heptamer. Reference-free two-dimensional (2D) class averages of the complex show top views with clear heptameric rings and apparent C7 symmetry and side views with two bands of density likely corresponding to the equatorial and apical domains (**Figure 3.1D** and **Figure 3.S1C**). Remarkably, in certain top view class averages an additional asymmetric density in the central cavity is observed that we hypothesized to be a bound protein client (**Figure 3.1D**). Initial three-dimensional (3D) classification of mtHsp60^{apo} particles reveal four prevalent classes (classes 1-4) corresponding to mtHsp60 heptamers. Classes 2 and 4 feature density in the mtHsp60 central cavity, consistent with the top-view 2D averages (**Figure 3.S1D** and **Figure 3.1D**). In total, ~39% of the particles selected from 3D classification contain this density. Given that mtHsp60 heptamers are reconstituted from purified monomers and no additional protein was carried through the purification (**Figure 3.S1E**), we conclude the extra density is likely partially folded mtHsp60 that is retained as a client in the chamber. Indeed, mtHsp60 is required for its own assembly into oligomeric complexes in yeast mitochondria (47). This serendipitous observation indicates that the increased oligomer stability and slowed client folding activity of V72I are features that combine to favor the capture of structures with bound client, making the mtHsp60^{V72I} system poised to reveal the structural basis of mtHsp60 chaperone function.

Given the structural similarities between all mtHsp60 classes, we jointly refined particles from all four classes with C7 symmetry enforced in order to improve resolution. This resulted in a consensus map at 3.4 Å resolution, which enabled building of an atomic model (**Figure 3.1E**, **Figure 3.S2A**, and **Table 3.1**). All domains of mtHsp60 were modeled except the flexible C-terminal tails, which were not resolved. This model highly resembles structures of previously published mtHsp60 heptamers (Cα root mean squared deviation (RMSD) ~0.6-0.8 Å) (35, 38).

While the equatorial and intermediate domains are well-resolved in this map, density for the apical domains, including the cavity-facing helices H and I, is considerably weaker, indicating flexibility (**Figure 3.1F**). This is also reflected in the higher *B*-factors relative to the equatorial and intermediate domains (**Figure 3.S1F**). Additional density in the central cavity is only observed at very low thresholds, likely due to its heterogeneity and symmetry imposed during refinement. From this analysis, we wondered whether the weaker apical domain density was a result of independent apical domain motions of each protomer, or whether a series of discrete heptameric arrangements of these domains existed, possibly related to client binding.

To better resolve the apical domains and potential client contacts we sorted mtHsp60 particles solely by apical domain conformation and client density, excluding signal from the relatively invariant equatorial and intermediate domains. Given the C7 symmetry of the mtHsp60 heptamer, this was achieved by focused classification using symmetry-expanded (48) particles in order to resolve symmetry-breaking conformations of apical domains (**Figure 3.1G**). This approach, and subsequent refinement of the entire volumes, resulted in two types of classes: those with dramatically improved apical domain density, and those with strong density corresponding to client (**Figure 3.S1D** and **Figure 3.S2B**). The absence of strong client density in classes with well-resolved apical domains is likely due to apical domain signal driving the classification, rather than client. Inspection of the best class with improved apical domain density, termed mtHsp60^{apo} focus, revealed a range of apical domain conformations around the heptamer, each related by a rigid body rotation about the apical-intermediate domain hinge (**Figure 3.1H,I**). Relative to the consensus map, apical domains rotate both upward (i.e. away from the equatorial domain) and downward; the range of rotation among all protomers spans ~10° (**Figure 3.1H,I** and **Figure 3.S1G**). Intriguingly, some of the largest differences in apical domain position occur in adjacent protomers, giving rise to an apparent ‘up’ and ‘down’ alternating conformation (**Figure 3.1H**, protomers 7 through 3). In sum, we successfully resolved the flexible mtHsp60^{apo} apical

domains and identify that they adopt discrete up/down positions around the heptamer, rather than being randomly oriented.

Client-containing maps from focused classification feature client at multiple locations in the mtHsp60 heptamer (**Figure 3.1J** and **Figure 3.S1D**). Density corresponding to client is at an overall low resolution compared to the mtHsp60 protomers, but this result is expected for a partially folded protein that likely populates multiple conformations; low-resolution client density has also been observed in GroEL structures (8, 9, 14, 49). In all structures, client is asymmetrically positioned in the central cavity and contacts multiple mtHsp60 protomers, which is consistent with the finding that group I chaperonins use multiple apical domains to engage client, and with previous observations of asymmetric client density in GroEL tetradecamers (7–9). However, there are notable differences in client localization between the three classes, with density positioned adjacent to the mtHsp60 apical domain, equatorial domain, or both. In the apical-only class client density is proximal to helices H and I (**Figure 3.S1I**), which contain multiple hydrophobic residues shown to be critical for the binding of non-native proteins to GroEL (6), and also form the surface engaged by mtHsp10 (36, 37). Likewise, in the equatorial-only class client density is located deeper in the central cavity and appears to interact with the disordered C-terminal tails that project into this cavity (**Figure 3.S1J**), and in the apical/equatorial class both contacts are observed. Notably, all client-bound classes also feature asymmetric apical domain conformations (**Figure 3.S1H**), indicating that apical flexibility is a general feature of mtHsp60^{apo} and not limited to either client-bound or -unbound complexes.

ATP binding induces mtHsp60 double-ring formation and ordered apical domain conformations

We next sought to characterize apical domain conformations and client positioning in the uncapped, ATP-bound state. ATP binding favors the formation of double-ring tetradecamers (50), and reference-free 2D class averages of this sample indeed revealed a double-ring arrangement for the majority of particles, though top views of single rings were also observed (**Figure 3.S3A**).

All top view averages show clear density corresponding to client, in contrast to the weaker density in apo state particles, potentially indicating higher client occupancy in the ATP sample (**Figure 3.S3A** and **Figure 3.S1C**). Side view class averages show markedly decreased apical domain resolution relative to that of the equatorial and intermediate domains (**Figure 3.2A**). Based on symmetric features of the complex identified in 2D analysis and the lack of negative inter-ring cooperativity with respect to nucleotide binding in this system (50), we refined the structure of the double-ring complex with D7 symmetry enforced (**Figure 3.2B** and **Figure 3.S3B**). The resulting map has an overall resolution of 2.5 Å, with the highest resolution in the equatorial and intermediate domains and greatly reduced resolution for the apical domains due to their extended, flexible arrangement (**Figure 3.S2C** and **Table 3.1**). This finding is similar to the apo state, and indicates the equatorial and intermediate domains are conformationally invariant, while the apical domains are substantially more flexible in the uncapped, ATP state. Client appears as a diffuse central density at approximately the level of the apical domains, and is likely less visible due to the imposition of symmetry. We built a complete atomic model of this structure by fitting in a previous model of mtHsp60 and rigid body docking the apical domain into the low-resolution density, followed by all-atom refinement (**Figure 3.S3C**). ATP is clearly resolved in the nucleotide-binding pocket, indicating that this structure corresponds to a pre-hydrolysis state (**Figure 3.S3D**). As observed in other chaperonins, nucleotide binding induces a downward ~20° rigid body rotation of the intermediate domain over the equatorial nucleotide-binding pocket, positioning the catalytic aspartate (D397) in proximity to the ATP γ-phosphate (**Figure 3.S3E**). The inter-ring interface closely matches that of other nucleotide-bound mtHsp60 cryo-EM structures, with protomers arranged in a staggered 1:2 conformation and presenting two possible sites of interaction to the opposite ring (37). At the first site, residues in helix P form polar and hydrophobic interactions between rings, while no contacts are observed at the other site (**Figure 3.S3F**). The mtHsp60 inter-ring interface is significantly reduced compared to those in analogous GroEL complexes (10, 11, 51), likely explaining the ability of mtHsp60 to exist as single rings.

We postulated that the apical domains in the ATP state may be similarly positioned as we identify in the apo state, adopting discrete up/down arrangements around the heptamer that are potentially correlated with client contact. To investigate this possibility, we performed focused classification of D7 symmetry expanded particles, using a mask that encompassed all apical domains of one heptamer, and the central cavity (**Figure 3.2C** and **Figure 3.S3B**). Out of 50 classes, ten have greatly improved apical domain density for several protomers; the number of protomers per heptamer with improved density varies between three and six. Intriguingly, similar to the apo state, we identify an up/down arrangement in all apical domains with improved resolution. Four of the ten classes (classes 1-4) have six well-resolved apical domains in this pattern, and the symmetry-breaking protomer (i.e. the protomer between an up and down protomer) exhibits much weaker density, likely due to an inability to stably adopt either conformation.

Refinement of the best focused class with six well-resolved apical domains (class 1, determined qualitatively) using a mask around the entire heptamer yielded the mtHsp60^{ATP} focus map (**Figure 3.2D**, **Figure 3.S2D**, and **Table 3.1**). This structure features substantially improved density for six apical domains, while that of the symmetry-breaking protomer remained more poorly resolved. Additionally, the equatorial and intermediate domains adopt identical conformations as in the consensus structure, but two states of the apical domains, termed the 'up' and 'down' states, are observed in an alternating arrangement around the heptamer (**Figure 3.2E**). With the improved apical domain resolution we identify that the up/down conformations are related by a rigid body rotation of ~25°. The rotation of the 'up' apical domains displaces helices H and I from the central cavity; this likely eliminates potential client binding to these helices. In contrast, the rotation of the 'down' apical domains enables helices H and I to project directly into the central cavity. Apical inter-protomer contacts between 'up' and 'down' protomers are predominantly made using helices H and I, though the resolution is insufficient to identify specific

interacting residues (**Figure 3.S3G**). Finally, modeling suggests that two adjacent 'up' protomers would not significantly clash with each other but that two adjacent 'down' protomers would (**Figure 3.S3H**). Given that adjacent 'up' protomers were not observed during focused classification it therefore appears that the alternating up/down arrangement is critical for stable apical domain positioning.

In addition to substantially improved apical domain density, the mtHsp60^{ATP} focus map features asymmetric client density in the mtHsp60 central cavity (**Figure 3.2D**). As in mtHsp60^{apo} structures, client is contacted by the apical and equatorial domains (**Figure 3.2F-H**). Apical contacts are only made by 'down' protomers; this pattern of contact results in an asymmetric positioning in the mtHsp60 cavity (**Figure 3.2D**). Based on our molecular model, these interactions primarily involve helix I and the underlying hydrophobic segment (**Figure 3.2G**). The C-terminal tails and equatorial stem loop (residue W42) also contact client, and, as in mtHsp60^{apo}, likely serve to retain client in the folding cavity (**Figure 3.2H**). This arrangement is distinct from the client densities identified in the apo state, likely due to the rotation of all apical domains relative to those in apo states. In sum, ATP binding induces a highly persistent alternating conformational arrangement of mtHsp60 apical domains, which is identified in all classes with well-resolved apical domains. This appears to cause a functional asymmetry in client binding ability and potentially enables bifunctional interactions by apical domains.

mtHsp10 binding symmetrizes mtHsp60 complexes and exposes distinct client-contacting surfaces

We next sought to determine structures of the mtHsp60-mtHsp10 complex in order to investigate the active state for promoting client folding. To accomplish this, we incubated these proteins with saturating ATP and prepared samples for cryo-EM as before. Reference-free 2D class averages revealed predominantly symmetric double-ring complexes (hereafter referred to as 'footballs' due to their resemblance to an American football), with a heptamer of mtHsp10 capping each mtHsp60

heptamer (**Figure 3.S4A,B**). The structure of the football complex with D7 symmetry imposed refined to a resolution of 2.7 Å, with well-resolved density for mtHsp10 and all domains of mtHsp60, excluding the mtHsp60 C-terminal tails (**Figure 3.3A**, **Figure 3.S2E**, and **Table 3.1**). In contrast to the apo and ATP consensus structures, the apical domains in this state are approximately as well-resolved as the equatorial and intermediate domains. Client is only observed in this consensus map at very low thresholds, likely due to partial occupancy in the central cavities of double-ring complexes and well-resolved density for mtHsp60 and mtHsp10, which could overwhelm density for client. However, based on previous structures we hypothesized that a subset of particles might contain stronger client density.

To analyze the mtHsp10-bound state further, we built an atomic model of the football complex (**Figure 3.S4C**). ATP is well resolved in the nucleotide-binding pocket, and adopts the same orientation as in ATP-bound mtHsp60 (**Figure 3.3B**). Likewise, the conformations of the equatorial and intermediate domains are nearly identical to those in the ATP-bound state (**Figure 3.S4D**). Relative to the 'up' apical domains in mtHsp60^{ATP}, the apical domains undergo a ~65° clockwise twist and elevation, generating a near-planar surface formed by helices H and I onto which mtHsp10 docks. mtHsp10 predominantly interacts with these helices through a hydrophobic triad (I31, M32, L33) in its mobile loop (**Figure 3.S4E**). The interior of the composite mtHsp60/10 folding cavity features increased hydrophilicity relative to the interior of apo-mtHsp60 (**Figure 3.S4F**), also a feature of GroEL/ES complexes (52). Finally, the inter-ring interface of this complex very closely resembles that of uncapped mtHsp60^{ATP} (**Figure 3.S4G**).

To visualize client in football complexes, we performed focused classification using a mask that included the folding cavity, with minimal density corresponding to mtHsp60 and mtHsp10 (**Figure 3.3C** and **Figure 3.S4B**). This approach resulted in a class with significant client density, which refined to 3.4 Å when using a mask encompassing the entire mtHsp60/mtHsp10 ring (**Figure 3.3D**). The bulk of the client density presents as a toroidal ring approximately at the level

of the mtHsp60 apical domains (**Figure 3.3D**). mtHsp60-client contacts become apparent when inspecting lowpass-filtered versions of the client density, which reveal that in multiple mtHsp60 protomers, client contacts the interface of two alpha-helical hairpins, which project two aromatic residues (F279, Y359) into the folding cavity (**Figure 3.3E,F**). These residues are only exposed to the central cavity in the mtHsp10-bound state (**Figure 3.S4D**). Contiguous density corresponding to client and the mtHsp60 C-terminal tails is also visible in filtered maps, suggesting that these extensions play a role during client folding (**Figure 3.3G**). Overall, client localization and mtHsp60 contacts in this state resembles those in the mtHsp60^{ATP} focus map and in client-bound GroEL/ES complexes (14, 49), with both apical and equatorial domains in contact with client. This arrangement is distinct from the mtHsp60^{apo} state, which features several client topologies, including apical-only and equatorial-only contacts, indicating a more heterogeneous association with mtHsp60^{apo} heptamers. Of note, multiple distinct conformations in the mtHsp10-bound complex might exist, though the likely heterogeneous client population and sub-stoichiometric occupancy likely precludes the identification of distinct, or folded, conformations.

Client-contacting mtHsp60 residues are also important for oligomerization

To probe the role of specific regions of mtHsp60 in client refolding activity, we selected four aromatic residues observed to contact client and mutated them to Ala (**Figure 3.4A**). W42 is located on the equatorial domain stem loop, which is positionally invariant in all mtHsp60 states. Y201 is located in the underlying segment of the apical domains, and was observed to contact client in the ATP state. F279 and Y359 contact client in the mtHsp10-bound state due to a significant rotation of the apical domain (**Figure 3.S4D**); they do not face the folding chamber in the apo or ATP-bound states. Conservation analysis between human mtHsp60 and its yeast and bacterial orthologs revealed that three of these residues are conserved, while W42 is a Phe in the other sequences (**Figure 3.4B**). Analysis of ATPase activity in these mutants revealed that the activity of three of the four, W42A, F279A, and Y359A, was not stimulated by mtHsp10 (**Figure**

3.4C). The activity of the Y201A mutant was modestly impaired at high concentrations of mtHsp10, reminiscent of V72I (**Figure 3.S1B**). Furthermore, all four mutants had impaired mtMDH refolding activity compared to WT (**Figure 3.4D**), a finding possibly explained by the perturbed ATPase activity. Given the lack of mtHsp10-stimulated ATPase activity in three of four mutants, we next wondered whether these mutations had altered oligomerization propensities. Indeed, when analyzing these samples by SEC we observed that the W42A, F279A, and Y359A mutants had completely dissociated into monomers, whereas WT and Y201A were at least partly heptameric (**Figure 3.4E**). Inspection of the apo mtHsp60 model revealed that F279 and Y359 are at an inter-protomer interface, and appear to contact the neighboring intermediate domain (**Figure 3.4F**). Thus, mutation of these two residues potentially impairs this interaction, leading to a less stable heptamer. However, the mechanism of monomerization induced by the W42A mutation, which is not proximal to any inter-protomer interface, is less clear. Together, we conclude that client binding and oligomer assembly are somewhat coupled in the mtHsp60 system, making it difficult to assign distinct roles to these residues.

A model of mtHsp60 client engagement and progression through the chaperone cycle

The results presented here allow for the generation of a model describing client folding by the mtHsp60-mtHsp10 system (**Figure 3.5** and **Movie 3.1**). In this model, mtHsp60 without nucleotide or co-chaperone exists as heptamers that are competent to bind client, with static equatorial and intermediate domains and somewhat flexible apical domains loosely arranged in alternating up/down conformations. The client folding chamber in the apo state allows for multiple mtHsp60 interaction modes, including interaction with the inward surface of the apical domains, the disordered C-terminal tails, or both. ATP binding induces the dimerization of heptamers at the equatorial-equatorial interface, causes a downward rotation of the intermediate domain, closing the nucleotide binding pocket, and causes apical domain rotation. The apical domains of ATP-bound protomers are arranged in a strict up/down alternating arrangement, with the ‘down’

protomers interacting with client through helix I and the underlying hydrophobic segment. Equatorial interactions, namely with the C-terminal tail and an aromatic residue projecting into the folding chamber, also contribute to client interaction. The ‘up’ ATP-bound protomers likely provide an initial platform for mtHsp10 association, and interaction with the remaining apical domains induces the transition into a fully symmetric conformation that expands the now-capped folding chamber, allowing the client to fold. Finally, upon ATP hydrolysis mtHsp10 dissociates from the heptamer, and client is released.

Discussion

Chaperonins are a superfamily of molecular chaperones that promote protein folding by encapsulating unfolded or misfolded client proteins and allowing them to fold in a protected environment. How client and co-chaperonin binding are coordinated to enable efficient client folding in group I chaperonins, including the bacterial GroEL/ES and mitochondrial Hsp60/10 systems, has remained an active area of study. The mtHsp60/10 system is a relatively understudied chaperonin homolog, yet has critical roles in human health and disease. Here we used the stabilizing V72I mutant to structurally characterize intermediates in the mtHsp60 chaperone cycle, all of which unexpectedly contained client. These investigations substantially increase our understanding of the mechanism of group I chaperonins.

In the apo state we identify that client contacts multiple mtHsp60 protomers in several dynamic arrangements (**Figure 3.1J** and **Figure 3.S1I,J**), an observation consistent with previous reports of multiple apical domains being necessary for efficient client binding in GroEL (7). Intriguingly, though a preference for contact with contiguous protomers has been observed for some clients, this does not appear to be the case upon ATP binding in the mtHsp60 system, as apical domains of alternating protomers were observed to contact client (**Figure 3.2F**). Therefore, client interactions with chaperonins appear to change throughout the chaperone cycle.

Based on our structures we propose that apical domain asymmetry is a key feature of the mtHsp60 cycle because it enables efficient client capture and retention. The mtHsp60 apo state may be initially encountered by client and features moderate apical domain flexibility, in agreement with other studies of mtHsp60 and its homologs (35, 38, 53). We identify that apical domains in intact heptamers exhibit loosely enforced alternating arrangements of 'up' and 'down' apical domains, rather than being randomly distributed (**Figure 3.1H,I**). These arrangements do not appear to be induced by client binding, as classes without resolved client that exhibit these patterns were identified (**Figure 3.1I**). It is therefore possible that these arrangements are simply more energetically favorable than in a perfectly symmetric apical domain ring, perhaps due to steric constraints. Intriguingly, similar apical domain arrangements are observed in ATP-bound structures, though the degree of asymmetry is greater and the up/down pattern is consistently observed across the different classes (**Figure 3.2F** and **Figure 3.S3B**). The positioning in the apo state likely predisposes the apical domains for the alternating arrangement we observed in the ATP-bound state. Moreover, the ATP dependence in mtHsp10 binding may be a consequence of increased stability of the upward-positioned apical domains to facilitate binding. Notably, these results are in contrast to previous assumptions of symmetric intermediates in the group I chaperonin cycle (10).

The alternating apical domain arrangement in the ATP-bound mtHsp60 state raises a question about the role of the 7th protomer, located at the interface of 'up' and 'down' apical domains. The apical domain of this protomer appears highly flexible, likely due to an inability to adopt either ordered conformation, though two adjacent 'up 'protomers appear permitted (**Figure 3.S3H**) and are likely not observed due to the need for the stabilizing up/down packing arrangement. Several possibilities exist as to the function of the 7th protomer: first, it might play a role in co-chaperonin recruitment, enabling significantly greater access to helices H and I and thus more efficient binding than even that facilitated by the three 'up' apical domains, which are

still somewhat inward-facing (**Figure 3.2D**). Alternatively, it may be largely non-functional, and the presence of the 7th protomer may merely serve to enlarge the size of the chaperonin folding chamber, enabling encapsulation of larger clients. A final possibility is that this symmetry-breaking protomer might confer a measure of stochasticity and dynamics in apical domain conformation, possibly weakening the alternating ATP-bound arrangement, which could enable efficient progression through the chaperone cycle. However, the evolution of octameric group II chaperonins, despite having a distinct conformational cycle (54), indicates that chaperonins with even numbers of protomers can be functional.

How client proteins are retained in the folding chamber during co-chaperonin binding has remained an open question for all group I chaperonins. Here, the alternating apical domain arrangements observed in the ATP-bound states raise exciting hypotheses about how this objective is achieved. We speculate that the function of the 'up' apical domains is to enable efficient recruitment of co-chaperonin, while the function of those in the 'down' conformation is to interact with client. This alternating arrangement would enable simultaneous client retention and co-chaperonin recruitment, likely preventing premature client release into solution during co-chaperonin association. The three 'up' apical domains provide a platform for initial co-chaperonin association (**Figure 3.5**, green apical surfaces), and conformational rearrangements cooperatively propagated throughout the entire heptamer result in apical domain rotations in all protomers and the formation of the fully-encapsulated complex. This model is consistent with previous biochemical studies of group I chaperonins, which suggested multiple ATP- and co-chaperonin-bound intermediates on the pathway to complete encapsulation (13, 41). The structures presented here are the first high-resolution views of an ATP-bound group I chaperonin without co-chaperonin, leaving unclear whether other homologs such as GroEL function by the same mechanism. However, given the high sequence similarity between members of the chaperonin superfamily (**Figure 3.S5**), it appears likely that the mechanism is conserved. Of note,

apical domains of apo GroEL exhibit considerably less flexibility than those in mtHsp60 and have distinct inter-protomer interfaces (38), suggesting that a different mechanism may be operative. The up/down apical domain configuration in ATP-bound protomers might also provide an explanation of chaperonin-promoted folding without encapsulation observed in GroEL (55, 56): the significant apical domain rotations relative to apo states may perform mechanical work on clients, displacing them from the walls of the central chamber and promoting folding without the need for the unique folding environment formed in the intact chaperonin-co-chaperonin complex.

The oligomer disruption observed for several tested mtHsp60 mutants is striking, and further confirms that mtHsp60 complexes are more labile than GroEL, which exists exclusively as oligomers. Though it is presumed that equatorial contacts are largely responsible for oligomeric stability in chaperonins (57), it appears that mutation of single equatorial and apical domain residues in mtHsp60 is sufficient to impair oligomeric stability. Indeed, the causative mutation of the hereditary spastic paraplegia MitCHAP-60 (27), D3G, is characterized by a marked decrease in oligomeric stability and thus chaperonin function (58), further supporting this instability as a unique aspect of mtHsp60 function.

The function of single- vs double-ring states of group I chaperonins during their chaperone cycles has been debated extensively (37, 59–61). In contrast to GroEL, apo mtHsp60 exists as single-ring heptamers, and in all other visualized states single-ring complexes are also observed (**Figure 3.1**, **Figure 3.S3A**, and **Figure 3.S4B**). A previously reported lack of inter-ring allostery also suggests that single rings are functional (62), and it is thus tempting to speculate that double-ring complexes are artefacts of the high protein concentrations employed *in vitro*. Indeed, engineered single-ring variants of mtHsp60 have been demonstrated to support client folding *in vitro*, strengthening this notion (37). However, lack of direct high-resolution observation of mtHsp60 complexes *in situ* leaves this question unresolved. In sum, this work provides a

comprehensive view of the structural intermediates of mtHsp60 complexes, the conclusions from which are potentially applicable to all group I chaperonins.

Figures

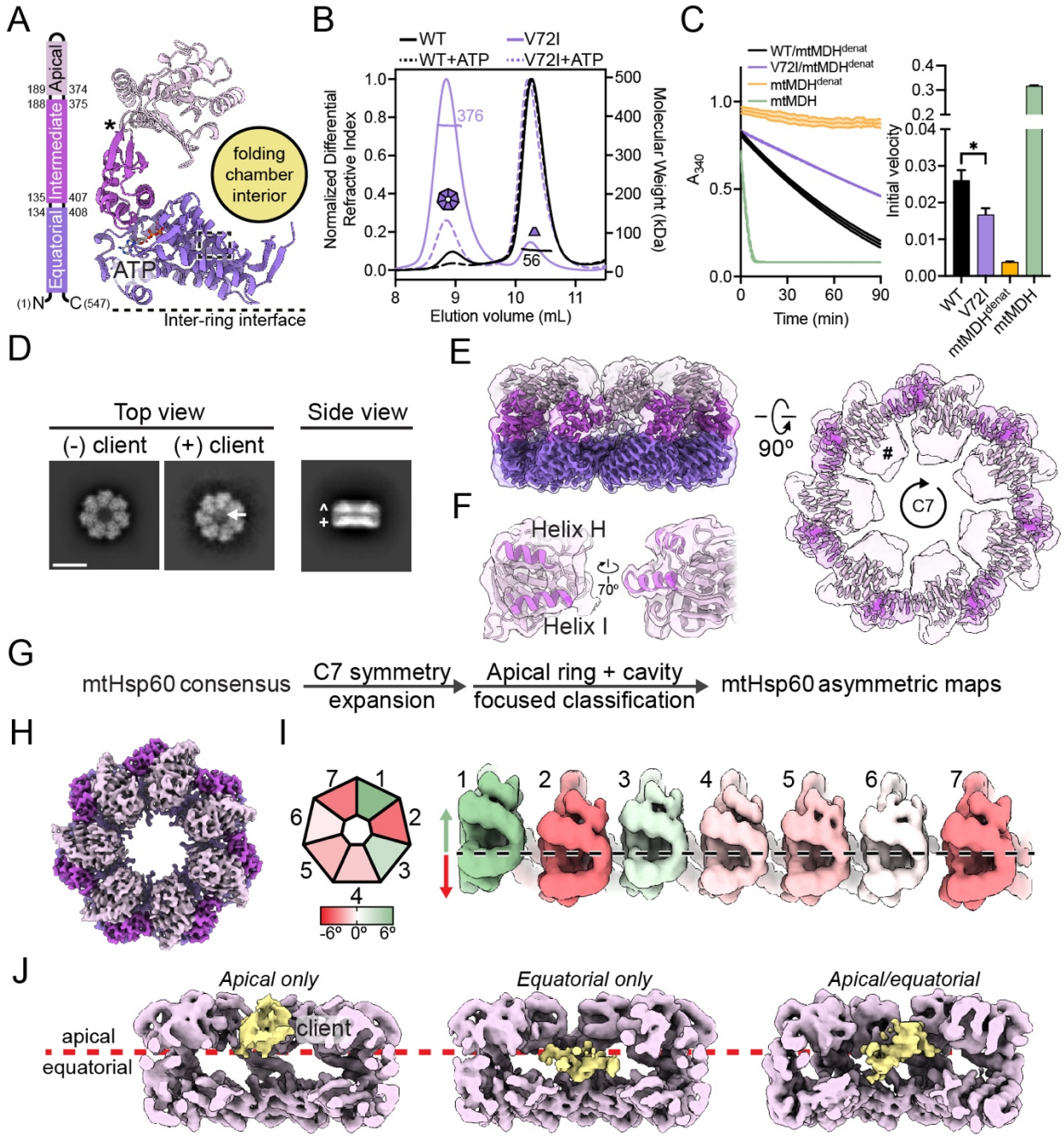

Figure 3.1 Biochemical and structural analysis of the mtHsp60^{V72I} mutant
(**A**) Domain schematic and cartoon of an mtHsp60 protomer (ATP-bound consensus model). Location of the V72I mutation is indicated by a box, and the apical-intermediate domain hinge is marked (*). (**B**) SEC-MALS of mtHsp60 (black) and mtHsp60^{V72I} (purple) without ATP (solid lines) and with ATP (dashed lines). Normalized differential refractive index (left y-axis) vs elution volume (x-axis) are shown. The average molecular weight of the heptamer peak of mtHsp60^{V72I} and the monomer peak of mtHsp60 are shown and indicated by horizontal lines (kDa, right y-axis). (**C**) Enzymatic activity of chemically-denatured human mtMDH refolded by the mtHsp60-mtHsp10 system, as measured by the decrease in NADH (an mtMDH cofactor) absorbance at 340 nm (left panel, representative of three biological replicates). Dashed lines represent standard deviation of technical triplicates. Initial velocities of absorbance curves from three biological replicates are shown at right. Error bars represent standard error of the mean. *$p < 0.05$. Wild-type mtHsp60 (black) refolds mtMDH more efficiently than does V72I (purple). Native (green) and denatured mtMDH (mtMDH^{denat}) (orange) are shown for comparison. (**D**) Top and side view 2D class averages of client-bound and -unbound mtHsp60^{V72I} heptamers. Client is indicated with a white arrow. Equatorial (+) and apical (^) domains are indicated in the side view average. Scale bar equals 100 Å. (**E**) Overlay of the sharpened (opaque) and unsharpened (transparent) mtHsp60^{apo} consensus map, colored as in (B), showing high-resolution equatorial and intermediate domains and weak apical domain density. Lack of apical domain density in the sharpened map is indicated in the top view (#). (**F**) Detailed view of an apical domain from mtHsp60^{apo} consensus, with the sharpened map (opaque) overlaid with the unsharpened map (transparent) and the fitted model. Helices H and I (dark purple) are particularly poorly resolved, indicating flexibility. (**G**) Cryo-EM processing workflow to obtain maps with client and asymmetric apical domain conformations. (**H**) Top view of the sharpened mtHsp60^{apo} focus map, showing significantly improved apical domain features, colored as in (B). (**I**) (Left) heptamer cartoon showing apical domain rotation relative to the consensus map. Positive values (green) indicate an upward rotation (increasing equatorial-apical distance), negative values (red) indicate a downward rotation. (Right) unwrapped view of the apical domains of the unsharpened mtHsp60^{apo} focus map, showing significant asymmetry in apical domain conformations, labeled as in (H), colored as in the cartoon. Dashed line indicates the apical domain position in the consensus map. (**J**) Slabbed side views of unsharpened additional refinements from the classification outlined in (G), showing unannotated density likely corresponding to client (yellow) present in multiple conformations in the mtHsp60 heptamer (purple). A dashed line (red) delimits apical and equatorial regions of mtHsp60.

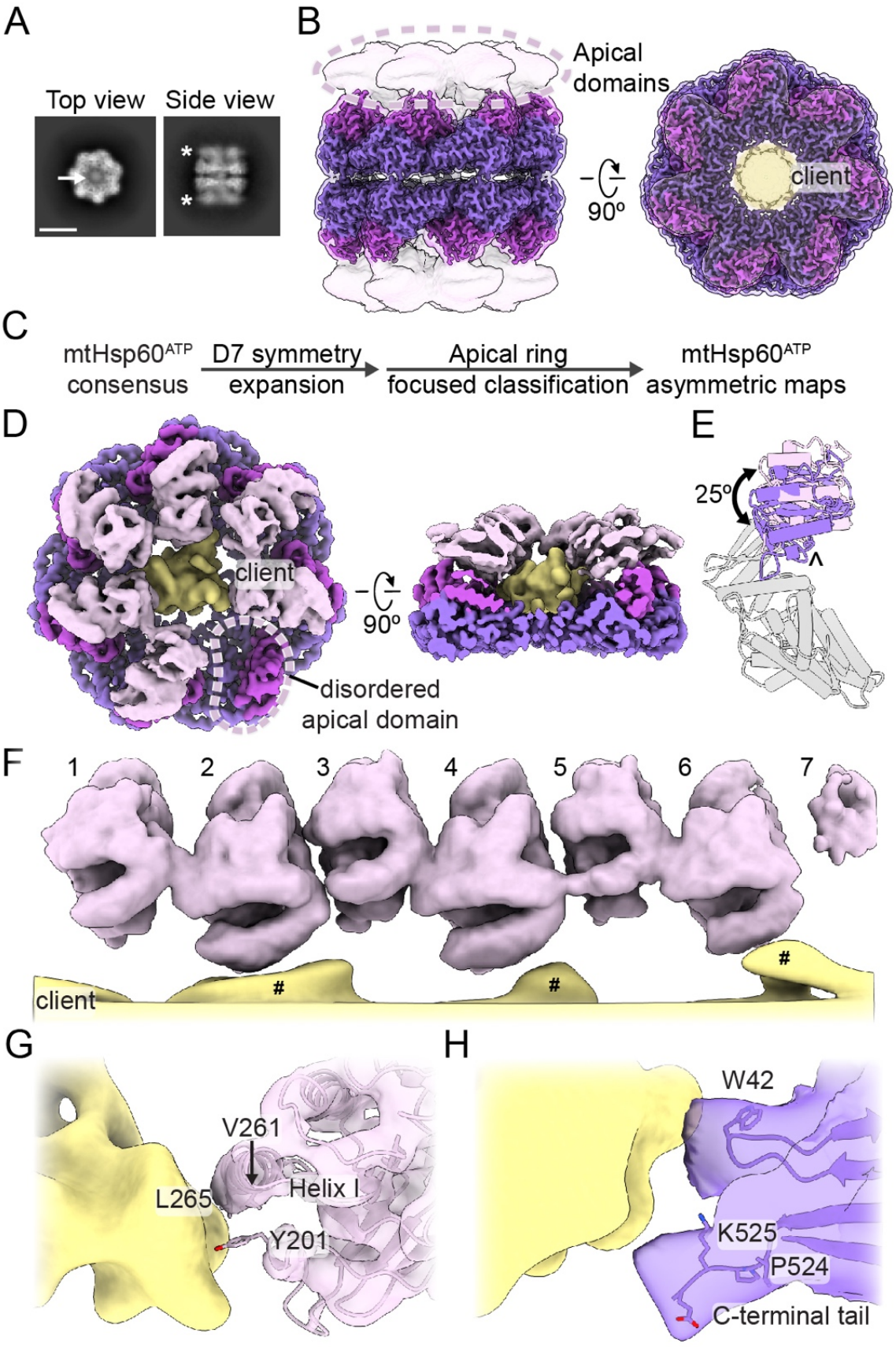
A
Top view
Side view
B
Apical domains
client
90º
C
mtHsp60ATP consensus
D7 symmetry expansion
Apical ring focused classification
mtHsp60ATP asymmetric maps
D
client
90º
disordered apical domain
E
25º
F
1
2
3
4
5
6
7
client
G
V261
L265
Helix I
Y201
H
W42
K525
P524
C-terminal tail

Figure 3.2 ATP-induced mtHsp60^{V72I} conformational changes and client contacts
(**A**) Top and side view 2D class averages of ATP-bound mtHsp60^{V72I}. Arrow in top view indicates client density in folding cavity; asterisks in side view indicate poor apical domain resolution as compared to the equatorial and intermediate domains. Scale bar equals 100 Å. (**B**) Sharpened (opaque) and unsharpened (transparent) maps of consensus ATP-bound mtHsp60^{V72I}, colored as in **Figure 3.1**. Note complete loss of apical domain density (encircled) in sharpened map. The central density corresponding to client is colored yellow in the top view. (**C**) Cryo-EM processing workflow to obtain maps with asymmetric apical domain conformations. (**D**) mtHsp60^{ATP} focus map, shown as unsharpened mtHsp60 density overlaid with segmented and 8 Å low-pass filtered client density. Note lack of density for one apical domain (encircled). (**E**) Models for representative 'up' (pink apical domain) and 'down' (purple apical domain) protomers, showing a rigid body rotation of the apical domain. Equatorial and intermediate domains are colored gray. The apical domain underlying segment (below helices H and I) is indicated (^). (**F**) Unwrapped view of the apical domains and client in the mtHsp60^{ATP} focus map, showing alternating up/down apical domain conformations, shown as in (D). Note that client extensions (#) are only proximal to 'down' protomers (2, 4, 6), and the weak apical domain density for protomer 7 at the symmetry-mismatched interface. (**G**) Client (shown as in (D)) contact with a representative 'down' apical domain (model overlaid with transparent unsharpened map). Putative client-contacting residue are shown. (**H**) Client (shown as in (D)) contact with a representative equatorial domain (filtered map). Putatively client-contacting residue Trp42 is shown, as are the last resolved residues of the C-terminal tail.

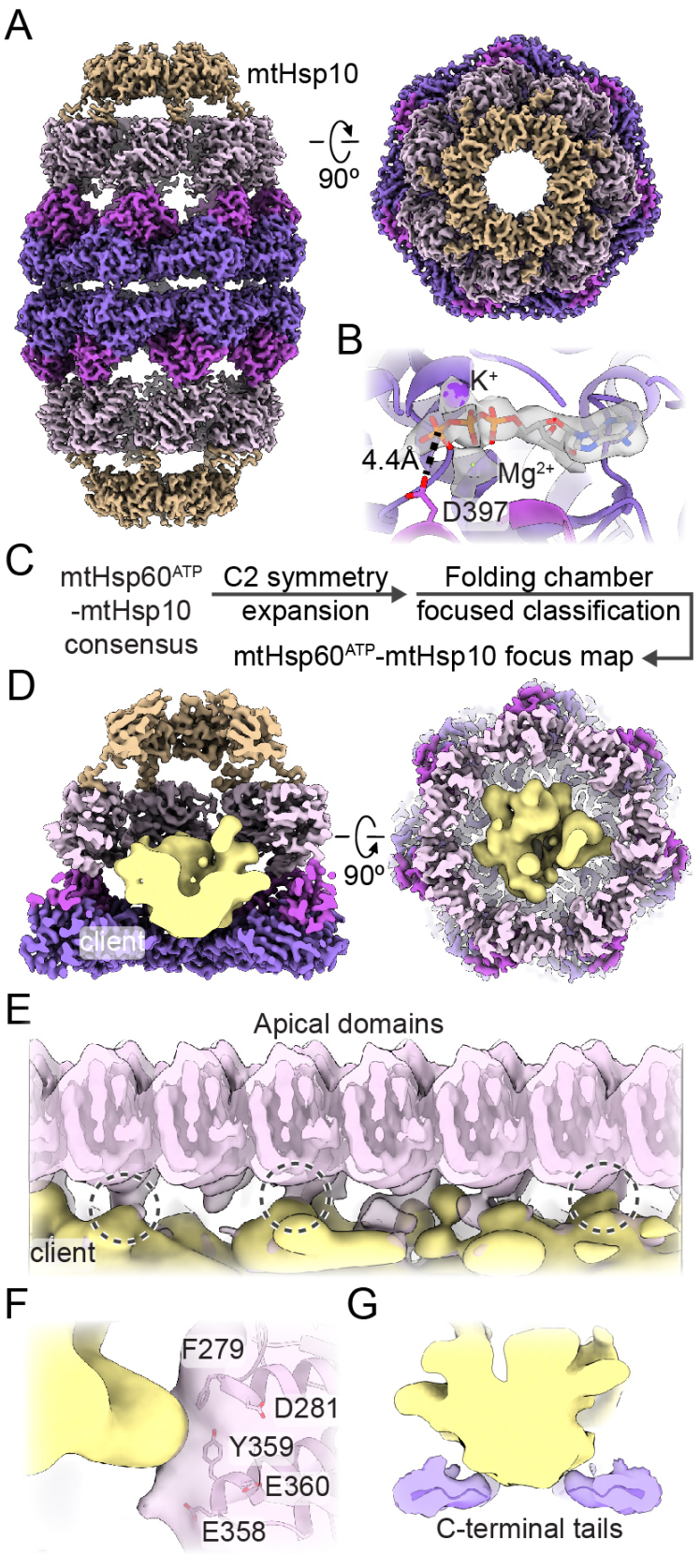
A
mtHsp10
90°
B
K+
4.4Å
Mg2+
D397
C
mtHsp60ATP
-mtHsp10
consensus
C2 symmetry
expansion
Folding chamber
focused classification
mtHsp60ATP-mtHsp10 focus map
D
90°
client
E
Apical domains
client
F
F279
D281
Y359
E360
E358
G
C-terminal tails

Figure 3.3 Analysis of mtHsp10-bound mtHsp60 complexes
(**A**) Sharpened map of mtHsp60^{ATP}-mtHsp10, mtHsp60 colored as in **Figure 3.1**, mtHsp10 in brown. Note uniform quality of all mtHsp60 domains. (**B**) Nucleotide-binding pocket of mtHsp60^{ATP}-mtHsp10, showing density for ATP and the γ-phosphate thereof, and Mg^{2+} and K^{+} ions (gray, from sharpened map). (**C**) Cryo-EM processing workflow to obtain the mtHsp60^{ATP}-mtHsp10 focus map. (**D**) Slabbed views of mtHsp60^{ATP}-mtHsp10 focus map. mtHsp60/mtHsp10 density is shown as the sharpened map, colored as in (A), client is shown as a segmented and 8 Å low-pass filtered map. (**E**) Unwrapped view of the mtHsp60^{ATP}-mtHsp10 focus map, showing client contact with multiple apical domains (encircled). mtHsp60 is shown as an unsharpened map (pink, opaque) overlaid with an 8 Å low-pass filtered map, and client is shown as in (D). (**F**) Enlarged view of client contact with a representative apical domain (both mtHsp60 and client maps are low-pass filtered to 8 Å). Residues putatively involved in client contact are labeled. (**G**) Enlarged view of client contact with the mtHsp60 C-terminal tails.

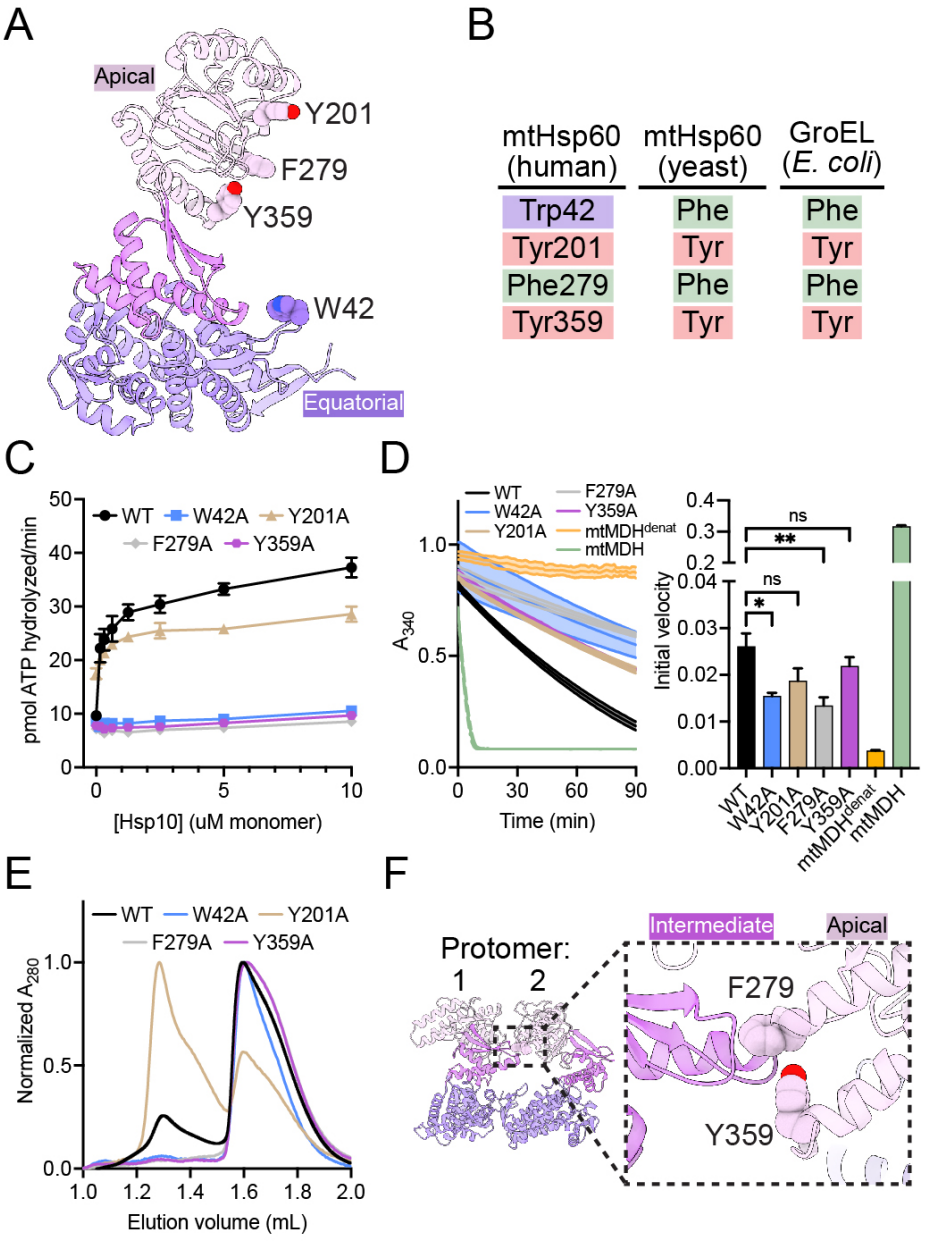

Figure 3.4 Functional analysis of putative client-contacting mtHsp60 residues
(**A**) Protomer of mtHsp60 from mtHsp60^{ATP}-mtHsp10, showing residues mutated. (**B**) Conservation of residues in (A) among human and yeast mtHsp60 and GroEL. (**C**) Steady-state ATPase activity of mtHsp60 mutants vs concentration of mtHsp10. A representative experiment of three biological replicates is shown. Error bars represent standard deviation. (**D**) Enzymatic activity of chemically-denatured human mtMDH refolded by mtHsp60 mutants (left panel, representative of three biological replicates). Dashed lines represent standard deviation of technical triplicates. Initial velocities of absorbance curves from three biological replicates are shown at right. Error bars represent standard error of the mean. *$p < 0.05$, **$p < 0.005$, ns = not significant. (**E**) Analytical size exclusion chromatography traces of mtHsp60 mutants, showing complete monomerization of W42A, F279A, and Y359A mutants. (**F**) Model of two apo-mtHsp60 protomers, showing apical domain residues F279 and Y359 contacting the intermediate domain of an adjacent protomer.

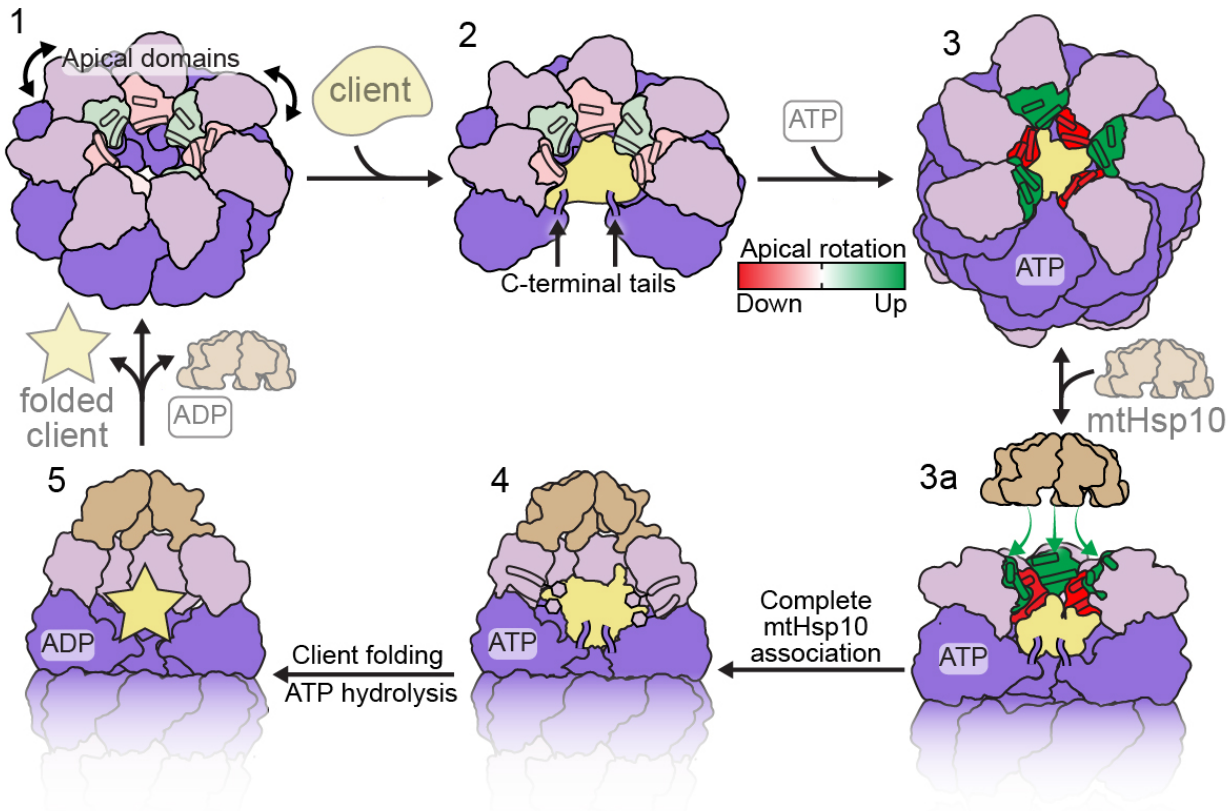

Figure 3.5 Model of conformational changes in the client-engaged mtHsp60 reaction cycle State 1: Apical domains (pink) of mtHsp60^{apo} heptamers are flexible, and exhibit modest rotation about the apical-intermediate hinge, denoted by coloration of helices H and I. State 2: Client binding to mtHsp60^{apo} preserves apical domain asymmetry, and client can localize to multiple depths of the heptamer, facilitated by mtHsp60 apical domains and the flexible C-terminal tails. State 3: ATP binding induces the dimerization of heptamers through the equatorial domains and a more pronounced apical domain asymmetry in an alternating up/down arrangement. Helices H and I in 'down' protomers (red) contact client, while those in 'up' protomers (green) are competent to bind mtHsp10. State 3a: mtHsp10 initially binds the mtHsp60 heptamer using the three upward-facing apical domains; all apical domains then transition to the conformation observed in the mtHsp10-bound complex (state 4). After ATP hydrolysis and client folding (state 5), client, mtHsp10, and ADP are released, and the double-ring complex disassociates into heptamers.

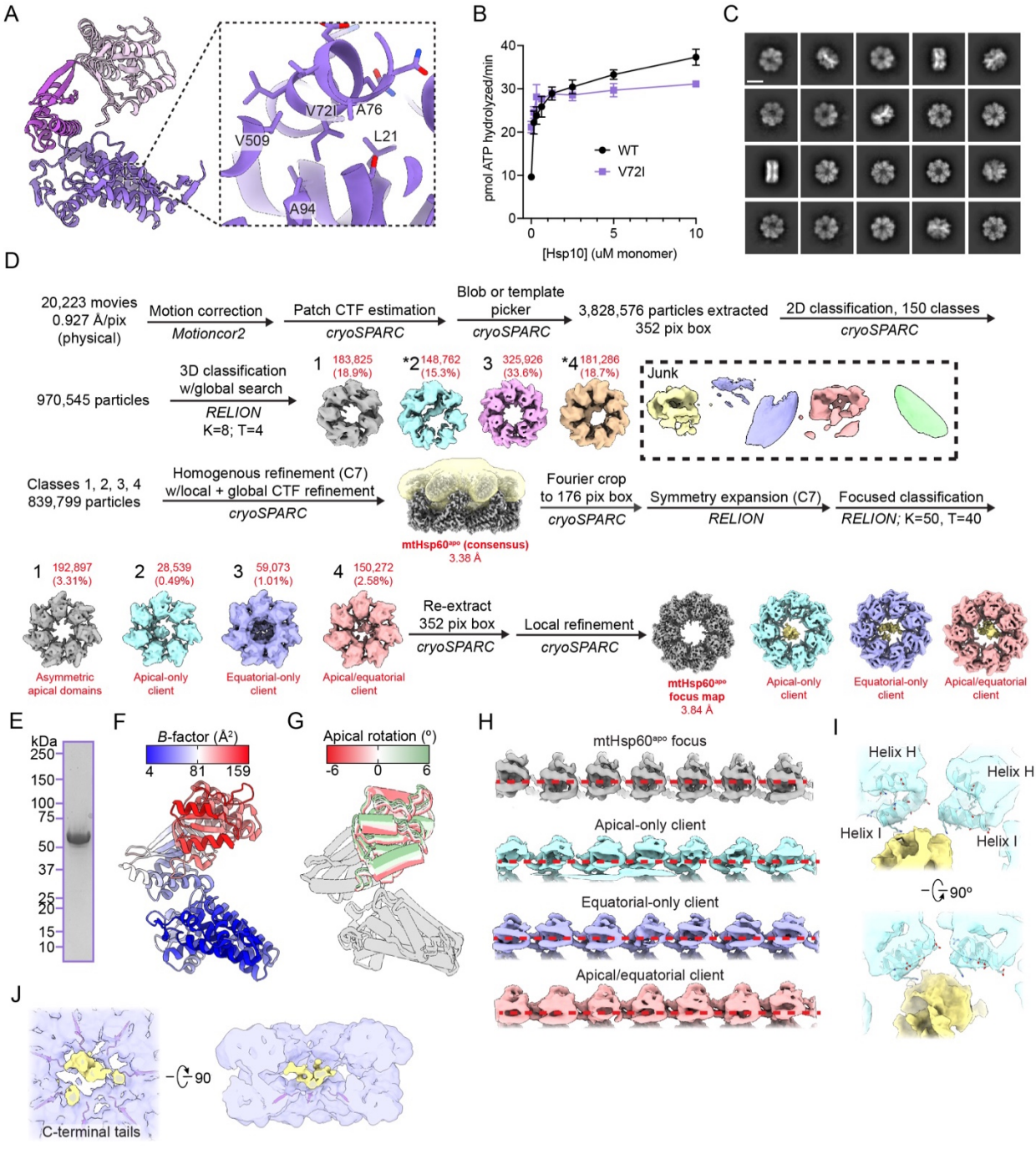
A
V72I
A76
V509
L21
A94
B
pmol ATP hydrolyzed/min
WT
V72I
[Hsp10] (uM monomer)
C
D
20,223 movies
0.927 Å/pix
(physical)
Motion correction
Motioncor2
Patch CTF estimation
cryoSPARC
Blob or template
picker
cryoSPARC
3,828,576 particles extracted
352 pix box
2D classification, 150 classes
cryoSPARC
970,545 particles
3D classification
w/global search
RELION
K=8; T=4
1 183,825 (18.9%)
*2 148,762 (15.3%)
3 325,926 (33.6%)
*4 181,286 (18.7%)
Junk
Classes 1, 2, 3, 4
839,799 particles
Homogenous refinement (C7)
w/local + global CTF refinement
cryoSPARC
mtHsp60apo (consensus)
3.38 Å
Fourier crop
to 176 pix box
cryoSPARC
Symmetry expansion (C7)
RELION
Focused classification
RELION; K=50, T=40
1 192,897 (3.31%)
2 28,539 (0.49%)
3 59,073 (1.01%)
4 150,272 (2.58%)
Asymmetric apical domains
Apical-only client
Equatorial-only client
Apical/equatorial client
Re-extract
352 pix box
cryoSPARC
Local refinement
cryoSPARC
mtHsp60apo focus map
3.84 Å
Apical-only client
Equatorial-only client
Apical/equatorial client
E
kDa
250
150
100
75
50
37
25
20
15
10
F
B-factor (Å²)
4
81
159
G
Apical rotation (°)
-6
0
6
H
mtHsp60apo focus
Apical-only client
Equatorial-only client
Apical/equatorial client
I
Helix H
Helix H
Helix I
Helix I
90°
J
90
C-terminal tails

Figure 3.S1 Biochemical and cryo-EM analysis of apo mtHsp60^{V72I}
(**A**) View of V72I mutation in mtHsp60^{apo}, colored as in **Figure 3.1B**. Adjacent hydrophobic residues also labeled. (**B**) Steady-state ATPase activity of mtHsp60 (black) and mtHsp60^{V72I} (purple) as a function of mtHsp10 concentration. A representative experiment of three biological replicates is shown. Error bars represent standard deviation. (**C**) Representative 2D class averages from the mtHsp60^{apo} dataset. Scale bar equals 100 Å. (**D**) Cryo-EM processing workflow for structures obtained from the mtHsp60^{apo} dataset. The mask used for focused classification is shown in transparent yellow with the consensus map. Client-containing maps from the initial 3D classification are indicated (*). (**E**) Coomassie Brilliant Blue-stained SDS-PAGE gel of recombinant mtHsp60^{V72I}, showing no strong additional bands corresponding to other proteins. (**F**) Protomer of apo mtHsp60 consensus colored by *B*-factor. (**G**) Overlay of mtHsp60^{apo} focus protomers, with apical domains colored as in **Figure 3.1I**. (**H**) Unwrapped views of unsharpened mtHsp60^{apo} focus and client-bound maps, showing apical domain asymmetry. Horizontal red dashed lines are for clarity. (**I**) Enlarged view of apical domain helices H and I from the mtHsp60^{apo} apical-only client map. (**J**) Enlarged view of resolved portions of C-terminal tails from the mtHsp60^{apo} equatorial-only client map.

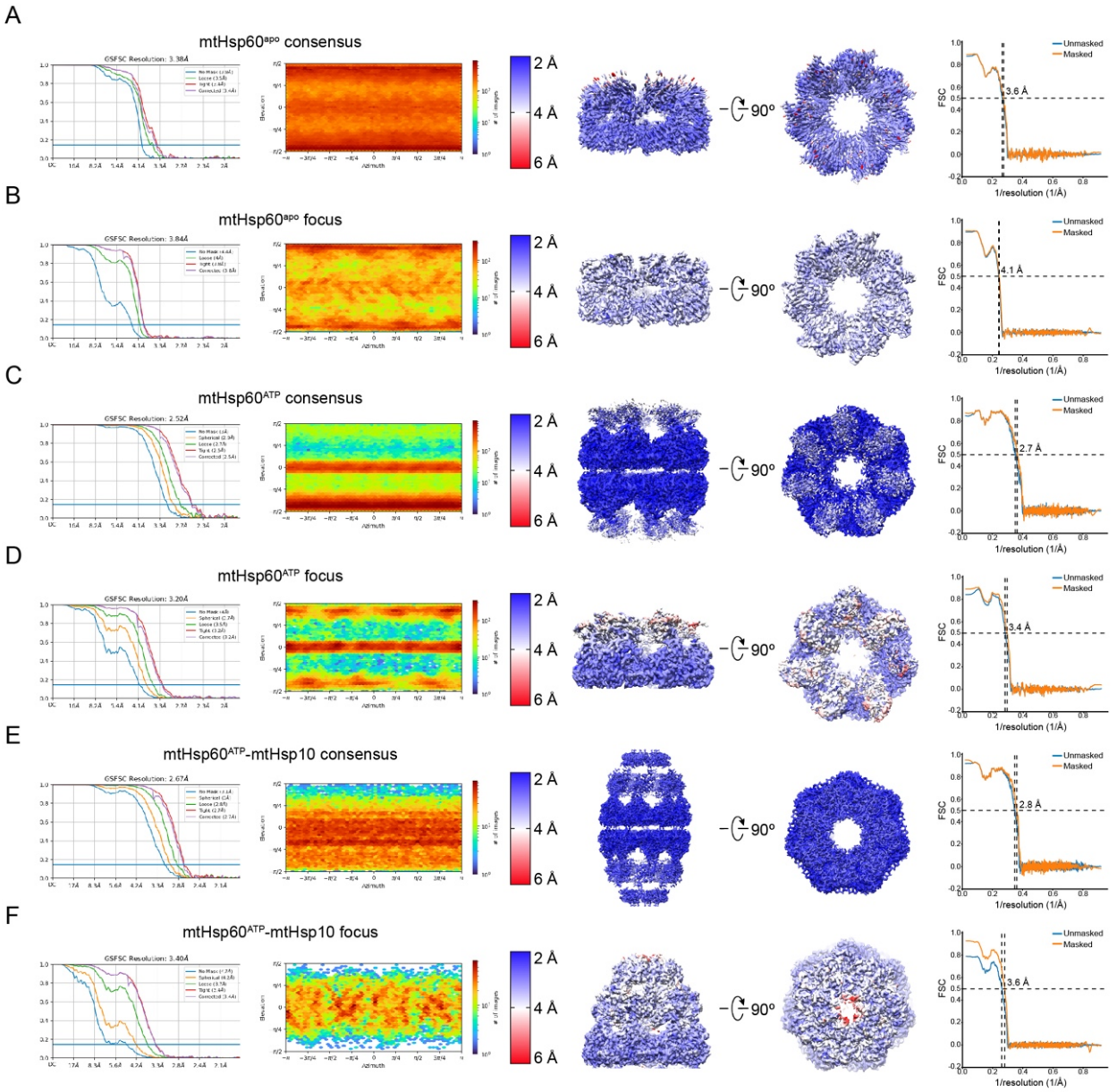

Figure 3.S2 Cryo-EM densities and resolution estimation from the mtHsp60^{V72I} datasets
Fourier Shell Correlation (FSC) curves, orientation distribution plots, sharpened maps colored by local resolution (0.143 cutoff), and map-model FSC curves for (**A**) mtHsp60^{apo} consensus, (**B**) mtHsp60^{apo} focus, (**C**) mtHsp60^{ATP} consensus, (**D**) mtHsp60^{ATP} focus, (**E**) mtHsp60^{ATP}-mtHsp10 consensus, and (**F**) mtHsp60^{ATP}-mtHsp10 focus structures. Displayed model resolutions for map-model FSC plots were determined using the masked map.

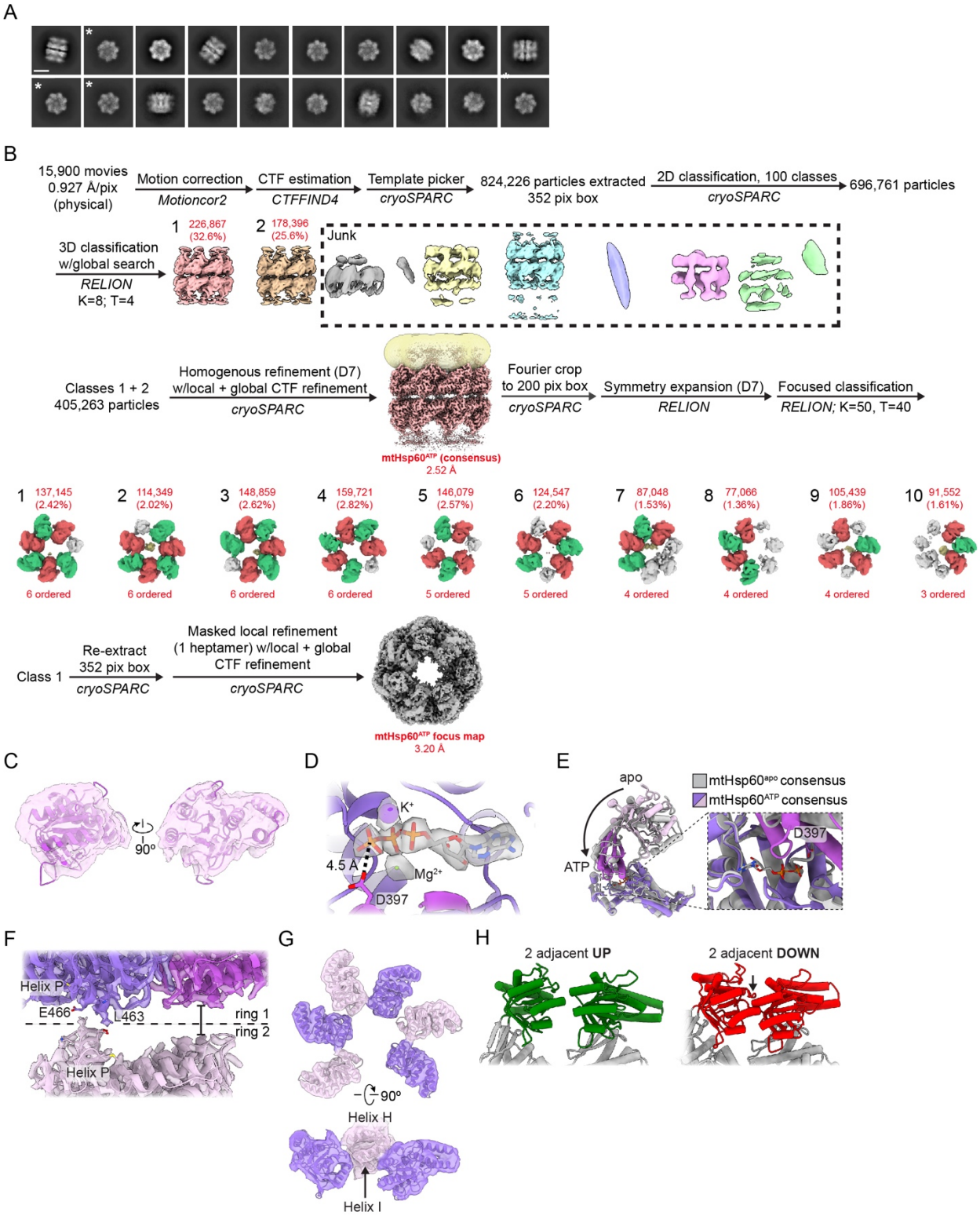
A
B
15,900 movies
0.927 Å/pix
(physical)
Motion correction
Motioncor2
CTF estimation
CTFFIND4
Template picker
cryoSPARC
824,226 particles extracted
352 pix box
2D classification, 100 classes
cryoSPARC
696,761 particles
3D classification
w/global search
RELION
K=8; T=4
1 226,867 (32.6%)
2 178,396 (25.6%)
Junk
Classes 1 + 2
405,263 particles
Homogenous refinement (D7)
w/local + global CTF refinement
cryoSPARC
Fourier crop
to 200 pix box
cryoSPARC
Symmetry expansion (D7)
RELION
Focused classification
RELION; K=50, T=40
mtHsp60ATP (consensus)
2.52 Å
1 137,145 (2.42%) 6 ordered
2 114,349 (2.02%) 6 ordered
3 148,859 (2.62%) 6 ordered
4 159,721 (2.82%) 6 ordered
5 146,079 (2.57%) 5 ordered
6 124,547 (2.20%) 5 ordered
7 87,048 (1.53%) 4 ordered
8 77,066 (1.36%) 4 ordered
9 105,439 (1.86%) 4 ordered
10 91,552 (1.61%) 3 ordered
Class 1
Re-extract
352 pix box
cryoSPARC
Masked local refinement
(1 heptamer) w/local + global
CTF refinement
cryoSPARC
mtHsp60ATP focus map
3.20 Å
C
90°
D
K+
4.5 Å
Mg2+
D397
E
apo
ATP
mtHsp60apo consensus
mtHsp60ATP consensus
D397
F
Helix P
E466
L463
ring 1
ring 2
Helix P
G
90°
Helix H
Helix I
H
2 adjacent UP
2 adjacent DOWN

Figure 3.S3 Cryo-EM analysis of ATP-bound mtHsp60^{V72I}
(**A**) Representative 2D class averages from the mtHsp60^{ATP} dataset. Scale bar equals 100 Å. Top views of single-ring complexes are indicated (*). (**B**) Cryo-EM processing workflow for structures obtained from the mtHsp60^{ATP} dataset. The mask used for focused classification is shown in transparent yellow with the consensus map. Protomers from focused classification maps are colored in green (apical domain facing upward), red (apical domain facing downward), or gray (disordered apical domain). Class 1 was selected for refinement based on visual assessment of map quality. (**C**) View of an apical domain from the unsharpened mtHsp60^{ATP} consensus map and associated model. (**D**) Nucleotide-binding pocket of mtHsp60^{ATP}, showing density for ATP and the γ-phosphate thereof, and Mg^{2+} and K^{+} ions (gray, from sharpened map). (**E**) Overlay of consensus mtHsp60^{apo} and mtHsp60^{ATP} models, aligned by the equatorial domain, showing a downward rotation of the intermediate and apical domains in the ATP-bound state. (**F**) Inter-ring interface of the sharpened mtHsp60^{ATP} consensus map and fitted model, showing contact at the left interface mediated by helix P, but no contact at the right interface. Each protomer is colored a different shade of purple. (**G**) Unsharpened map and model of apical domains of mtHsp60^{ATP} focus. 'Down' protomers are colored purple, 'up' protomers are colored pink. (**H**) Modeling of two adjacent ATP-bound 'up' (left) or 'down' (right) protomers, generated by aligning a copy of chain C of mtHsp60^{ATP} focus with chain D (up pair) or a copy of chain D with chain C (down pair). A large clash is observed with two adjacent down protomers, while two adjacent up protomers appear compatible.

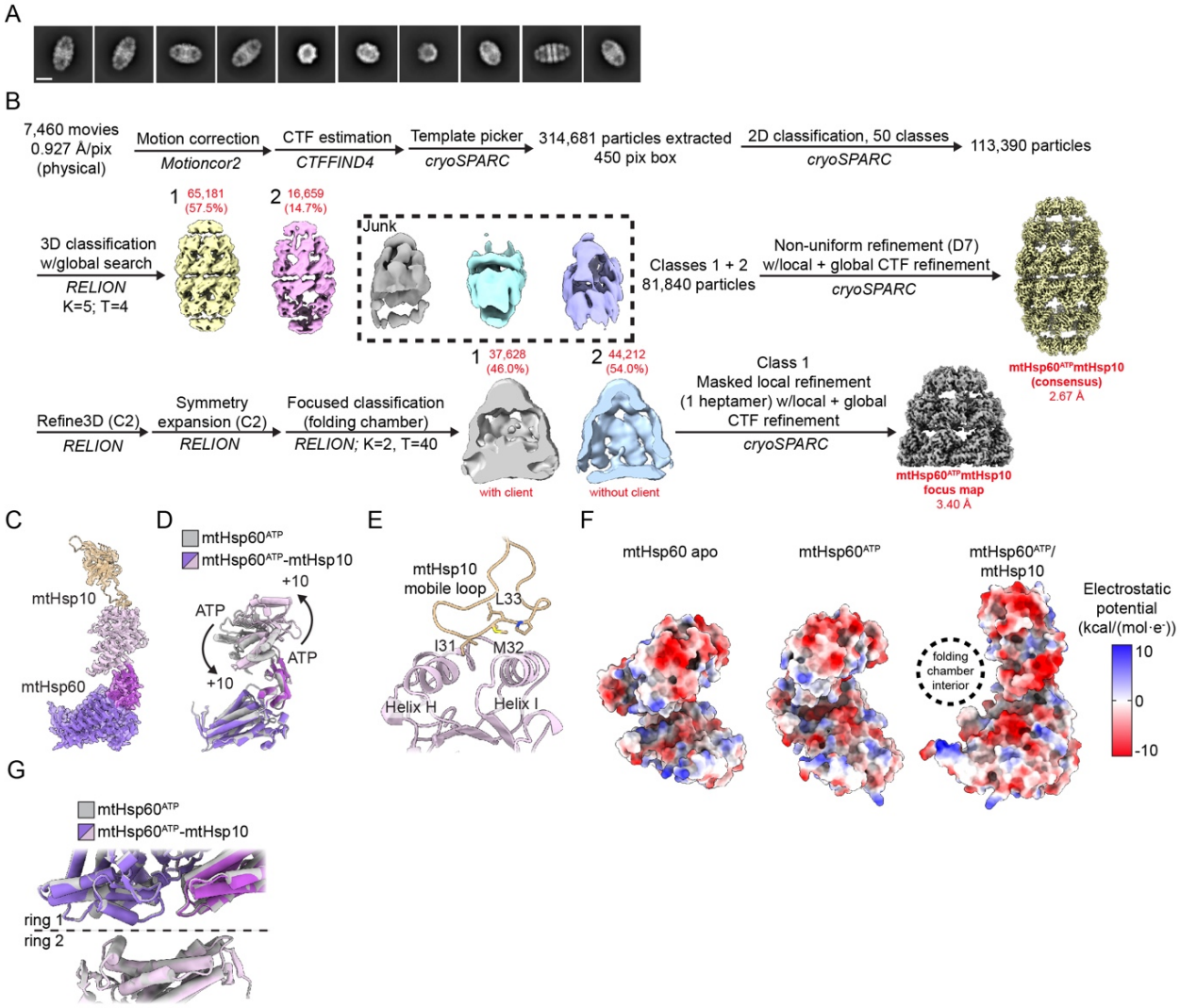

Figure 3.S4 Cryo-EM analysis of ATP/mtHsp10-bound mtHsp60^{V72I}
(**A**) Representative 2D class averages from the mtHsp60^{ATP}-mtHsp10 dataset. Scale bar equals 100 Å. (**B**) Cryo-EM processing workflow for structures obtained from the mtHsp60^{ATP}-mtHsp10 dataset. (**C**) Sharpened map and model for the asymmetric unit of the mtHsp60^{ATP}-mtHsp10 consensus structure. (**D**) Overlay of consensus models for mtHsp60^{ATP} and mtHsp60^{ATP}-mtHsp10 structures, showing identical equatorial and intermediate domain conformations but a large upward apical domain rotation. (**E**) Model of the mtHsp10 mobile loop and associated mtHsp60 apical domain in the mtHsp60^{ATP}-mtHsp10 consensus map, showing interaction of conserved hydrophobic residues with apical domain helices H and I. (**F**) Coulombic potential maps of protomers of mtHsp60 apo, mtHsp60^{ATP}, and mtHsp60^{ATP}-mtHsp10 consensus structures, showing increased negative charge in the inward-facing regions of mtHsp60^{ATP}-mtHsp10. (**G**) Overlay of consensus models for mtHsp60^{ATP} and mtHsp60^{ATP}-mtHsp10 structures, showing highly similar inter-ring conformations.

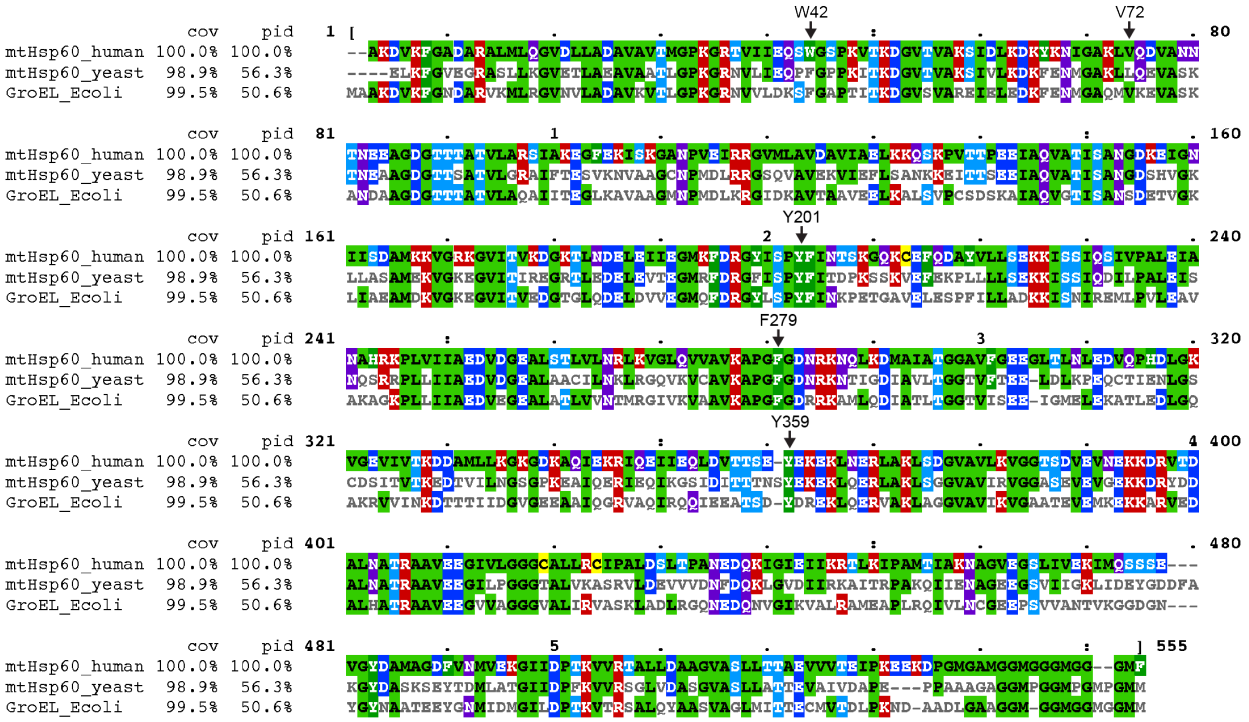

Figure 3.S5 Alignments of group I chaperonin amino acid sequences
Alignments of mature human (residues 27-end) and yeast (*Saccharomyces cerevisiae*, residues 26-end) mitochondrial Hsp60 and *E. coli* GroEL amino acid sequences. Residues mutated in this study are indicated (numbering corresponds to the human sequence). Cov = covariance relative to the human sequence, Pid = percent identity relative to the human sequence.

Tables

Table 3.1 Cryo-EM data collection, refinement, and validation statistics of mtHsp60 structures

	mtHsp60^{apo} consensus (EMD-29813, PDB 8G7J)	mtHsp60^{apo} focus (EMD-29814, PDB 8G7K)	mtHsp60^{ATP} consensus (EMD-29815, PDB 8G7L)	mtHsp60^{ATP} focus (EMD-29816, PDB 8G7M)	mtHsp60^{ATP}-mtHsp10 consensus (EMD-29817, PDB 8G7N)	mtHsp60^{ATP}-mtHsp10 focus (EMD-29818, PDB 8G7O)
Data collection and processing						
Microscope and camera	Glacios, K2	Glacios, K2	Glacios, K2	Glacios, K2	Glacios, K2	Glacios, K2
Magnification	53,937	53,937	53,937	53,937	53,937	53,937
Voltage (kV)	200	200	200	200	200	200
Data acquisition software	SerialEM	SerialEM	SerialEM	SerialEM	SerialEM	SerialEM
Exposure navigation	Image shift	Image shift	Image shift	Image shift	Image shift	Image shift
Electron exposure ($e^-/Å^2$)	66	66	66	66	66	66
Defocus range (μm)	-0.5 to -2.5	-0.5 to -2.5	-1.0 to -2.5	-1.0 to -2.5	-0.5 to -3.0	-0.5 to -3.0
Pixel size (Å)	0.927	0.927	0.927	0.927	0.927	0.927
Symmetry imposed	C7	C1	D7	C1	D7	C1
Initial particle images (no.)	970,545	970,545	696,761	696,761	113,390	113,390
Final particle images (no.)	839,799	192,680	405,263	137,145	81,840	37,628
Map resolution (Å)	3.4	3.8	2.5	3.2	2.7	3.4
FSC threshold	0.143	0.143	0.143	0.143	0.143	0.143
Map resolution range (Å)	2.5-8	3-6	2-6	2.5-8	2-7	2.5-8
Refinement						
Model resolution (Å)	3.6	4.1	2.7	3.4	2.8	3.6
FSC threshold	0.5	0.5	0.5	0.5	0.5	0.5
Map sharpening *B* factor ($Å^2$)	-221.8	-157.4	-127.9	-120.0	-120.6	-91.8
Model composition						
Nonhydrogen atoms	27,461	27,461	55,524	26,334	66,122	33,047
Protein residues	3,682	3,682	7,378	3,505	8,778	4,389
Ligands	0	0	42	21	42	7
B factors ($Å^2$)						
Protein	67.39	67.39	107.82	107.52	39.67	90.40
Ligand	N/A	N/A	23.99	44.80	11.75	61.26
R. m. s. deviations						
Bond lengths (Å)	0.015	0.014	0.008	0.004	0.004	0.003
Bond angles (°)	1.525	1.509	1.350	0.940	0.972	0.572
Validation						
MolProbity score	0.83	0.87	0.91	1.25	1.04	1.24
Clashscore	1.16	1.41	1.63	4.88	2.56	3.99
Poor rotamers (%)	0.00	0.00	0.79	0.00	0.20	0.00
Ramachandran plot						
Favored (%)	99.24	98.99	99.37	99.17	99.04	97.78
Allowed (%)	0.68	0.82	0.63	0.83	0.96	2.22
Disallowed (%)	0.08	0.19	0.00	0.00	0.00	0.00

Supplemental Files

Movie 3.1 Summary of conformational changes and client contacts in the mtHsp60 reaction cycle

Morphs between mtHsp60^{apo} focus, mtHsp60^{ATP} focus, and mtHsp60^{ATP}-mtHsp10 focus are shown, with experimental client density appearing at each stage. In apo and ATP-bound models helices H and I are colored according to apical domain rotation. For clarity, only one ring of mtHsp60^{ATP} and mtHsp60^{ATP}-mtHsp10 are shown.

Methods

Molecular cloning

The Q5 Site-Directed Mutagenesis kit (New England Biolabs) was used to introduce mutations into the mtHsp60 expression construct.

Protein expression and purification

Human mtHsp60 constructs and mtHsp10 were expressed and purified as previously described (39, 46). In brief, mtHsp60 variants ('mature' construct, residues 27-end) and full-length mtHsp10 were cloned into pMCSG7, containing a TEV protease-cleavable N-terminal 6xHis tag. pMCSG7-mtHsp60^{WT}, pMCSG7-mtHsp60^{V72I}, and pMCSG7-mtHsp10 were transformed into *E. coli* BL21(DE3) chemically competent cells (New England Biolabs) using standard protocols. BL21 cells were grown in Terrific Broth supplemented with 100 µg/ml ampicillin at 37 °C with shaking until OD_{600} of ~1 was reached. Cultures were then induced with 400 µM isopropyl β-D-1-thiogalactopyranoside (IPTG) and incubated at 37°C for 4 hours with shaking. Cells were harvested by centrifugation for 10 minutes at 4,000 rpm, and stored at -80 °C until use.

All purification steps were performed at 4 °C unless otherwise specified. Cell pellets were resuspended in His-binding buffer (50 mM Tris pH 8.0, 10 mM imidazole, 500 mM NaCl), supplemented with EDTA-free protease inhibitor cocktail (Roche). The resuspensions were

homogenized by douncing and lysed by sonication. Lysates were clarified by centrifugation at 17,000 rpm for 30 min. Lysate supernatants were incubated with HisPur Ni-NTA resin (Thermo Scientific) for 1 hour. The resin was washed with His-washing buffer (50 mM Tris pH 8.0, 30 mM imidazole, 300 mM NaCl), and eluted with His-elution buffer (50 mM Tris pH 8.0, 300 mM imidazole, 300 mM NaCl). The 6xHis tags were removed by incubating the elutions with TEV protease and 1 mM DTT for 4 hours at room temperature, followed by overnight dialysis in SEC buffer (50 mM Tris pH 7.7, 300 mM NaCl, 10 mM $MgCl_2$). The next day, uncleaved protein was removed by a reverse nickel column and concentrated for reconstitution/size exclusion chromatography. mtHsp10 heptamers were purified on a HiLoad 16/600 Superdex 200 pg column (GE Healthcare) equilibrated in SEC buffer. mtHsp60 oligomers were reconstituted by mixing mtHsp60 with KCl, $Mg(OAc)_2$ and ATP in the following ratio: 573 µL mtHsp60, 13 µL of 1 M KCl, 13 µL 1 M $Mg(OAc)_2$, and 52 µL 50 mM ATP. After incubation at 30 °C for 90 minutes, the mixture was applied to the same SEC column, and the oligomeric fractions were collected, supplemented with 5% glycerol, concentrated, flash frozen in liquid nitrogen, and stored at -80 °C.

The mtMDH bacterial expression vector was a gift from Nicola Burgess-Brown (Addgene plasmid #38792; https://www.addgene.org/38792/). The vector was transformed into Rosetta 2(DE3)pLysS chemically competent cells (Novagen) using standard protocols. Rosetta 2 cells were grown in Terrific Broth supplemented with 50 µg/ml kanamycin and 25 µg/ml chloramphenicol at 37 °C with shaking until OD_{600} of ~1 was reached. Cultures were then induced with 500 µM IPTG and incubated at 18°C overnight with shaking. Cells were harvested by centrifugation for 10 minutes at 4000 rpm, and stored at -80 °C until use.

All purification steps were performed at 4 °C. A cell pellet was resuspended in mtMDH His-binding buffer (50 mM HEPES pH 7.5, 20 mM imidazole, 500 mM NaCl, 5% glycerol), supplemented with EDTA-free protease inhibitor cocktail (Roche). The resuspension was homogenized by douncing and lysed by sonication. The lysate was clarified by centrifugation at

17,000 rpm for 30 min, filtered, and applied to a 5 mL HisTrap column (GE Healthcare). The column was washed with 5 column volumes of mtMDH His-binding buffer, and eluted with a 10 column volume gradient of mtMDH His-elution buffer (50 mM HEPES pH 7.5, 250 mM imidazole, 500 mM NaCl, 5% glycerol). Fractions containing mtMDH were concentrated and injected onto a HiLoad 16/600 Superdex 200 pg column (GE Healthcare) equilibrated in mtMDH SEC buffer (10 mM HEPES pH 7.5, 500 mM NaCl, 5% glycerol, 0.5 mM TCEP). Fractions enriched in mtMDH were concentrated, flash-frozen in liquid nitrogen, and stored at -80 °C.

Purity of all proteins was verified by SDS-PAGE and concentration was determined using the Pierce BCA Protein Assay Kit (Thermo Scientific).

SEC-MALS and analytical SEC

For SEC-MALS, mtHsp60 samples (17 μM monomer) incubated with 1 mM ATP where applicable were injected onto an SEC column (Shodex Protein KW-804) equilibrated at room temperature in MALS buffer (20 mM HEPES pH 7.5, 100 mM KCl, 10 mM $MgCl_2$) connected to an in-line DAWN HELEOS multi-angle light scattering detector and Optilab T-rEX differential refractive index detector (Wyatt Technology Corporation). Molecular weights of proteins were determined with the ASTRA V software package (Wyatt Technology Corporation). For analytical SEC, mtHsp60 samples (17 μM monomer) were injected onto a Superdex 200 Increase 3.2/300 column equilibrated at room temperature in MALS buffer.

BIOMOL Green ATPase assay

ATPase activity was measured in 96-well plates using an assay reported previously (63), with minor modifications. In brief, 500 nM mtHsp60 monomer (final) was incubated with a two-fold dilution series of mtHsp10, starting at 10 uM monomer (final), in ATPase buffer (100 mM Tris pH 7.4, 20 mM KCl, 6 mM $MgCl_2$, 0.01% Triton X-100). ATP was added to 1 mM (final), and the reactions (25 μL total) were incubated for 1 hour at 37 °C. After incubation, 80 μL of BIOMOL

Green reagent (Enzo Life Sciences) was added to each well, immediately followed by 10 µL of 32% w/v sodium citrate, to limit nonenzymatic hydrolysis of ATP. The reactions were mixed and incubated at 37 °C for 15 minutes, and then A_{620} was measured on a SpectraMax M5 (Molecular Devices). ATP hydrolysis (pmol ATP hydrolyzed/min) was quantified using a standard curve of sodium phosphate and the following equation:

$$\text{pmol ATP hydrolyzed/min} = \frac{A_{620} \times \text{reaction volume (µL)}}{\text{slope of standard curve } \left(A_{620}/\text{µM phosphate}\right) \times \text{incubation time (min)}}$$

mtMDH refolding assay

mtMDH activity after refolding by mtHsp60/10 was measured using a previously reported assay with minor modifications (46). To prepare chemically denatured mtMDH ($mtMDH^{denat}$), mtMDH was incubated for 1 hour at room temperature in denaturant buffer (50 mM Tris pH 7.4, 6 M guanidine HCl, 10 mM DTT). A binary complex of mtHsp60-$mtMDH^{denat}$ was prepared by adding $mtMDH^{denat}$ (120 nM final) to mtHsp60 (3.33 µM final) in mtMDH reaction buffer (50 mM Tris pH 7.4, 20 mM KCl, 10 mM $MgCl_2$, 1 mM DTT), and incubating for 10 minutes at room temperature. mtHsp10 (6.67 µM final) was added to this mixture, and 30 µL aliquots were transferred to 96-well plates in triplicate. 20 µL ATP was added to each well (1 mM final), and reactions were incubated at 37 °C for 1 hour. After incubation, an equivalent amount of mtMDH or $mtMDH^{denat}$ was added to the plate as controls for mtMDH activity, and 10 µL of 500 mM EDTA pH 8.0 was added to all wells to quench mtHsp60-mediated refolding. 20 µL of mtMDH enzymatic reporter (2.4 mM NADH, 20 mM sodium mesoxalate dissolved in mtMDH reaction buffer, freshly prepared for each assay) was added to all wells, and A_{340} was measured by a SpectraMax M5 (Molecular Devices) for 90 minutes at room temperature. Initial velocities of NADH oxidation were calculated using the following equation:

$$\text{Initial velocity } \left(\frac{A_{340}}{\text{min}}\right) = -1 \times \frac{A_{340_{t=3\text{ min}}} - A_{340_{t=0\text{ min}}}}{3\text{ min}}$$

Significance testing for calculated initial velocities was performed using Dunnett's multiple comparison test, using mtHsp60^{WT} as the control.

SDS-PAGE analysis

mtHsp60^{V72I} (10 µL of 5 µM monomer) was loaded on a 4-15% TGX gel (Bio-Rad), run for 30 min at 200 V, and stained using Coomassie Brilliant Blue R-250 (Bio-Rad).

Cryo-EM sample preparation, data collection, and image processing

For apo mtHsp60 samples, 2.4 mg/mL mtHsp60 was prepared in ATPase buffer (without detergent), supplemented with 0.1% n-Octyl-beta-D-glucopyranoside (Alfa Aesar) to improve particle orientation distribution. For samples with ATP, 0.2-0.6 mg/mL mtHsp60 was prepared in ATPase buffer (without detergent), supplemented with 1 mM ATP. For samples with mtHsp10, 6.3 mg/mL mtHsp60 and 1.3 mg/mL mtHsp10 were prepared in ATPase buffer, supplemented with 1 mM ATP and 0.1% amphipol A8-35 (Anatrace) to improve particle orientation distribution. 3 µL of each sample was applied to glow-discharged (PELCO easiGlow, 15 mA, 2 min) holey carbon grid (Quantifoil R1.2/1.3 on gold or copper 200 mesh support), blotted for 3 seconds with Whatman Grade 595 filter paper (GE Healthcare), and plunge frozen into liquid ethane cooled by liquid nitrogen using a Vitrobot (Thermo Fisher Scientific) operated at 4 or 22 °C and 100% humidity. Samples were imaged on a Glacios TEM (Thermo Fisher Scientific) operated at 200 kV and equipped with a K2 Summit direct electron detector (Gatan). Movies were acquired with SerialEM (64) in super-resolution mode at a calibrated magnification of 53,937, corresponding to a physical pixel size of 0.927 Å. A nominal defocus range of -1.0 to -2.0 µm was used with a total exposure time of 10 sec fractionated into 0.1 sec frames for a total dose of 66 $e^-/Å^2$ at a dose rate of 6 e^-/pix/s. Movies were subsequently corrected for drift, dose-weighted, and Fourier-cropped by a factor of 2 using MotionCor2 (65).

For the apo-mtHsp60 dataset, a total of 20,223 micrographs were collected over two different sessions and initially processed in cryoSPARC (66). After Patch CTF estimation, micrographs were manually curated to exclude those of poor quality, followed by blob- or template-based particle picking, 2D classification, and *ab initio* modeling in cryoSPARC. Datasets were processed separately through 2D classification, and particles selected from 2D analysis were subjected to an initial 3D classification in RELION (67). Four classes resembled mtHsp60 heptamers, some of which contained density in the central cavity likely corresponding to a bound client. The particles from these four classes were jointly refined in cryoSPARC with C7 symmetry imposed. This resulted in the mtHsp60^{apo} consensus map, which featured well-resolved equatorial and intermediate domains but very poor density for the apical domains. To improve the resolution of the apical domains and resolve client, particles from this refinement were symmetry expanded in C7 and subjected to focused classification without image alignment (hereafter referred to as skip-align classification), using a mask encompassing all apical domains and the central cavity. This resulted in a number of classes with significantly improved apical domains in asymmetric conformations (for example, class 1), as well as a number of classes with moderate apical domain resolutions but strong density corresponding to client (classes 2-4). Particles from each of these classes were re-extracted and locally refined to obtain the entire structure.

For the mtHsp60/ATP dataset, a total of 15,900 micrographs were collected over three different sessions, and initially processed as for apo-mtHsp60, leaving particles from different collections separate until initial 3D classification in RELION. Two classes from this job, both double-ring tetradecamers with weak central density corresponding to client, were jointly refined in cryoSPARC with D7 symmetry enforced, yielding the mtHsp60^{ATP} consensus map. As for the mtHsp60^{apo} consensus map, the equatorial and intermediate domains were well-resolved in this map, but density for the apical domains was extremely poor, indicating significant conformational flexibility. To better resolve the apical domains, skip-align focused classification was performed

on D7-symmetry expanded particles, using a mask that encompassed the apical domains of 1 heptamer. This yielded many classes with between three and six ordered apical domains, with the remainder of the apical domains being poorly resolved. Local refinement in cryoSPARC of the best class (class 1) yielded the mtHsp60^{ATP} focus map.

For the mtHsp60/mtHsp10/ATP dataset, a total of 7,460 micrographs were collected across two different sessions, and initially processed as for apo-mtHsp60, leaving particles from different collections separate until initial 3D classification in RELION. Two classes from this job, both resembling double-ring complexes with each ring bound by mtHsp10, were jointly refined in cryoSPARC with D7 symmetry imposed, resulting in the mtHsp60^{ATP}-mtHsp10 consensus map. Weak density in the central cavities prompted further analysis to classify rings with and without client density. To this end, a mask was created encompassing the folding chamber of one ring, with minimal density for mtHsp60 or mtHsp10. A skip-align focused classification into two classes was performed in RELION on C2-symmetry expanded particles, which resulted in classes with and without client density. The class with client was locally refined in cryoSPARC using a mask that encompassed the entire ring, resulting in the mtHsp60^{ATP}-mtHsp10 focus map.

Molecular modeling

For the mtHsp60^{apo} consensus structure, a previously published model (PDB 7AZP) was docked and refined against the sharpened map using Rosetta Fast Torsion Relax. The V72I mutations were made using Coot (68). This model was then refined against the sharpened mtHsp60^{apo} focus map. For the mtHsp60^{ATP} consensus structure, a chain from a previously published model (PDB 6MRC) was docked into an asymmetric unit of the unsharpened map, and the apical domain was rigid-body docked using Phenix Real Space Refine (69). The V72I mutation and ligand modifications were then made in Coot, followed by generation of the complete 14-mer in Phenix and refinement against the sharpened map using Phenix Real Space Refine. One heptamer from this model was docked into the sharpened mtHsp60^{ATP} focus map, and refined using Phenix Real

Space Refine. The disordered apical domain was omitted from the model due to extremely poor resolution. For the mtHsp60^{ATP}-mtHsp10 consensus structure, a protomer pair of mtHsp60-mtHsp10 from a previously published model (PDB 6MRC) was docked into an asymmetric unit of the sharpened map. The V72I mutation and ligand modifications were then made in Coot, followed by generation of the complete 14-mer in Phenix and refinement against the sharpened map using Phenix Real Space Refine. One ring of this model was then docked into the sharpened mtHsp60^{ATP}-mtHsp10 focus map, and refined using Phenix Real Space Refine. Coot, ISOLDE(70), and Phenix were used to finalize all models.

Data analysis and figure preparation

Biochemical data was analyzed and plotted using Prism 9.3.1 (GraphPad). Figures were prepared using Adobe Illustrator, UCSF Chimera, and UCSF ChimeraX (71, 72).

Resource Availability

Materials availability:

Requests for resources and reagents should be directed to Daniel R. Southworth.

Data availability:

Cryo-EM densities have been deposited at the Electron Microscopy Data Bank under accession codes EMD: 29813 (mtHsp60^{apo} consensus), EMD: 29814 (mtHsp60^{apo} focus), EMD: 29815 (mtHsp60^{ATP} consensus), EMD: 29816 (mtHsp60^{ATP} focus), EMD: 29817 (mtHsp60^{ATP}-mtHsp10 consensus), and EMD: 29818 (mtHsp60^{ATP}-mtHsp10 focus). Atomic coordinates have been deposited at the Protein Data Bank under accession codes PDB: 8G7J (mtHsp60^{apo} consensus), PDB: 8G7K (mtHsp60^{apo} focus), PDB: 8G7L (mtHsp60^{ATP} consensus), PDB: 8G7M (mtHsp60^{ATP} focus), PDB: 8G7N (mtHsp60^{ATP}-mtHsp10 consensus), and PDB: 8G7O (mtHsp60^{ATP}-mtHsp10 focus).

Acknowledgments

We thank Axel Brilot for helpful advice regarding cryo-EM data processing. This work was supported by NIH grants F31GM142279 (to J.R.B.), NS059690 (to J.E.G.), and R01GM138690 (to D.R.S.).

Author Contributions

J.R.B. cloned mtHsp60 mutants, expressed and purified proteins, performed biochemical and cryo-EM experiments, built models, developed figures, and wrote and edited the manuscript. H.S. expressed and purified proteins. E.T. operated electron microscopes and assisted with data collection. J.E.G. and D.R.S. designed and supervised the project and wrote and edited the manuscript.

References

1. Balchin, D., Hayer-Hartl, M., and Hartl, F. U. (2016) In vivo aspects of protein folding and quality control. *Science*. 353, aac4354
2. Horwich, A. L., and Fenton, W. A. (2020) Chaperonin-assisted protein folding: a chronologue. *Q Rev Biophys*. 53, e4
3. Yébenes, H., Mesa, P., Muñoz, I. G., Montoya, G., and Valpuesta, J. M. (2011) Chaperonins: two rings for folding. *Trends Biochem Sci*. 36, 424–432
4. Lopez, T., Dalton, K., and Frydman, J. (2015) The Mechanism and Function of Group II Chaperonins. *J Mol Biol*. 427, 2919–2930
5. Hayer-Hartl, M., Bracher, A., and Hartl, F. U. (2016) The GroEL–GroES Chaperonin Machine: A Nano-Cage for Protein Folding. *Trends Biochem Sci*. 41, 62–76
6. Fenton, W. A., Kashi, Y., Furtak, K., and Horwich, A. L. (1994) Residues in chaperonin GroEL required for polypeptide binding and release. *Nature*. 371, 614–619
7. Farr, G. W., Furtak, K., Rowland, M. B., Ranson, N. A., Saibil, H. R., Kirchhausen, T., and Horwich, A. L. (2000) Multivalent Binding of Nonnative Substrate Proteins by the Chaperonin GroEL. *Cell*. 100, 561–573
8. Elad, N., Farr, G. W., Clare, D. K., Orlova, E. V., Horwich, A. L., and Saibil, H. R. (2007) Topologies of a Substrate Protein Bound to the Chaperonin GroEL. *Mol Cell*. 26, 415–426
9. Weaver, J., Jiang, M., Roth, A., Puchalla, J., Zhang, J., and Rye, H. S. (2017) GroEL actively stimulates folding of the endogenous substrate protein PepQ. *Nat Commun*. 8, 15934
10. Clare, D. K., Vasishtan, D., Stagg, S., Quispe, J., Farr, G. W., Topf, M., Horwich, A. L., and Saibil, H. R. (2012) ATP-Triggered Conformational Changes Delineate Substrate-Binding and -Folding Mechanics of the GroEL Chaperonin. *Cell*. 149, 113–123

11. Ranson, N. A., Farr, G. W., Roseman, A. M., Gowen, B., Fenton, W. A., Horwich, A. L., and Saibil, H. R. (2001) ATP-Bound States of GroEL Captured by Cryo-Electron Microscopy. *Cell*. 107, 869–879
12. Madan, D., Lin, Z., and Rye, H. S. (2008) Triggering Protein Folding within the GroEL-GroES Complex*. *J Biol Chem*. 283, 32003–32013
13. Cliff, M. J., Limpkin, C., Cameron, A., Burston, S. G., and Clarke, A. R. (2006) Elucidation of Steps in the Capture of a Protein Substrate for Efficient Encapsulation by GroE. *J Biol Chem*. 281, 21266–21275
14. Clare, D. K., Bakkes, P. J., Heerikhuizen, H. van, Vies, S. M. van der, and Saibil, H. R. (2009) Chaperonin complex with a newly folded protein encapsulated in the folding chamber. *Nature*. 457, 107–110
15. Weissman, J. S., Hohl, C. M., Kovalenko, O., Kashi, Y., Chen, S., Braig, K., Saibil, H. R., Fenton, W. A., and Norwich, A. L. (1995) Mechanism of GroEL action: Productive release of polypeptide from a sequestered position under groes. *Cell*. 83, 577–587
16. Xu, Z., Horwich, A. L., and Sigler, P. B. (1997) The crystal structure of the asymmetric GroEL–GroES–(ADP)7 chaperonin complex. *Nature*. 388, 741–750
17. Korobko, I., Eberle, R. B., Roy, M., and Horovitz, A. (2022) A diminished hydrophobic effect inside the GroEL/ES cavity contributes to protein substrate destabilization. *Proc National Acad Sci*. 119, e2213170119
18. Weissman, J. S., Rye, H. S., Fenton, W. A., Beechem, J. M., and Horwich, A. L. (1996) Characterization of the Active Intermediate of a GroEL–GroES-Mediated Protein Folding Reaction. *Cell*. 84, 481–490
19. Neidhardt, F. C., and VanBogelen, R. A. (1981) Positive regulatory gene for temperature-controlled proteins in Escherichia coli. *Biochem Bioph Res Co*. 100, 894–900

20. Cheng, M. Y., Hartl, F.-U., Martin, J., Pollock, R. A., Kalousek, F., Neuper, W., Hallberg, E. M., Hallberg, R. L., and Horwich, A. L. (1989) Mitochondrial heat-shock protein hsp60 is essential for assembly of proteins imported into yeast mitochondria. *Nature*. 337, 620–625
21. Manning-Krieg, U. C., Scherer, P. E., and Schatz, G. (1991) Sequential action of mitochondrial chaperones in protein import into the matrix. *Embo J*. 10, 3273–3280
22. Itoh, H., Kobayashi, R., Wakui, H., Komatsuda, A., Ohtani, H., Miura, A. B., Otaka, M., Masamune, O., Andoh, H., and Koyama, K. (1995) Mammalian 60-kDa stress protein (chaperonin homolog). Identification, biochemical properties, and localization. *J Biol Chem*. 270, 13429–13435
23. Beyene, D. A., Naab, T. J., Kanarek, N. F., Apprey, V., Esnakula, A., Khan, F. A., Blackman, M. R., Brown, C. A., and Hudson, T. S. (2018) Differential expression of Annexin 2, SPINK1, and Hsp60 predict progression of prostate cancer through bifurcated WHO Gleason score categories in African American men. *Prostate*. 78, 801–811
24. Castilla, C., Congregado, B., Conde, J. M., Medina, R., Torrubia, F. J., Japón, M. A., and Sáez, C. (2010) Immunohistochemical Expression of Hsp60 Correlates With Tumor Progression and Hormone Resistance in Prostate Cancer. *Urology*. 76, 1017.e1-1017.e6
25. Hansen, J., Svenstrup, K., Ang, D., Nielsen, M. N., Christensen, J. H., Gregersen, N., Nielsen, J. E., Georgopoulos, C., and Bross, P. (2007) A novel mutation in the HSPD1 gene in a patient with hereditary spastic paraplegia. *J Neurol*. 254, 897–900
26. Hansen, J. J., Dürr, A., Cournu-Rebeix, I., Georgopoulos, C., Ang, D., Nielsen, M. N., Davoine, C.-S., Brice, A., Fontaine, B., Gregersen, N., and Bross, P. (2002) Hereditary Spastic Paraplegia SPG13 Is Associated with a Mutation in the Gene Encoding the Mitochondrial Chaperonin Hsp60. *Am J Hum Genetics*. 70, 1328–1332
27. Magen, D., Georgopoulos, C., Bross, P., Ang, D., Segev, Y., Goldsher, D., Nemirovski, A., Shahar, E., Ravid, S., Luder, A., Heno, B., Gershoni-Baruch, R., Skorecki, K., and Mandel, H. (2008) Mitochondrial Hsp60 Chaperonopathy Causes an Autosomal-Recessive

Neurodegenerative Disorder Linked to Brain Hypomyelination and Leukodystrophy. *Am J Hum Genetics*. 83, 30–42

28. Bross, P., Naundrup, S., Hansen, J., Nielsen, M. N., Christensen, J. H., Kruhøffer, M., Palmfeldt, J., Corydon, T. J., Gregersen, N., Ang, D., Georgopoulos, C., and Nielsen, K. L. (2008) The Hsp60-(p.V98I) Mutation Associated with Hereditary Spastic Paraplegia SPG13 Compromises Chaperonin Function Both *in Vitro* and *in Vivo*. *J Biol Chem*. 283, 15694–15700
29. Fontaine, B., Davoine, C.-S., Dürr, A., Paternotte, C., Feki, I., Weissenbach, J., Hazan, J., and Brice, A. (2000) A New Locus for Autosomal Dominant Pure Spastic Paraplegia, on Chromosome 2q24-q34. *American Journal of Human Genetics*. 66, 702–707
30. Meng, Q., Li, B. X., and Xiao, X. (2018) Toward Developing Chemical Modulators of Hsp60 as Potential Therapeutics. *Frontiers Mol Biosci*. 10.3389/fmolb.2018.00035
31. Nakamura, H., and Minegishi, H. (2013) HSP60 as a Drug Target. *Current Pharmaceutical Design*. 19, 441–451
32. Polson, E. S., Kuchler, V. B., Abbosh, C., Ross, E. M., Mathew, R. K., Beard, H. A., Silva, B. da, Holding, A. N., Ballereau, S., Chuntharpursat-Bon, E., Williams, J., Griffiths, H. B. S., Shao, H., Patel, A., Davies, A. J., Droop, A., Chumas, P., Short, S. C., Lorger, M., Gestwicki, J. E., Roberts, L. D., Bon, R. S., Allison, S. J., Zhu, S., Markowetz, F., and Wurdak, H. (2018) KHS101 disrupts energy metabolism in human glioblastoma cells and reduces tumor growth in mice. *Sci Transl Med*. 10, eaar2718
33. Gestwicki, J. E., and Shao, H. (2019) Inhibitors and chemical probes for molecular chaperone networks. *J Biol Chem*. 294, 2151–2161
34. Brocchieri, L., and Karlin, S. (2008) Conservation among HSP60 sequences in relation to structure, function, and evolution. *Protein Sci*. 9, 476–486

35. Klebl, D. P., Feasey, M. C., Hesketh, E. L., Ranson, N. A., Wurdak, H., Sobott, F., Bon, R. S., and Muench, S. P. (2021) Cryo-EM structure of human mitochondrial HSPD1. *Iscience*. 24, 102022

36. Nisemblat, S., Yaniv, O., Parnas, A., Frolow, F., and Azem, A. (2015) Crystal structure of the human mitochondrial chaperonin symmetrical football complex. *Proc National Acad Sci*. 112, 6044–6049

37. Gomez-Llorente, Y., Jebara, F., Patra, M., Malik, R., Nisemblat, S., Chomsky-Hecht, O., Parnas, A., Azem, A., Hirsch, J. A., and Ubarretxena-Belandia, I. (2020) Structural basis for active single and double ring complexes in human mitochondrial Hsp60-Hsp10 chaperonin. *Nat Commun*. 11, 1916

38. Wang, J. C.-Y., and Chen, L. (2021) Structural basis for the structural dynamics of human mitochondrial chaperonin mHsp60. *Sci Rep-uk*. 11, 14809

39. Viitanen, P. V., Lorimer, G., Bergmeier, W., Weiss, C., Kessel, M., and Goloubinoff, P. (1998) [18] Purification of mammalian mitochondrial chaperonin 60 through in Vitro reconstitution of active oligomers, pp. 203–217, Methods in Enzymology, Elsevier, 290, 203–217

40. Miyazaki, T., Yoshimi, T., Furutsu, Y., Hongo, K., Mizobata, T., Kanemori, M., and Kawata, Y. (2002) GroEL-Substrate-GroES Ternary Complexes Are an Important Transient Intermediate of the Chaperonin Cycle*. *J Biol Chem*. 277, 50621–50628

41. Taniguchi, M., Yoshimi, T., Hongo, K., Mizobata, T., and Kawata, Y. (2004) Stopped-flow Fluorescence Analysis of the Conformational Changes in the GroEL Apical Domain RELATIONSHIPS BETWEEN MOVEMENTS IN THE APICAL DOMAIN AND THE QUATERNARY STRUCTURE OF GroEL*. *J Biol Chem*. 279, 16368–16376

42. Kawata, Y., Kawagoe, M., Hongo, K., Miyazaki, T., Higurashi, T., Mizobata, T., and Nagai, J. (1999) Functional Communications between the Apical and Equatorial Domains of GroEL through the Intermediate Domain †. *Biochemistry-us*. 38, 15731–15740

43. Chen, L., Syed, A., and Balaji, A. (2022) Hereditary spastic paraplegia SPG13 mutation increases structural stability and ATPase activity of human mitochondrial chaperonin. *Sci Rep-uk*. 12, 18321

44. Gray, T. E., and Fersht, A. R. (1991) Cooperativity in ATP hydrolysis by GroEL is increased by GroES. *Febs Lett*. 292, 254–258

45. Bochkareva, E. S., Lissin, N. M., Flynn, G. C., Rothman, J. E., and Girshovich, A. S. (1992) Positive cooperativity in the functioning of molecular chaperone GroEL. *J Biol Chem*. 267, 6796–6800

46. Shao, H., Oltion, K., Wu, T., and Gestwicki, J. E. (2020) Differential scanning fluorimetry (DSF) screen to identify inhibitors of Hsp60 protein–protein interactions. *Org Biomol Chem*. 18, 4157–4163

47. Cheng, M. Y., Hartl, F.-U., and Norwich, A. L. (1990) The mitochondrial chaperonin hsp60 is required for its own assembly. *Nature*. 348, 455–458

48. Zhou, M., Li, Y., Hu, Q., Bai, X., Huang, W., Yan, C., Scheres, S. H. W., and Shi, Y. (2015) Atomic structure of the apoptosome: mechanism of cytochrome c- and dATP-mediated activation of Apaf-1. *Gene Dev*. 29, 2349–2361

49. Chen, D.-H., Madan, D., Weaver, J., Lin, Z., Schröder, G. F., Chiu, W., and Rye, H. S. (2013) Visualizing GroEL/ES in the Act of Encapsulating a Folding Protein. *Cell*. 153, 1354–1365

50. Levy-Rimler, G., Viitanen, P., Weiss, C., Sharkia, R., Greenberg, A., Niv, A., Lustig, A., Delarea, Y., and Azem, A. (2001) The effect of nucleotides and mitochondrial chaperonin 10 on the structure and chaperone activity of mitochondrial chaperonin 60. *Eur J Biochem*. 268, 3465–3472

51. Ranson, N. A., Clare, D. K., Farr, G. W., Houldershaw, D., Horwich, A. L., and Saibil, H. R. (2006) Allosteric signaling of ATP hydrolysis in GroEL–GroES complexes. *Nat Struct Mol Biol*. 13, 147–152

52. Tang, Y.-C., Chang, H.-C., Roeben, A., Wischnewski, D., Wischnewski, N., Kerner, M. J., Hartl, F. U., and Hayer-Hartl, M. (2006) Structural Features of the GroEL-GroES Nano-Cage Required for Rapid Folding of Encapsulated Protein. *Cell*. 125, 903–914

53. Roh, S.-H., Hryc, C. F., Jeong, H.-H., Fei, X., Jakana, J., Lorimer, G. H., and Chiu, W. (2017) Subunit conformational variation within individual GroEL oligomers resolved by Cryo-EM. *Proc National Acad Sci*. 114, 8259–8264

54. Zhao, Y., Schmid, M. F., Frydman, J., and Chiu, W. (2021) CryoEM reveals the stochastic nature of individual ATP binding events in a group II chaperonin. *Nat Commun*. 12, 4754

55. Farr, G. W., Fenton, W. A., Chaudhuri, T. K., Clare, D. K., Saibil, H. R., and Horwich, A. L. (2003) Folding with and without encapsulation by cis- and trans-only GroEL–GroES complexes. *Embo J*. 22, 3220–3230

56. Chaudhuri, T. K., Farr, G. W., Fenton, W. A., Rospert, S., and Horwich, A. L. (2001) GroEL/GroES-Mediated Folding of a Protein Too Large to Be Encapsulated. *Cell*. 107, 235–246

57. Braig, K., Otwinowski, Z., Hegde, R., Boisvert, D. C., Joachimiak, A., Horwich, A. L., and Sigler, P. B. (1994) The crystal structure of the bacterial chaperonin GroEL at 2.8 Å. *Nature*. 371, 578–586

58. Parnas, A., Nadler, M., Nisemblat, S., Horovitz, A., Mandel, H., and Azem, A. (2009) The MitCHAP-60 Disease Is Due to Entropic Destabilization of the Human Mitochondrial Hsp60 Oligomer. *J Biol Chem*. 284, 28198–28203

59. Viitanen, P. V., Lorimer, G. H., Seetharam, R., Gupta, R. S., Oppenheim, J., Thomas, J. O., and Cowan, N. J. (1992) Mammalian Mitochondrial Chaperonin 60 Functions as a Single Toroidal Ring. *Journal of Biological Chemistry*. 267, 695–698

60. Yan, X., Shi, Q., Bracher, A., Miličić, G., Singh, A. K., Hartl, F. U., and Hayer-Hartl, M. (2018) GroEL Ring Separation and Exchange in the Chaperonin Reaction. *Cell*. 172, 605-617.e11

61. Nielsen, K. L., and Cowan, N. J. (1998) A Single Ring Is Sufficient for Productive Chaperonin-Mediated Folding In Vivo. *Mol Cell*. 2, 93–99

62. Dubaquié, Y., Looser, R., and Rospert, S. (1997) Significance of chaperonin 10-mediated inhibition of ATP hydrolysis by chaperonin 60. *Proc National Acad Sci*. 94, 9011–9016

63. Chang, L., Bertelsen, E. B., Wisén, S., Larsen, E. M., Zuiderweg, E. R. P., and Gestwicki, J. E. (2008) High-throughput screen for small molecules that modulate the ATPase activity of the molecular chaperone DnaK. *Anal Biochem*. 372, 167–176

64. Mastronarde, D. N. (2005) Automated electron microscope tomography using robust prediction of specimen movements. *J Struct Biol*. 152, 36–51

65. Zheng, S. Q., Palovcak, E., Armache, J.-P., Verba, K. A., Cheng, Y., and Agard, D. A. (2017) MotionCor2: anisotropic correction of beam-induced motion for improved cryo-electron microscopy. *Nat Methods*. 14, 331–332

66. Punjani, A., Rubinstein, J. L., Fleet, D. J., and Brubaker, M. A. (2017) cryoSPARC: algorithms for rapid unsupervised cryo-EM structure determination. *Nat Methods*. 14, 290–296

67. Scheres, S. H. W. (2012) RELION: Implementation of a Bayesian approach to cryo-EM structure determination. *J Struct Biol*. 180, 519–530

68. Emsley, P., Lohkamp, B., Scott, W. G., and Cowtan, K. (2010) Features and development of Coot. *Acta Crystallogr Sect D Biological Crystallogr*. 66, 486–501

69. Afonine, P. V., Poon, B. K., Read, R. J., Sobolev, O. V., Terwilliger, T. C., Urzhumtsev, A., and Adams, P. D. (2018) Real-space refinement in PHENIX for cryo-EM and crystallography. *Acta Crystallogr Sect D Struct Biology*. 74, 531–544

70. Croll, T. I. (2018) ISOLDE: a physically realistic environment for model building into low-resolution electron-density maps. *Acta Crystallogr Sect D Struct Biology*. 74, 519–530

71. Pettersen, E. F., Goddard, T. D., Huang, C. C., Meng, E. C., Couch, G. S., Croll, T. I., Morris, J. H., and Ferrin, T. E. (2021) UCSF ChimeraX: Structure visualization for researchers, educators, and developers. *Protein Sci*. 30, 70–82

72. Pettersen, E. F., Goddard, T. D., Huang, C. C., Couch, G. S., Greenblatt, D. M., Meng, E. C., and Ferrin, T. E. (2004) UCSF Chimera—A visualization system for exploratory research and analysis. *J Comput Chem*. 25, 1605–1612

Chapter 4

Structural basis for intermediate activation of the human 20S proteasome by a sub-optimal HbYX sequence

Contributing Authors:

Julian R. Braxton[1-4], Sarah K. Williams[2,3], Eric Tse[2,4], Daniel R. Southworth[2,4], and Jason E. Gestwicki[2,3]

[1]Graduate Program in Chemistry and Chemical Biology; University of California, San Francisco; San Francisco, CA 94158, USA

[2]Institute for Neurodegenerative Diseases; University of California, San Francisco; San Francisco, CA 94158, USA

[3]Department of Pharmaceutical Chemistry; University of California, San Francisco; San Francisco, CA 94158, USA

[4]Department of Biochemistry and Biophysics; University of California, San Francisco; San Francisco, CA 94158, USA

Abstract

The proteasome is responsible for the controlled degradation of nearly all cellular proteins. In higher organisms, activity of the 20S core particle is regulated by gating residues that occlude the entrance to the proteolytic active sites located in the 20S interior, preventing indiscriminate processing of substrates. Activation of the proteasome is enabled by proteasomal activator (PA) proteins that bind the apical face of the 20S particle using C-terminal peptides with canonical hydrophobic, Tyr, any amino acid (HbYX) motifs. These peptides open the 20S gate, allowing for substrates to passively diffuse or be actively threaded into the interior. Though the determinants of HbYX-mediated activation have been well established in the archaeal proteasome, less is understood about activation of the human 20S (h20S), in large part due to the evolution of paralogous subunits with distinct peptide binding pockets. Here, we attempt to improve understanding of h20S activation by determining a high-resolution cryo-EM structure of h20S bound to the sub-optimal sequence NLSFFT grafted onto the *Trypanosoma brucei* PA26 activator. This structure reveals distinct activator peptide conformations and an intermediate extent of gate opening that correlates well with *in vitro* proteolytic activity.

Introduction

The efficient degradation of proteins is a key component of cellular protein homeostasis (proteostasis) (1). The proteasome is an essential and highly conserved proteolytic machine that enables the degradation of most cellular proteins. Decline in proteasomal activity is observed in aging and neurodegenerative disease, underscoring the importance of this process in human health. Indeed, pharmacological activation of the proteasome is a potential therapeutic strategy to ameliorate cellular dysfunction associated with a reduced capacity to clear damaged or misfolded proteins (2). Conversely, the dependence of some cancers on proteasomal activity has led to the development of proteasome inhibitors as cancer therapeutics (3). These observations

suggest that modulating proteasomal activity has potential as a versatile therapeutic modality in numerous diseases.

The minimal unit of proteasomal activity is the cylindrical 20S core particle. The 20S is composed of four stacked heptamers composed of two subunit types, α and β, arranged in the pattern α-β-β-α (4). β subunits contain the proteolytic active sites while α subunits form a gate at the 20S periphery. In simple organisms like archaea, there is only one of each α and β subunit, whereas in eukaryotes there are seven paralogous α and β subunits each. These subunits are arranged in a conserved pattern and enable distinct proteolytic activities and more complex regulation of substrate degradation (5). Additionally, in eukaryotic proteasomes isolated 20S particles are largely inactive, due to N-terminal extensions of α subunits that form a closed gate that prevents access of large substrates to the interior. Thus, the 20S needs to be activated by accessory proteins in order to function. These proteasomal activators (PAs) can be divided into two main groups: those that enable the degradation of ubiquitylated (as in the ubiquitin-proteasome system, UPS) or non-ubiquitylated (the ubiquitin-independent-proteasome system, UIPS). PAs in both classes frequently have C-terminal sequences (canonical sequence hydrophobic, Tyr, any amino acid, HbYX) that bind to pockets formed at the intersubunit interfaces of the α ring. Binding of HbYX peptides induces a conformational rearrangement of the α gating residues, exposing a pore through which substrates can pass (6).

Though the HbYX model of proteasomal activation was developed using the archaeal proteasome (7), the activation mechanism of human 20S appears distinct, likely due to the unique pockets formed by α subunits. Indeed, the consensus sequence for h20S activation by HbYX-like peptides was recently revised to Tyr-Phe/Tyr (Φ) in the P3 and P2 positions (**Figure 4.1A**), reflecting different requirements for binding and activation (8). In that work, the optimal peptide for proteasomal activation was determined to be N-NLSYYT-C. Furthermore, a structure of h20S bound to a PA26 (UIPS activator) chimera with NLSYYT as its terminal residues revealed that the

YY motif forms a pi stack and hydrogen bonds to the N-terminal regions of the α subunits, resulting in gate opening. Though the experiments in the aforementioned study provide a strong mechanistic basis for h20S proteasome activation, structural understanding of gate opening was only obtained using the optimal NLSYYT sequence. Thus, correlating peptide-mediated proteasome activation *in vitro* with direct observation of structural remodeling is limited in this defined system.

In this work we sought to structurally characterize h20S bound to the sub-optimal PA26-peptide fusion NLSFFT in order to visualize intermediate states of activation. Intriguingly, the EC_{50} of h20S activation using this construct is similar to that with the optimal construct, but proteasome activity is only stimulated to ~50% using the fluorogenic substrate suc-LLVY-amc (**Figure 4.1B**) (8). High-resolution cryo-EM analysis of this complex reveals that in some pockets the FF dyad adopts the same conformation as in the NLSYYT structure, while in others a distinct conformation is observed. Strikingly, these interactions remodel the gates to a state between that of unliganded and NLSFFT-bound α rings, in which the pore is partially but not completely occluded. This extent of opening likely explains the incomplete activation observed biochemically. This work increases our understanding of the mechanism of h20S gate opening, and could inform the development of pharmacological h20S activators.

Results

Cryo-EM structure of h20S-PA26E102A-NLSFFT reveals liganding of α pockets and a partially-occluded gate

To determine how the Phe-Phe sequence remodels the h20S α gate, we substituted these residues for the Tyr-Tyr sequence in the previously used *Trypanosoma brucei* PA26 activator construct (8). As in the previous structure, this construct has the E102A mutation that ablates an alternative, non-HbYX-mediated activation mechanism present in this PA. Therefore, any observed remodeling can be solely attributed to HbYX-like activation. We incubated h20S with a

twofold molar excess of PA26 heptamer and prepared grids for cryo-EM analysis. Two-dimensional (2D) class averages of this sample reveal 20S particles with zero, one, or two PA26 molecules bound, indicating productive 20S-PA26 interactions (**Figure 4.S1A**). Next, three-dimensional (3D) classification reveals that ~43% of particles have at least some PA26 density, while the remainder resemble unliganded h20S (**Figure 4.S1B**). We therefore combined the PA26-containing particles and jointly refined them, which resulted in a 3.1 Å resolution structure with density for one PA26 heptamer bound to an α ring (**Figure 4.1C** and **Figure 4.S1B-D**). Density for the PA26 C-terminal tails is observed in six of seven α pockets, and the gating residues appear to mostly, though not completely, occlude the entrance to the proteasome interior (**Figure 4.1D**). The resolution of this map was sufficient to build an atomic model for both h20S and PA26, including the side chains of the PA26 tails (**Figure 4.S1E,F** and **Table 4.1**).

Distinct peptide conformations in FFT-bound h20S α pockets relative to YYT-bound pockets

We adopt the subunit numbering convention of the yeast 20S proteasome (5). Using this nomenclature, all α pockets except α7/1 have PA26 density, though the density in α6/7 is considerably weaker than the others (**Figure 4.2A**). Of note, reduced α6/7 occupancy (or resolution) was also observed in the NLSYYT structure, potentially indicating a weaker affinity for peptides in this pocket. The primary interactions made by resolved peptides include a salt bridge between the C-terminal carboxylate and positively charged ‘anchor’ residue at the base of the α pocket, and hydrophobic interactions with the N-terminal region of α subunits. The substitution of a canonical anchor residue in the α7/1 pocket for a His likely explains the lack of peptide density, and is consistent with the previous NLSYYT structure. C-terminal peptides can be classified as ‘anchored’ or ‘unanchored’ based on the proximity of the C-terminal carboxylate to the anchor residue (**Figure 4.2B**). As in the NLSYYT structure, peptides in α2/3, α3/4, α4/5, and α5/6 are anchored (heavy atom-heavy atom distances 2.6-4.5 Å), while in the α1/2 pocket the peptide is unanchored (distance 6.9 Å). Though the resolution of the peptide in α6/7 is insufficient to

confidently model interactions, we provisionally consider this peptide anchored based on its estimated position in the pocket.

Of the five pockets with side chain density for the FF dyad, two major conformations are observed (**Figure 4.2A,C**). In α1/2, α2/3, and α3/4, the rings of the Phe residues are parallel to each other and somewhat laterally displaced, and thus appear to be engaging in pi stacking interactions. This conformation closely mirrors that found in α1/2 in the NLSYYT structure. Furthermore, the increased anchor salt bridge distance in these pockets (NLSFFT-bound α1/2, α2/3, and α3/4 NLSYYT-bound α1/2) appears correlated with this conformation. In α4/5 and α5/6, the P3 Phe is rotated out of alignment with P2, such that pi stacking does not occur. Curiously, in these pockets the anchor salt bridge distances are dramatically shorter than those in the α1/2-like conformation (~2.7 vs 5 Å), indicating that this arrangement of side chains allows for better interaction with the anchor residue.

Notably, in no pockets are the FF dyads oriented towards the region immediately N-terminal to H0 of the α subunits; this region undergoes dramatic repositioning in YYT-bound pockets that leads to gate opening (8). The distinct orientations observed in the NLSFFT structure are likely due to the lack of tyrosine hydroxyls that mediate interaction with this region in the NLSYYT structure (**Figure 4.S2**). The absence of these interactions likely explains the modest change in positions of these N-terminal regions relative to those of unliganded h20S (**Figure 4.2A**).

Intermediate gate opening in the NLSFFT structure

Occupancy of α pockets opens the 20S gate by repositioning the region N-terminal to H0 away from the center of the complex (**Figure 4.3A**). A conserved network of residues including a proline and a tyrosine on H0 of the adjacent α subunit stabilizes this conformation (7). To determine the extent of gate opening induced by the NLSFFT sequence, we aligned unliganded, NLSFFT-bound, and NLSYYT-bound structures using the cis-β rings (chosen because they are

conformationally invariant) and inspected the positions of the conserved proline residue in each α subunit (**Figure 4.3B**). This analysis revealed that these prolines are appreciably repositioned relative to the unliganded structure in a subset of α subunits, namely α4, α5, and α6. In these subunits the FFT-bound prolines are located between those of the unliganded and YYT-bound residues, indicating that partial gate opening occurs in these subunits. Intriguingly, the pockets of α4 and α5 feature the shortest anchor salt bridge distances, suggesting that this interaction is required for full gate opening. In the other pockets the prolines are in the same position as in the unliganded structure, indicating that activation does not occur despite peptide occupancy.

Though the N-terminal regions of some α pockets are somewhat radially displaced in the NLSFFT-bound structure, this is apparently insufficient to fully open the 20S gate, as the network of N-termini over the pore is mostly intact (**Figure 4.1D**). However, comparison of the cis and trans gates in this structure reveals that the density for some cis gate residues is slightly worse, indicating partial disordering and exposing a small gap in the otherwise sealed gate (**Figure 4.4**). This likely explains the incomplete stimulation of proteolytic activity observed biochemically (**Figure 4.1B**).

Discussion

Proteasomal gate opening is necessary to allow substrates to enter the 20S interior for degradation. Though initial structure-activity relationships for HbYX-mediated gate opening were developed using homo-oligomeric α rings of archaeal proteasomes, the relative complexity of the human 20S raises additional questions about its activation mechanism. In this work we sought to determine the structural basis for h20S remodeling by a HbYX-like peptide (FFT) presented on the multivalent PA26 activator. This construct binds the h20S but only partially stimulates proteolysis of a model substrate, suc-LLVY-amc. Using high-resolution cryo-EM, we determined that FFT peptides bind in conserved and distinct arrangements in α subunits that partially open the 20S gate. Notably, the pattern of α subunit occupancy for this construct is identical to that

using the ideal YYT sequence, with absent or weak density in α7/1 and α6/7 and strong density in the others. This conservation indicates that some h20S α pockets are more amenable to liganding than others, regardless of sequence.

Curiously, despite appreciable repositioning of α subunit N-terminal regions that indicates a degree of activation (**Figure 4.3B**), the h20S gating residues largely resemble those in unliganded α rings. Though disordering of some regions of the gate is observed (**Figure 4.4**), it appears that full gate opening requires movement of the conserved prolines to their position in the YYT-bound structure; this suggests a step-like mechanism of gate opening rather than a graded structural rearrangement more correlated with the position of gating cluster residues including the conserved proline (**Figure 4.3B**) (7). Of note, it would be interesting to determine the extent of NLSFFT-mediated activation using other proteasome substrates. For example, though the YYT sequence is able to robustly stimulate the degradation of the larger substrate FAM-LFP (8), we speculate that degradation by the FFT variant would be sharply decreased, as the gate opening observed with this sequence is likely too small to accommodate substrates significantly larger than the LLVY peptide tested.

The work presented here has the potential to inform future development of pharmacological h20S activators. An increase in unliganded (and therefore inactive) h20S particles is associated with aging and age-related disorders, and stimulating 20S activity therefore represent a promising therapeutic approach in these conditions (2). The homo-oligomeric PA26 platform used here and in previous studies (8) allows for the assessment of peptide activator sequence on rearrangement of the seven distinct α subunits in the human proteasome. Coupled with the observations from the previous YYT-bound structure, it appears that α4, α5, and α6 are the most amenable for liganding and activation, even using the sub-optimal FFT sequence, and structure-guided efforts to develop might therefore be targeted to these subunits. Future studies to further improve understanding of h20S activation will undoubtedly aid in this effort.

Figures

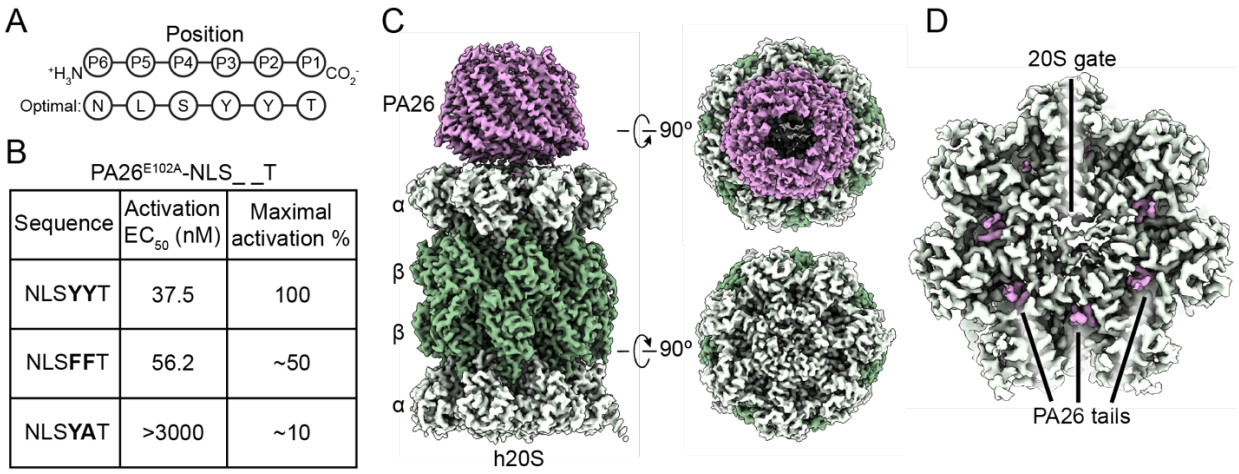

Sequence	Activation EC_{50} (nM)	Maximal activation %
NLS**YY**T	37.5	100
NLS**FF**T	56.2	~50
NLS**YA**T	>3000	~10

Figure 4.1 Cryo-EM structure of h20S-PA26-NLSFFT
(**A**) Nomenclature of HbYX-like peptides, using optimal sequence from (8) as an example. (**B**) Activation parameters of $PA26^{E102A}$ chimeras on human 20S proteasome activity, adapted from (8). (**C**) Sharpened map of h20S-$PA26^{E102A}$-NLSFFT. α and β rings of the 20S proteasome are colored in light and dark green, respectively. PA26 is colored in purple. (**D**) View of PA26-bound α ring, showing density for PA26 C-terminal tails and a partially occluded gate.

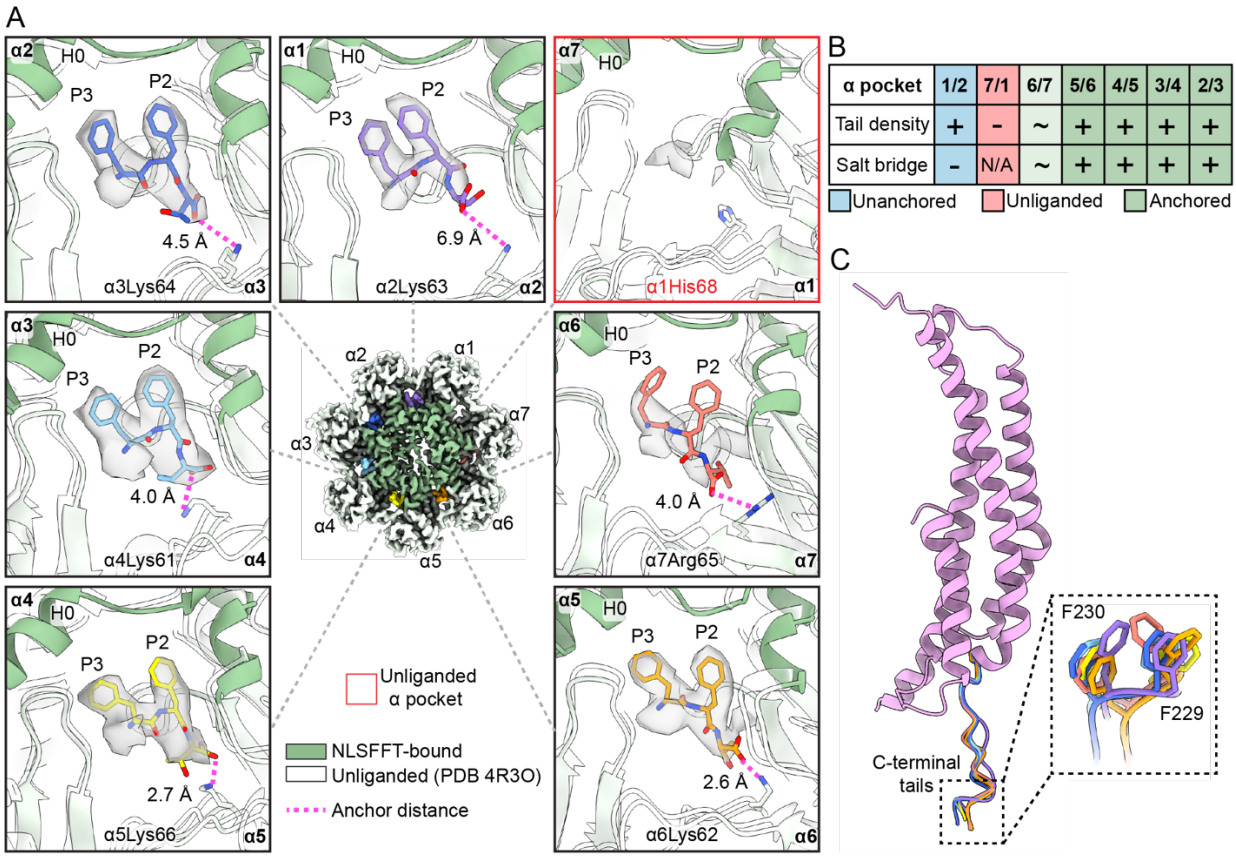

Figure 4.2 h20S alpha pockets and C-terminal peptide conformation

(**A**) Enlarged views of PA26-bound α ring pockets. The three terminal residues of the PA26 tails are shown (FFT), overlaid with the corresponding density from the sharpened map (transparent gray). PA26-bound h20S is shown in green, and is overlaid with an unbound structure (PDB 4R3O), aligned by the cis-β ring. Anchor residues are shown in each pocket, as well as the distance to the C-terminal carboxylate, where applicable. (**B**) Table summarizing peptide interactions with the proteasome. The lighter green used to color pocket 6/7 indicates partial occupancy. (**C**) Overlay of all PA26 C-terminal tails, showing distinct binding conformations.

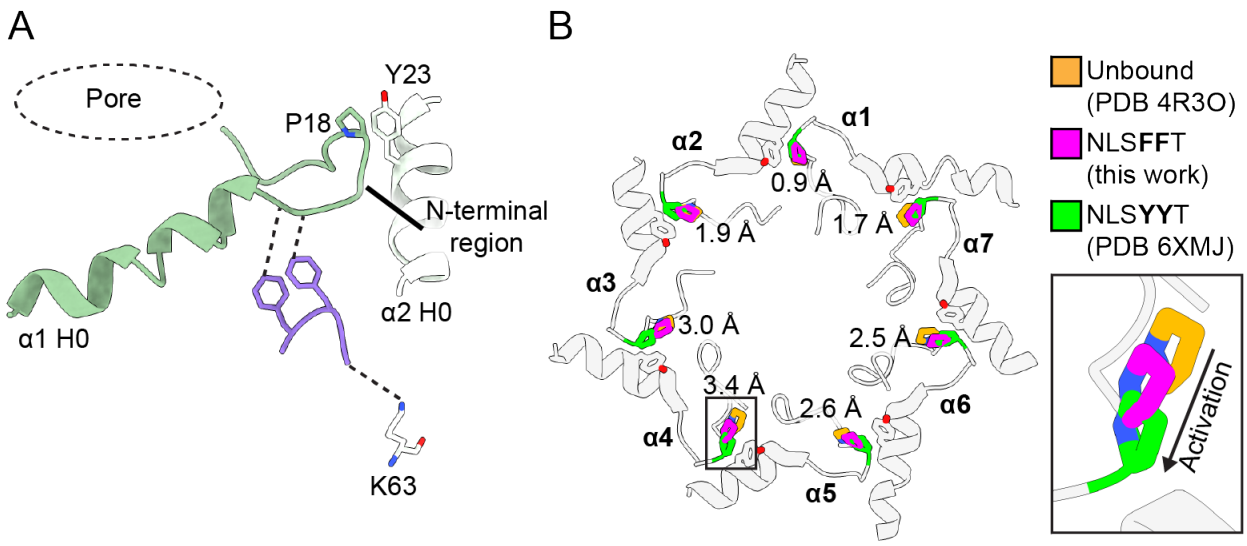

Figure 4.3 Intermediate N-terminal repositioning in the NLSFFT-bound α ring
(**A**) Schematic of HbYX-mediated proteasomal activation, using the α1/2 pocket of the NLSFFT-bound structure as an example. (**B**) View of α-subunit N-terminal proline residues in unbound (orange, PDB 4R3O), PA26-NLSFFT (magenta), and NLSYYT (green, PDB 6XMJ) h20S α rings. Displayed distances are between proline alpha carbons of unbound and NLSYYT-bound structures (models were aligned by the cis-β ring). The remainder of the N-terminal region and H0 from PDB 6XMJ are shown for reference (gray). A magnified view of proline 12 of α4 is shown at right.

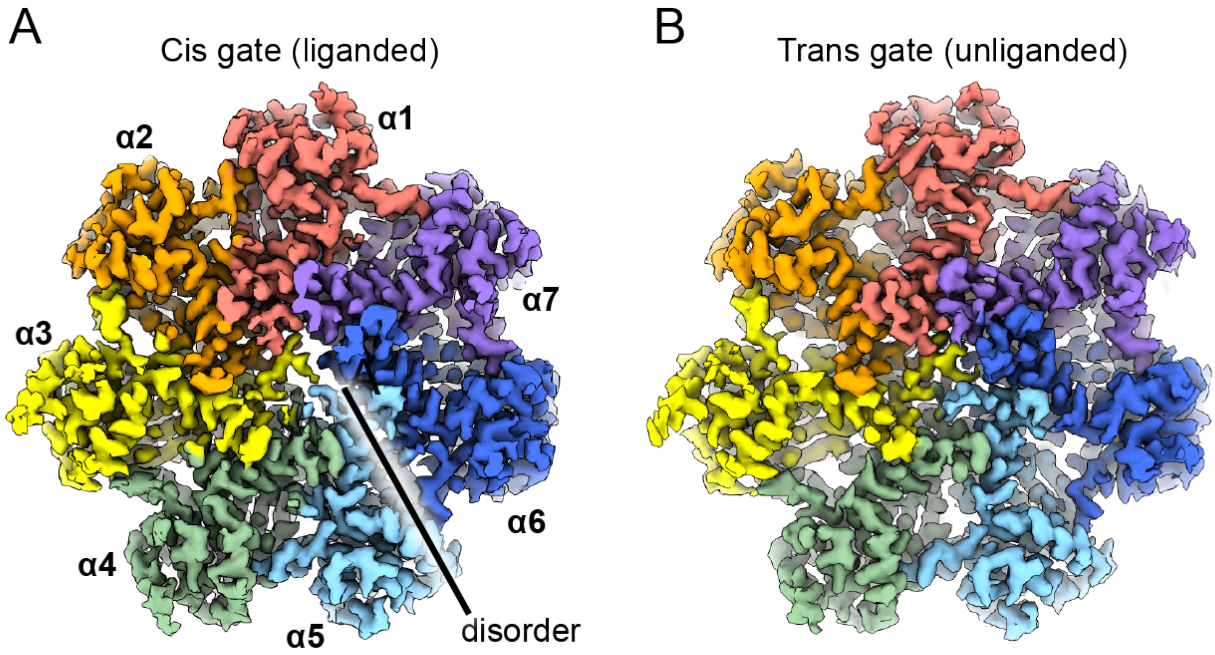

Figure 4.4 Disorder in pore loop gating residues
Sharpened maps of cis (**A**) and (**B**) trans h20S-PA26-NLSFFT-bound α rings. α subunits 1-7 are colored from red to purple. Note gaps in cis ring gate relative to trans ring.

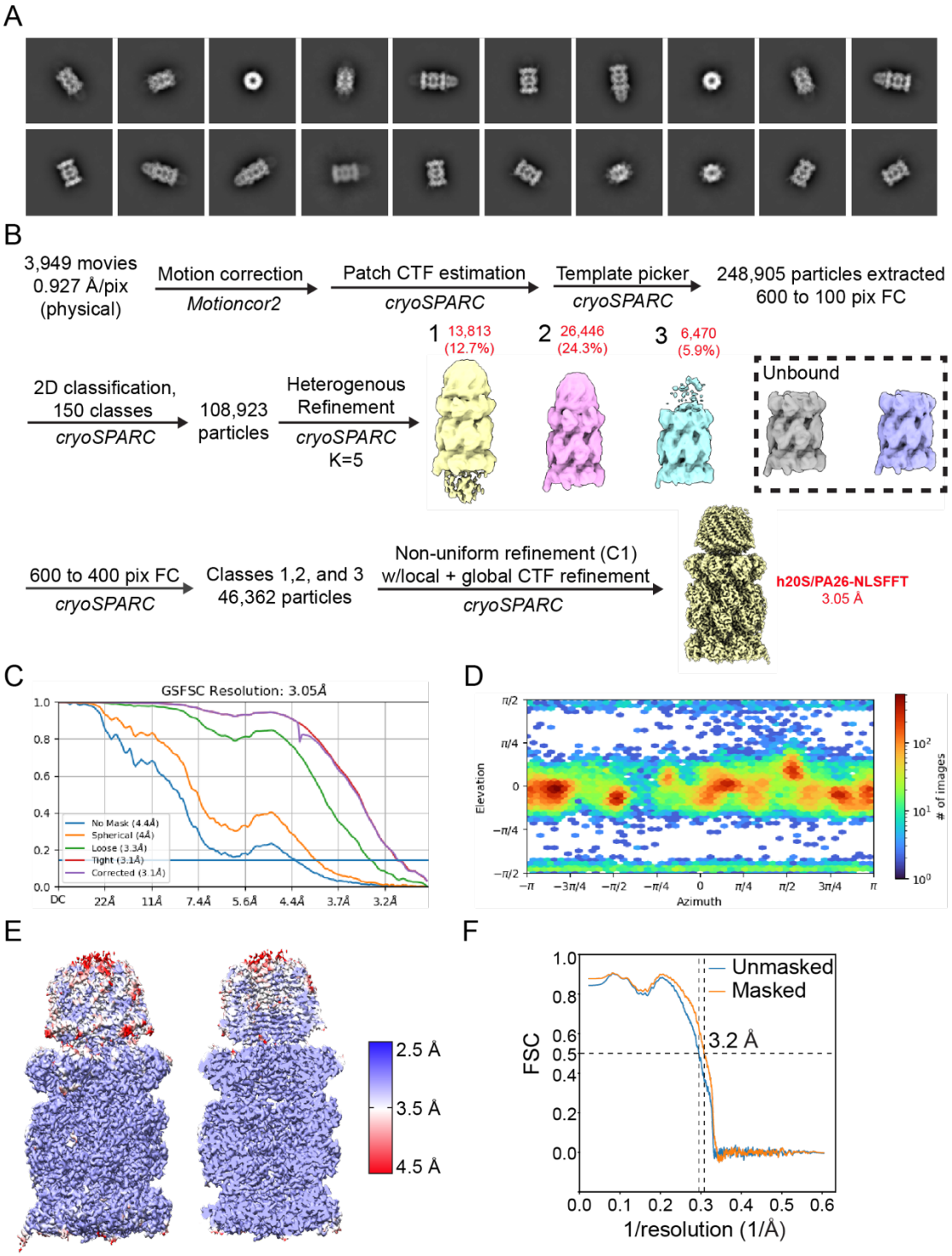

Figure 4.S1 Cryo-EM analysis of h20S-PA26-NLSFFT
(**A**) 2D class averages from the h20S-PA26-NLSFFT dataset. (**B**) Cryo-EM processing workflow for h20S-PA26-NLSFFT structure determination. (**C**) Fourier shell correlation (FSC) curves for h20S-PA26-NLSFFT. (**D**) Orientation distribution plot for h20S-PA26-NLSFFT. (**E**) Local resolution of h20S-PA26-NLSFFT, displayed on the sharpened map. A cut-through of the map is shown at right. (**F**) Map-model FSC curve for h20S-PA26-NLSFFT. Displayed model resolution was determined using the masked map.

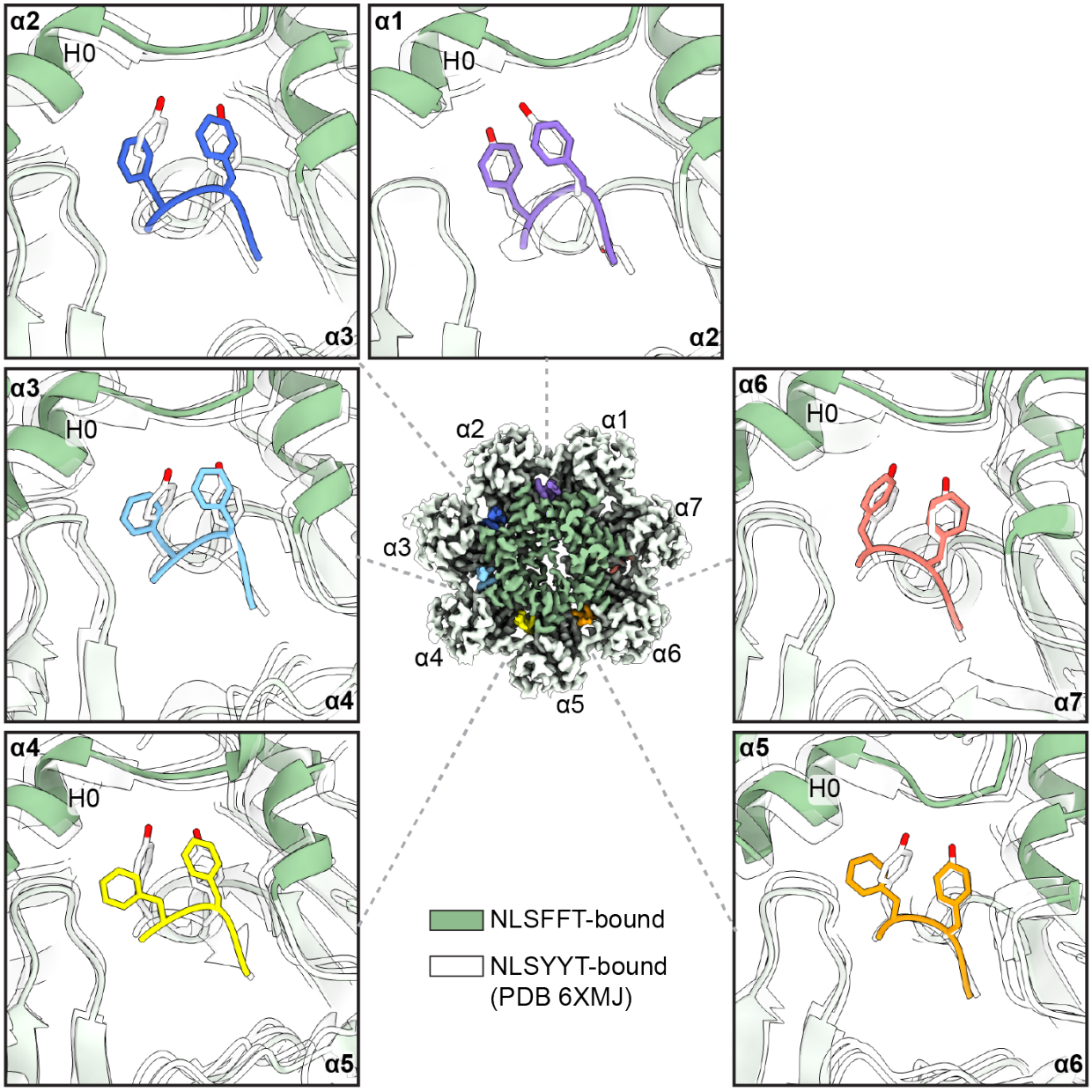

Figure 4.S2 Comparison of NLSFFT and NLSYYT peptide poses in PA26-bound h20S proteasomes

Enlarged views of PA26-bound α ring pockets for NLSFFT (green) and NLSYYT (PDB 6XMJ, transparent white) sequences. Structures were aligned by the cis-β ring.

Tables

Table 4.1 Cryo-EM data collection, refinement, and validation statistics of h20S-PA26-NLSFFT

	h20S-PA26-NLSFFT
Data collection and processing	
Microscope and camera	Glacios, K2
Magnification	53,937
Voltage (kV)	200
Data acquisition software	SerialEM
Exposure navigation	Image shift
Electron exposure ($e^-/Å^2$)	66
Defocus range (μm)	-0.5 to -2.5
Pixel size (Å)	0.927
Symmetry imposed	C1
Initial particle images (no.)	248,905
Final particle images (no.)	46,362
Map resolution (Å)	3.1
FSC threshold	0.143
Map resolution range (Å)	2.5-10
Refinement	
Model resolution (Å)	3.2
FSC threshold	0.5
Map sharpening *B* factor ($Å^2$)	-79.8
Model composition	
Nonhydrogen atoms	59,440
Protein residues	7,639
Ligands	N/A
B factors ($Å^2$)	
Protein	55.63
Ligand	N/A
R. m. s. deviations	
Bond lengths (Å)	0.024
Bond angles (°)	1.691
Validation	
MolProbity score	0.80
Clashscore	1.00
Poor rotamers (%)	0.11
Ramachandran plot	
Favored (%)	98.08
Allowed (%)	1.80
Disallowed (%)	0.12

Methods

Molecular cloning

The Q5 Site-Directed Mutagenesis kit (New England Biolabs) was used to introduce mutations into the *Trypanosoma brucei* PA26 expression construct. The final construct contains the E102A mutation and the sequence NLSFFT in place of the last six residues in the native protein.

Protein expression and purification

PA26^{E102A}-NLSFFT was expressed and purified as previously described (8). In brief, bacterial cell lysate was incubated with HisPur Ni-NTA resin (Thermo Scientific) pre-equilibrated in purification buffer (20 mM Tris pH 7.9, 20 mM NaCl), and eluted with elution buffer (purification buffer with 200 mM imidazole). Protein was then reduced with 1 mM DTT for 2 hours at 4 °C, and then buffer exchanged into purification buffer. Protein concentration was determined using the Pierce BCA Protein Assay Kit (Thermo Scientific).

Cryo-EM sample preparation, data collection, and image processing

2 μM human 20S proteasome (R&D Systems) was incubated with 4 μM PA26^{E102A}-NLSFFT heptamer in vitrification buffer (50 mM Tris pH 7.5, 10 mM $MgCl_2$, 1 mM DTT). 3 μL of sample was applied to a glow discharged (PELCO easiGlow, 15 mA, 2 min) holey carbon grid (Quantifoil R1.2/1.3 on a gold 300 mesh support), plunge frozen into liquid ethane cooled by liquid nitrogen using a Vitrobot (Thermo Fisher Scientific) operated at 4 °C and 100% humidity. The grid was imaged on a Glacios TEM (Thermo Fisher Scientific) operated at 200 kV and equipped with a K2 Summit direct electron detector (Gatan). Movies were acquired with SerialEM (9) in super-resolution mode at a calibrated magnification of 53,937, corresponding to a physical pixel size of 0.927 Å. A nominal defocus range of -1.0 to -2.0 μm was used with a total exposure time of 10 sec fractionated into 0.1 sec frames for a total dose of 66 $e^-/Å^2$ at a dose rate of 6 e^-/pix/s. Movies

were subsequently corrected for drift, dose-weighted, and Fourier-cropped by a factor of 2 using MotionCor2 (10).

A total of 3,949 motion-corrected micrographs were processed using cryoSPARC (11). After Patch CTF estimation, particles were picked using Template Picker and extracted with a box of 600 pixels Fourier cropped to 100 pixels. 2D classification, *ab initio* modeling, and 3D classification were performed, which resulted in three classes with density attributable to PA26 in addition to the 20S core particle, while two classes only had 20S density. Particles from the three PA26-bound classes were re-extracted with a box size of 600 pixels Fourier cropped to 400 pix, and jointly refined using Non-Uniform Refinement, with local and global CTF refinement enabled. This resulted in the h20S-PA26-NLSFFT map, with an estimated global resolution of 3.05 Å.

Molecular modeling

The h20S proteasome from PDB 6RGQ and PA26^{E102A} heptamer from PDB 6XMJ (h20S-PA26-NLSYAT) were docked into the h20S-PA26-NLSFFT map and used as a starting model. Residues in the PA26 C-terminal tails were mutated using Coot (12), and the model was refined using Phenix Real Space Refine (13). Coot, Isolde (14), Rosetta, and Phenix were used to finalize the model.

Figure preparation

Figures were prepared using Adobe Illustrator, UCSF Chimera, and UCSF ChimeraX (15, 16).

Resource Availability

Requests for resources and reagents should be directed to Jason E. Gestwicki or Daniel R. Southworth.

Acknowledgments

This work was supported by NIH grant F31GM142279 (to J.R.B.).

Author Contributions

J.R.B. performed cryo-EM experiments and modeling, and wrote and edited the manuscript. S.K.W. cloned, expressed, and purified the PA26^{E102A}-NLSFFT chimera. E.T. operated electron microscopes and assisted with data collection. J.E.G. and D.R.S. designed and supervised the project and edited the manuscript.

References

1. Balchin, D., Hayer-Hartl, M., and Hartl, F. U. (2016) In vivo aspects of protein folding and quality control. *Science*. 353, aac4354
2. Opoku-Nsiah, K. A., and Gestwicki, J. E. (2018) Aim for the core: suitability of the ubiquitin-independent 20S proteasome as a drug target in neurodegeneration. *Transl Res*. 198, 48–57
3. Thibaudeau, T. A., and Smith, D. M. (2019) A Practical Review of Proteasome Pharmacology. *Pharmacol Rev*. 71, 170–197
4. Löwe, J., Stock, D., Jap, B., Zwickl, P., Baumeister, W., and Huber, R. (1995) Crystal Structure of the 20S Proteasome from the Archaeon T. acidophilum at 3.4 Å Resolution. *Science*. 268, 533–539
5. Groll, M., Ditzel, L., Löwe, J., Stock, D., Bochtler, M., Bartunik, H. D., and Huber, R. (1997) Structure of 20S proteasome from yeast at 2.4Å resolution. *Nature*. 386, 463–471
6. Förster, A., Masters, E. I., Whitby, F. G., Robinson, H., and Hill, C. P. (2005) The 1.9 Å Structure of a Proteasome-11S Activator Complex and Implications for Proteasome-PAN/PA700 Interactions. *Mol Cell*. 18, 589–599
7. Smith, D. M., Chang, S.-C., Park, S., Finley, D., Cheng, Y., and Goldberg, A. L. (2007) Docking of the Proteasomal ATPases' Carboxyl Termini in the 20S Proteasome's α Ring Opens the Gate for Substrate Entry. *Mol Cell*. 27, 731–744
8. Opoku-Nsiah, K. A., Pena, A. H. de la, Williams, S. K., Chopra, N., Sali, A., Lander, G. C., and Gestwicki, J. E. (2022) The YΦ motif defines the structure-activity relationships of human 20S proteasome activators. *Nat Commun*. 13, 1226
9. Mastronarde, D. N. (2005) Automated electron microscope tomography using robust prediction of specimen movements. *J Struct Biol*. 152, 36–51

10. Zheng, S. Q., Palovcak, E., Armache, J.-P., Verba, K. A., Cheng, Y., and Agard, D. A. (2017) MotionCor2: anisotropic correction of beam-induced motion for improved cryo-electron microscopy. *Nat Methods*. 14, 331–332
11. Punjani, A., Rubinstein, J. L., Fleet, D. J., and Brubaker, M. A. (2017) cryoSPARC: algorithms for rapid unsupervised cryo-EM structure determination. *Nat Methods*. 14, 290–296
12. Emsley, P., Lohkamp, B., Scott, W. G., and Cowtan, K. (2010) Features and development of Coot. *Acta Crystallogr Sect D Biological Crystallogr*. 66, 486–501
13. Afonine, P. V., Poon, B. K., Read, R. J., Sobolev, O. V., Terwilliger, T. C., Urzhumtsev, A., and Adams, P. D. (2018) Real-space refinement in PHENIX for cryo-EM and crystallography. *Acta Crystallogr Sect D Struct Biology*. 74, 531–544
14. Croll, T. I. (2018) ISOLDE: a physically realistic environment for model building into low-resolution electron-density maps. *Acta Crystallogr Sect D Struct Biology*. 74, 519–530
15. Pettersen, E. F., Goddard, T. D., Huang, C. C., Meng, E. C., Couch, G. S., Croll, T. I., Morris, J. H., and Ferrin, T. E. (2021) UCSF ChimeraX: Structure visualization for researchers, educators, and developers. *Protein Sci*. 30, 70–82
16. Pettersen, E. F., Goddard, T. D., Huang, C. C., Couch, G. S., Greenblatt, D. M., Meng, E. C., and Ferrin, T. E. (2004) UCSF Chimera—A visualization system for exploratory research and analysis. *J Comput Chem*. 25, 1605–1612

Publishing Agreement

It is the policy of the University to encourage open access and broad distribution of all theses, dissertations, and manuscripts. The Graduate Division will facilitate the distribution of UCSF theses, dissertations, and manuscripts to the UCSF Library for open access and distribution. UCSF will make such theses, dissertations, and manuscripts accessible to the public and will take reasonable steps to preserve these works in perpetuity.

I hereby grant the non-exclusive, perpetual right to The Regents of the University of California to reproduce, publicly display, distribute, preserve, and publish copies of my thesis, dissertation, or manuscript in any form or media, now existing or later derived, including access online for teaching, research, and public service purposes.

DocuSigned by:
Julian Braxton
258DDE1C0797487...
Author Signature

4/29/2023
Date